

AMRL-TR-76-10



ADA 025911

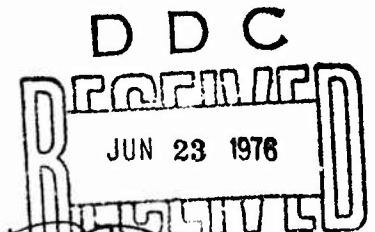
**A MODEL FOR
ANALYTIC INVESTIGATION OF
THREE DIMENSIONAL ~~XXXXXXXXXX~~ DYNAMICS
HEAD-SPINE**

*DEPARTMENT OF MATERIALS ENGINEERING
UNIVERSITY OF ILLINOIS AT CHICAGO CIRCLE
CHICAGO, ILLINOIS*

APRIL 1976

Approved for public release; distribution unlimited

AEROSPACE MEDICAL RESEARCH LABORATORY
AEROSPACE MEDICAL DIVISION
Air Force Systems Command
Wright-Patterson Air Force Base, Ohio 45433



NOTICES

When US Government drawings, specifications, or other data are used for any purpose other than a definitely related Government procurement operation, the Government thereby incurs no responsibility nor any obligation whatsoever, and the fact that the Government may have formulated, furnished, or in any way supplied the said drawings, specifications, or other data, is not to be regarded by implication or otherwise, as in any manner licensing the holder or any other person or corporation, or conveying any rights or permission to manufacture, use, or sell any patented invention that may in any way be related thereto.

Please do not request copies of this report from Aerospace Medical Research Laboratory. Additional copies may be purchased from:

National Technical Information Service
5285 Port Royal Road
Springfield, Virginia 22161

Federal Government agencies and their contractors registered with Defense Documentation Center should direct requests for copies of this report to:

Defense Documentation Center
Cameron Station
Alexandria, Virginia 22314

TECHNICAL REVIEW AND APPROVAL

This report has been reviewed by the Information Office (OI) and is releasable to the National Technical Information Service (NTIS). At NTIS, it will be available to the general public, including foreign nations.

This technical report has been reviewed and is approved for publication.

FOR THE COMMANDER



HENNING E. VON GIERKE
Director
Biodynamics and Bionics Division
Aerospace Medical Research Laboratory

SECURITY CLASSIFICATION OF THIS PAGE (When Data Entered)

29 REPORT DOCUMENTATION PAGE		READ INSTRUCTIONS BEFORE COMPLETING FORM
1. REPORT NUMBER AMRL TR-76-10	2. GOVT ACCESSION NO.	3. RECIPIENT'S CATALOG NUMBER
4. TITLE (and Subtitle) A MODEL FOR ANALYTIC INVESTIGATION OF THREE-DIMENSIONAL HEAD-SPINE DYNAMICS.	5. TYPE OF REPORT & PERIOD COVERED Final report 12-1-73 to 11-30-75	
6. AUTHOR(s) T. Belytschko, L. Schwer A. Schultz	8. CONTRACT OR GRANT NUMBER(s) F33615-74-C-4014 NEW	
9. PERFORMING ORGANIZATION NAME AND ADDRESS Department of Materials Engineering, University of Illinois at Chicago Circle Chicago, Illinois 60680	10. PROGRAM ELEMENT, PROJECT, TASK AREA & WORK UNIT NUMBERS PROGRAM ELEMENT: 62202F PROJECT: 7231; TASK: 7231-05; WORK UNIT: 7231-05-17	
11. CONTROLLING OFFICE NAME AND ADDRESS Aerospace Medical Research Laboratory, Aerospace Medical Division (AFSC) Wright-Patterson Air Force Base, Ohio 45433	12. REPORT DATE Apr 76	13. NUMBER OF PAGES 211
14. MONITORING AGENCY NAME & ADDRESS (if different from Controlling Office) AF-7231 723105	15. SECURITY CLASS. (of this report) Unclassified	
16. DISTRIBUTION STATEMENT (of this Report) Approved for public release; distribution unlimited		
17. DISTRIBUTION STATEMENT (of the abstract entered in Block 20, if different from Report) Final rept. 1 Dec 73 - 3p Nov 75		
18. SUPPLEMENTARY NOTES		
19. KEY WORDS (Continue on reverse side if necessary and identify by block number) Biomechanics, Spine, Head, Impact, Pilot Ejection		
20. ABSTRACT (Continue on reverse side if necessary and identify by block number) A three dimensional, discrete model of the human spine, torso and head was developed for the purpose of evaluating mechanical response in pilot ejection and it was developed in sufficient generality to be applicable to other body response problems, such as occupant response in aircraft crash and arbitrary loads on the head-spine system. There are no restrictions on the distribution or direction of applied loads, so a wide variety of situations can		

1402 171

be treated.

The anatomy is modelled by a collection of rigid bodies, which represent skeletal segments such as the vertebrae, pelvis, head, and ribs, interconnected by deformable elements, which represent ligaments, cartilageneous joints, viscera, and connective tissues.

Techniques for representing other aspects of the ejection environment, such as harnesses and the seat geometry, are also included. The model is valid for large displacements of the spine and treats material nonlinearities.

The basic model is modular in format, so that various components may be omitted or replaced by simplified representations. Thus, while the complete model is rather complex and involves substantial computational effort, various simplified models are available that are quite effective in duplicating the response of the complete model within a range of conditions. Three methods of solution are available for the analysis: direct integration in time by either an explicit, central difference method or by an implicit, trapezoidal method, and a frequency analysis method.

Results are presented for a variety of conditions, such as different rates of onset, ejection at angles, effects of lumbar curvature, and eccentric head loadings. It is shown that large initial curvatures and perfectly vertical acceleration loadings result in substantial flexural response of the spine, which cause large bending moments. It is further shown that the combination of the spine's low flexural stiffness, initial curvature, and mass eccentricity are such that stability cannot be maintained in a 10 g ejection without restraints or spine-torso-musculature interaction.

The complete models were used mainly to study the effects of the rib cage and viscera on spinal response. The flexural stiffness of the torso is increased substantially by a visceral model, even though it has no inherent flexural stiffness. In addition, the viscera provide significant reductions in the axial loads.

Modal analyses were performed on several of the models under various conditions. Numerous flexural natural frequencies under 10 cps were found, but the lowest axial frequency is of the order of 20 cps. We hypothesized that the peaks in the 5-7 Hz range in driving point impedances observed experimentally in axial shaker table measurements result from parametric excitation of the flexural modes.

PREFACE

The research presented in this final report was performed under Air Force Contract F33615-74-C-4014 awarded to the University of Illinois at Chicago Circle for the period December 1, 1973 to November 31, 1975. The Air Force program monitor was Mr. Ints Kaleps of the Mathematics and Analysis Branch, Biodynamics and Bionics Division of the Aerospace Medical Research Laboratory, Aerospace Medical Division of the Air Force Systems Command at Wright-Patterson Air Force Base, Ohio.

ACCESSION for		
NTIS	White Section	<input checked="" type="checkbox"/>
DDC	Buff Section	<input type="checkbox"/>
SEARCHED		<input type="checkbox"/>
JUSTIFICATION.....		
.....		
RT.....		
IDENTIFICATION/AVAILABILITY CODES		
.....		
AVAIL. and/or SPECIAL		
A		

DDC
RECEIVED
JUN 23 1976
D

TABLE OF CONTENTS

	Page
CHAPTER I INTRODUCTION	
1. Objectives	7
2. Literature Review	9
3. General Description of Model.	12
4. Mathematical Model.	13
5. General Description of Models	25
CHAPTER II MATHEMATICAL FORMULATION OF MODEL	
1. Nomenclature and Coordinate Transformations	36
2. Derivations of Equations of Motion.	40
3. Deformable Elements	46
CHAPTER III MATHEMATICAL ASPECTS OF SOLUTION PROCEDURES	
1. Explicit Time Integration	63
2. Implicit Time Integration	69
3. Modal Analysis.	78
CHAPTER IV MATERIAL PROPERTIES AND GEOMETRY	
1. Thoracolumbar and Cervical Spine.	81
2. Rib Cage.	96
3. Viscera and Abdominal Cavity.	98
4. Head.	102
5. Pelvis.	103
6. Preliminary Evaluation of Injury Potential.	103
7. Inertial Properties	111
8. Summary of Models	113
CHAPTER V STUDIES OF SPINAL RESPONSE	
1. Isolated Ligamentous Spine Model.	117
2. Complete Spine Model.	141
3. Modal Analysis.	149
4. Cervical Spine Model.	151
References	164
APPENDIX I COMPUTER PROGRAM DESCRIPTION.	168
APPENDIX II ELEMENT STIFFNESS MATRICES.	203

LIST OF FIGURES

<u>Figure</u>		<u>Page</u>
1	Rigid body representation and coordinate systems: global coordinates (x, y, z) ; body coordinates $(\bar{x}, \bar{y}, \bar{z})$ and element coordinates $(\hat{x}, \hat{y}, \hat{z})$.	16
2	Spring element	17
3	Beam element	19
4	Hydrodynamic element	22
5	Seat model representation	24
6	Back view of isolated ligamentous spine model	26
7	Side view of isolated ligamentous spine model	27
8	Back view of spine-torso model with rib cage	31
9	Side view of spine-torso model with rib cage	32
10	Viscera as modelled by hydrodynamic elements	34
11	Beam element nomenclature	50
12	Response of L3 to axial load	89
13	Response to T1 to axial load	91
14	Cervical spine geometry	97
15	Head-helmet representation	105
16	Idealization of vertebral body for preliminary evaluation of injury criteria	107
17	Side view of Model I	114
18	Side view of Model II	115
19	Side view of Model III	116
20	Response of unrestrained spine at 40 msec	118
21	Response of unrestrained spine at 60 msec	119
22	Response of unrestrained spine at 80 msec	120

		<u>Page</u>
23	Seated configuration with large lumbar curvature	123
24	Erect seated configuration	124
25	Straight spine configuration	126
26	Comparison of maximum axial forces in spines with and without sagittal plane curvature	127
27	Comparison of maximum bending moments in spines with and without sagittal plane curvature	128
28	Injury potentials for large lumbar curvature spine	129
29	Injury potentials for erect spine	130
30	Comparison of head acceleration for fast and slow rate of onset	133
31	Comparison of axial force in L4/L3 for fast and slow rate of onset	134
32	Comparison of facet force in L3/L2 for fast and slow rate of onset	135
33	Comparison of moment in T4/T3 for fast and slow rate of onset	136
34	Response of spine to eccentric mass distribution of head	139
35	Response of complex model without viscera to $10G_z$	142
36	Response of complete model to $10G_z$	144
37	Frontal impact deformed configurations	148
38	Comparison of head acceleration for symmetric and eccentric head mass	157
39	Comparison of C5/C4 axial force for symmetric and eccentric head mass	158
40	Comparison of C5/C4 sagittal plane moment for symmetric and eccentric head mass	159
41	Comparison of C5/C4 left facet force for symmetric and eccentric head mass	160

		<u>Page</u>
42	Comparison of C5/C4 right facet force for symmetric and eccentric head mass	161
43	Back view of 80 msec configuration for eccentric head mass	162
44	Side view of 80 msec configuration for eccentric head mass	163

LIST OF TABLES

<u>Table</u>		<u>Page</u>
1	Dilatation-displacement matrix [E] for hydrodynamic element	59
2	Flowchart for explicit direct integration procedure	67
3	Flowchart for implicit direct integration procedure	77
4	Coordinates of typical lumbar and thoracic vertebra	83
5	Geometry of spine	85
6	Stiffness properties of intervertebral discs	92
7	Lines of action of articular facet elements in undeformed configuration	95
8	Costo-vertebral geometry	99
9	Rib geometry	100
10	Stiffness properties of deformable elements in rib cage	101
11	Inertial properties for isolated ligamentous spine	104
12	Summary of maximum stress calculations	110
13	Inertial properties for complete model	112
14	Comparison of response for 30° angle and vertical ejection	137
15	Effect of rib cage and viscera on response of spine under 10G _z	145
16	Natural frequencies of spine models	150
17	Cervical forces with increased head mass	154
18	Standard elements	201

CHAPTER I
INTRODUCTION

1. Objectives

The spine is the primary structural element for transmitting forces to the upper torso and head in high acceleration environments such as pilot ejection. Thus in the study of ejection response, it is common to model the element for force transmission by a bar or beam and to neglect the torso and rib cage. These bar-beam models have evolved into two general classes: the so-called continuum models, in which the bar is considered as homogeneous, and the discrete models, in which the individual vertebrae are represented as rigid bodies and are connected in series by deformable elements, which represent the intervertebral disc and other connective tissues. These two types of models are in fact very similar in character, for if the scale of discretization employed in the homogeneous models is comparable to the number of vertebral levels, the difference equations of the homogeneous models will be very similar to that of the discrete models. The primary distinction between the two types of models lies in the possibility of directly using disc and ligament properties in the discrete models, whereas the continuum models require determination of extrapolated material properties, which represent the composite behavior of the discs and vertebrae. Both the discrete models and homogeneous bar-beam models that have been developed so far have been restricted to one or two dimensional behavior.

The principal objective of this investigation is the development of a three dimensional, discrete model of the spine and head.

In addition, the model was developed in a manner so that other aspects of the torso, such as the rib cage and viscera, could be modelled and their effects on the behavior of the spine investigated. This interaction of the spine with the torso is particularly important in responses which involve substantial flexure of the spine, for the flexural stiffness of the spine is very low, and as shown in results to be presented subsequently, are not sufficient to insure the stability of the spine in acceleration environments commonly found in pilot ejection. Significant flexure may be induced either by initial curvatures of the spine, or by asymmetric properties, such as asymmetric mass distribution. Thus the ability to investigate the behavior of the spine in situations involving substantial bending is of practical importance.

Because the treatment of elements, such as for example, the rib cage, in sufficient detail to accurately represent its behavior in a wide variety of situations involves substantial computational effort, the model has been developed so that portions of it may be replaced by simplified representations. These simplified representations are quite effective in a more limited range of situations. Thus, the rib cage can be replaced by an equivalent beam model, and a detailed representation of the cervical vertebrae can be replaced by a single beam element. These simplifications provide significant savings in computer time, and are therefore quite valuable when parametric studies are undertaken.

A general description of the characteristics of the model is given in the third section of this chapter. The details of the mathematical formulation, material properties, and anatomical repre-

sentation are given in the next three chapters. Some of the more interesting and significant results obtained during the course of this study are then described. Finally, the input data formats for both the dynamic simulation and the graphics package are given in the Appendices.

2. Literature Review

To put this work in proper perspective, we will first review previous models of the spine, using the customary classification of continuous and discrete models. Latham (1957) is usually cited as the first to develop a mathematical model for describing the dynamic response of the spine to $+G_z$ acceleration. Latham's one degree of freedom model consisted of the rigid masses representing the body and the ejection seat, interconnected by a spring. It was developed to study the dynamic overshoot of the body when seat cushions of varying resiliency were placed between the pilot and the ejection seat. Also included in Latham's work is the first study concerning the natural frequency response of the human body in the seated position.

Payne (1961) also developed a discrete, one degree of freedom model of the spine. A rigid mass was used to represent the head and upper torso, and the spine was modelled as a spring with a dashpot in parallel. The stiffness of the spring was chosen to match the lowest axial natural frequency of the human body as predicted from the lowest peak in the axial driving point impedance measurements. Although this single spring model could not predict

the force distribution in the spine, it was and still is considered an accurate representation of the dynamic response associated with the acceleration profile of the ejection seat. Subsequently, an eight degree of freedom model was developed by Toth (1966). It consisted of rigid masses representing vertebrae T11 through L5 and the pelvis, interconnected by springs and dampers which represented the intervertebral discs. This was the first use of multiple mass, damped spring models and the first discrete model to idealize individual discs.

Orne and Liu (1970) proposed the first model that included the shear and bending resistance of the intervertebral disc. The model employed a small strain, large displacement formulation. Each of the vertebrae, T1 through L5, was represented as a rigid body in two dimensional space with three degrees of freedom per vertebra. Spinal curvature and variations of disc stiffness with vertebral level were treated. A three parameter viscoelastic force-deflection relation was used to represent the material properties of the intervertebral discs. Orne and Liu were also the first to model the inertial properties by assigning to each motion segment the total inertia of the associated segment of the torso. Although this appears somewhat unreasonable in that the motion of the viscera, because of its low shear stiffness, is obviously quite different from the motion of the vertebrae, it was quite successful in duplicating the characteristics of experimentally observed response and has been used by many other investigators. The success of this procedure may be explained in terms of added masses resulting from the stiffness of the viscera: thus, it is

similar to the "added mass" technique used to analyze the vibration of structures within a fluid. Also included in the model was the eccentricity of the mass center for each motion segment, which was assumed to be uniform along the spinal column with each segment having the same inertial properties. The model did not include the interactions of the spine with the torso, ejection seat, or harness apparatus. Failure to represent these interactions in a large displacement formulation results in unrealistic deformed configurations of the spinal column and may invalidate the force distributions predicted by the model.

Prasad and King (1974) extended the Orne and Liu model by including the articular facet interaction. The motivation for this extension was to model a secondary load path in the spinal column which is effected by the articular facets as indicated by the experimental work of Prasad, et al. (1973). The interaction of the articular facets was modelled by two springs, one limiting relative rotations and the other limiting the relative sliding of adjacent vertebrae.

Stiffness values for the articular facets appear to have been chosen rather arbitrarily, since no reference is made as to how the axial stiffness was determined and no value for the rotational stiffness is cited. Of the axial facet stiffness values listed, the largest values are assigned in the lumbar region and are of the same order of magnitude as the disc axial stiffness. Such large stiffness values may be realistic in certain directions, where the facet effectively imposes a kinematic constraint. However, the deformation-resisting character of the facet joint in

other directions should be modelled with a much lower stiffness value, as pointed out by Schultz, et al. (1973). Also included in the model is an auxiliary force representation of the ejection seat and harness interaction, although the details of this aspect of the model were not described.

A parallel history can be traced in the homogeneous (or continuum) models. The first continuum model was proposed by Hess (1956), who included only axial response. Subsequently, Moffat, et al. (1971) included both axial and bending response by using a beam type model. However, the analysis was restricted to small displacements.

Recently, Liu, et al. (1973) developed bar-beam models, including large displacements in the analyses. The stiffness properties of this model were based on that of the isolated, ligamentous spine and the responses they exhibited demonstrated very large deflections.

3. General Description of Model

The model represents the human body by a collection of rigid bodies interconnected by deformable elements. The rigid bodies are used for the modelling of bones, while the deformable elements are used to model ligaments, muscles and connective tissues. The treatment of bones as rigid bodies is preferable from both the viewpoint of numerics and modelling, for the stiffness of bones is usually orders of magnitudes greater than that of connective tissue, so that if both are modelled as deformable,

the resulting numerical problem is poorly conditioned. However, long slender bones, such as ribs, may be modelled as deformable. The deformable elements may also be used to model entities external to the body, such as restraint systems and harnesses.

For purposes of describing the model, it is worthwhile to distinguish between the following:

- 1) The computer-based method of solution, or mathematical model, which is a rather general system for the treatment of the dynamics of collections of rigid bodies interconnected by deformable elements, and
- 2) The specific models of the spine, torso and ejection system, which constitute a data base for the computer system.

We will first describe in general terms the mathematical model employed in the computer simulation. This is followed by a general description of the data sets which have been developed for modelling the spine, head, and torso in ejection problems.

4. Mathematical Model

The computer procedure is basically a matrix structural analysis technique, which serves as a versatile framework for constructing the equations of motion. The program enables these equations of motion to be integrated in time by either explicit or implicit techniques, or analyzed by modal procedures, which give the natural frequencies and modes of the model. The formulation is completely three dimensional and treats arbitrarily large rotations and displacements of the rigid bodies. However,

the deformation of some of the elements is restricted to be moderately small. Material properties may be linear or nonlinear and linear viscous forces can be included.

Nodes and Coordinate Systems. Two types of nodes are used:

- a) primary nodes, each of which has six degrees of freedom consisting of three translations and three rotations; the centroid of a rigid body must be a primary node;
- b) secondary nodes, each of which is connected through a rigid body to a primary node and which thus has no independent degrees of freedom.

An arbitrary number of secondary nodes may be associated with any rigid body, and they serve principally as a means of connecting deformable elements to a rigid body at a point other than the centroid.

The configuration of the model is described by the position and orientation of the primary nodes. The original position of node I is denoted by x_{iI}^0 ($i=1$ to 3 representing the x, y, and z components); the new position x_{iI} are obtained by adding the displacements u_{iI} , so

$$x_{iI} = x_{iI}^0 + u_{iI} \quad (1.1)$$

The orientation of a primary node is described by a triad of orthogonal unit vectors \vec{b}_{1I} , \vec{b}_{2I} , \vec{b}_{3I} , which rotate with the node.

In order to describe the system, we will define three types of coordinate systems:

1. a fixed, global set of coordinates (x, y, z), or x_i ;

2. body coordinates $(\bar{x}, \bar{y}, \bar{z})_I$; a set of body coordinates is associated with each primary node, so that \bar{x} , \bar{y} , and \bar{z} coincide with \vec{b}_{1I} , \vec{b}_{2I} , and \vec{b}_{3I} , respectively for each node. The origin of the \bar{x}_{iI} system must be the centroid of the mass at node I;
3. element coordinates $(\hat{x}, \hat{y}, \hat{z})$; a set of element coordinates is associated with each element, and the element coordinates rotate and translate with the element in a manner to be specified later. The \hat{x} , \hat{y} , and \hat{z} axes are associated with unit vectors \vec{e}_1 , \vec{e}_2 , and \vec{e}_3 , respectively for each element.

Model Elements. The model consists of the following elements:

1. rigid bodies
2. spring elements
3. beam elements
4. hydrodynamic elements
5. elastic surfaces

Rigid Bodies. Each rigid body may be arbitrarily oriented in three dimensional space and may undergo arbitrarily large rotations and translations. The centroid of the rigid body is designated a primary node, (see Fig. 1), its coordinates in space define the position of the rigid body. Each rigid body has both translational and rotational inertia. The orientation of the rigid body is described by the triad of orthogonal unit vectors \vec{b}_1 , \vec{b}_2 , and \vec{b}_3 . These vectors must coincide with the principal axes of the moment of inertia. The moments of inertia about \vec{b}_1 , \vec{b}_2 , and \vec{b}_3 are I_1 , I_2 , and I_3 , respectively. In

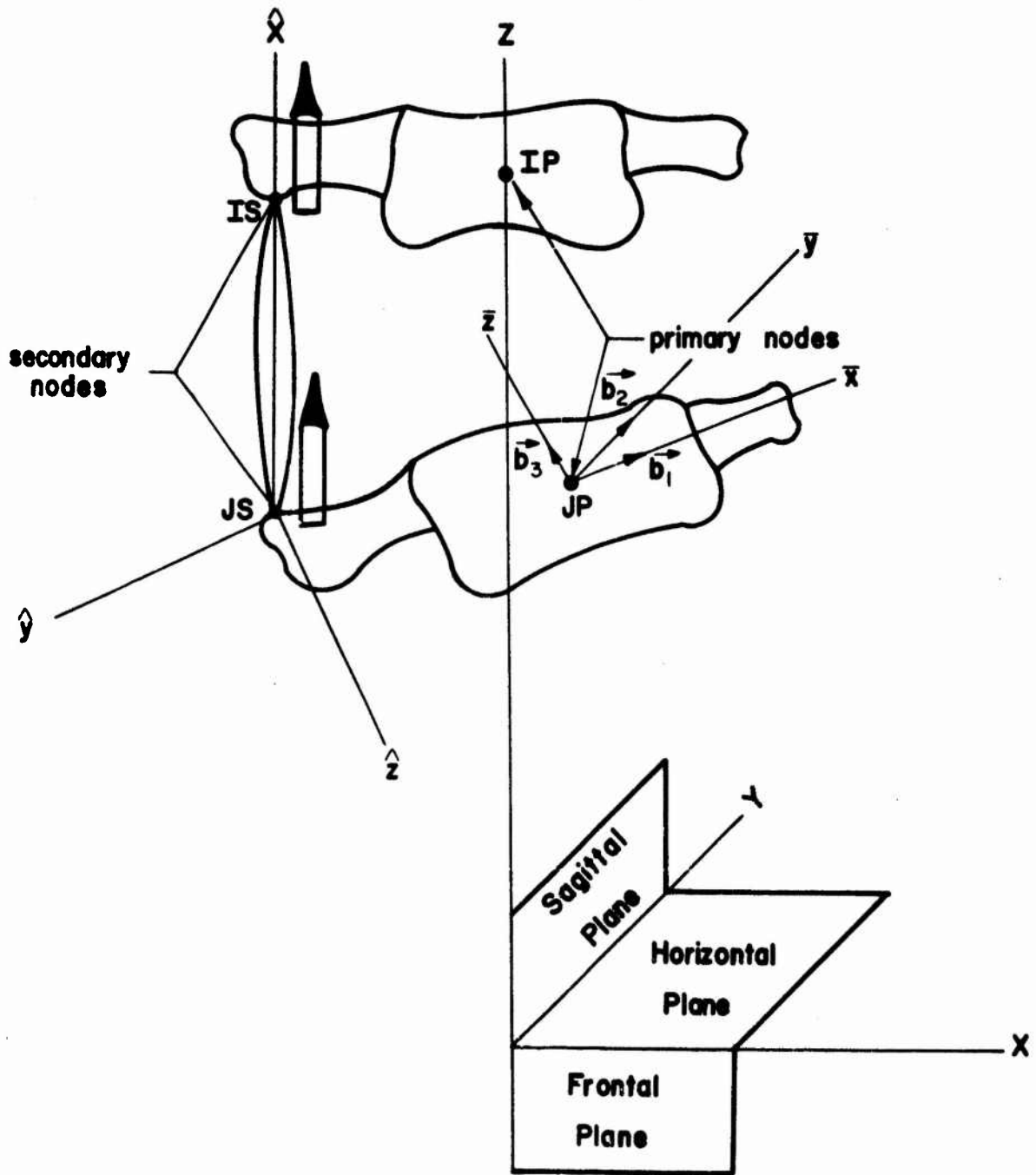


Figure 1. Rigid body representation and coordinate systems: global coordinates (x, y, z) ; body coordinates $(\bar{x}, \bar{y}, \bar{z})$ and element coordinates $(\hat{x}, \hat{y}, \hat{z})$.

addition to the primary nodes, any number of secondary nodes may be associated with the rigid body.

Spring Elements. Spring elements are deformable elements with only axial stiffness, which may interconnect any two nodes of the system. A typical spring element is shown in Fig. 2.

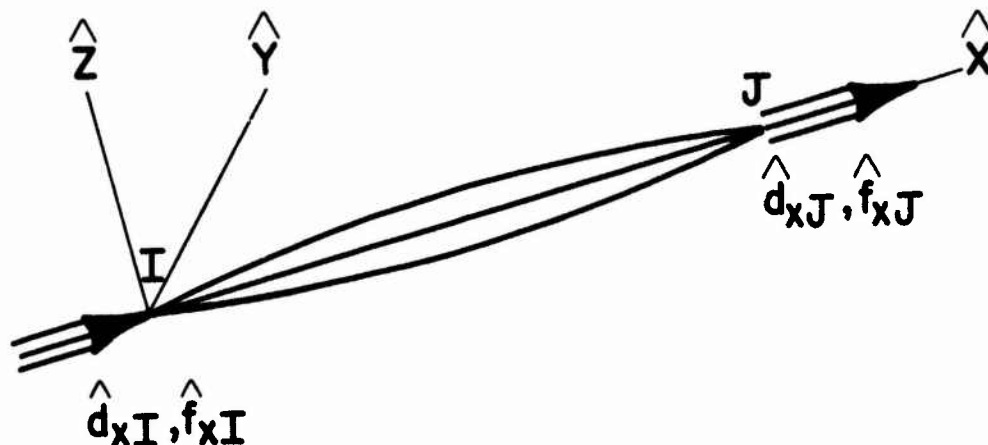


Figure 2. Spring Element

The element may be connected to either primary or secondary nodes. The axial force in the element will be denoted by T , with T positive in tension; the elongation is designated by δ . The axial force-elongation law is

$$T = k_1 \delta + k_2 \delta^3 \quad (1.2)$$

where either k_1 and k_2 may be zero. A tension cutoff

may be added to that $T = 0$ whenever $\delta < 0$; this is useful for ligaments and other elements that become slack whenever the elongation is negative.

Beam Element. A beam element may interconnect any two nodes, which may be either secondary or primary nodes. Beam elements include axial stiffness, torsional stiffness and bending stiffness. The resulting nodal forces are shown in Fig. 3: \hat{f}_{xI} and \hat{f}_{xJ} arise from axial stiffness, and \hat{m}_{yI} , \hat{m}_{zI} , \hat{m}_{yJ} and \hat{m}_{zJ} arise from the bending stiffness about the two principal coordinates of the cross-section, \hat{y} and \hat{z} , and \hat{m}_{xI} arises from torsional stiffness. For all moments, the right hand rule sign convention is used as shown in Fig. 3.

The orientation of the \hat{y} and \hat{z} axes is given by including a third node for each beam element, called an orientation node, that lies in the \hat{y} - \hat{x} plane of the original orientation of the beam.

There are two available modes for computing the forces and moments in the beam. In the first mode, functional forms are assumed for the overall response of the beam; these are not consistent with any homogeneous material properties but allow the introduction of certain nonlinearities. The forms are:

axial force

$$\hat{f}_{xJ} = T = k_1^a \delta + k_2^a \delta^3$$

$$\text{optional } T = 0 \quad \text{if } \delta < 0 \quad (1.3)$$

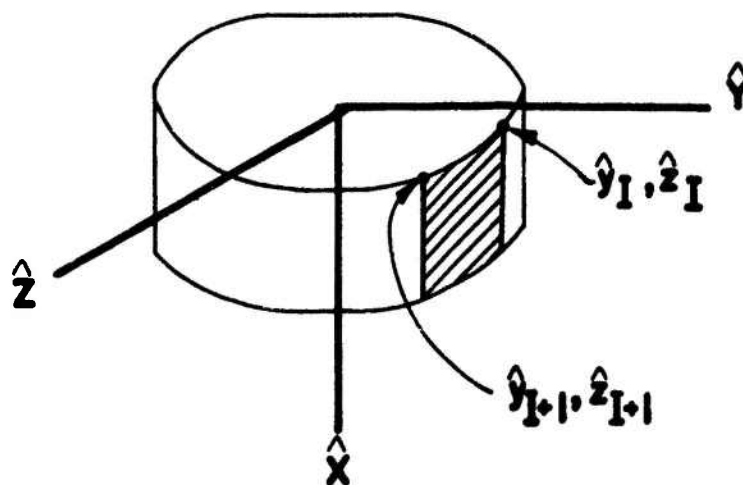
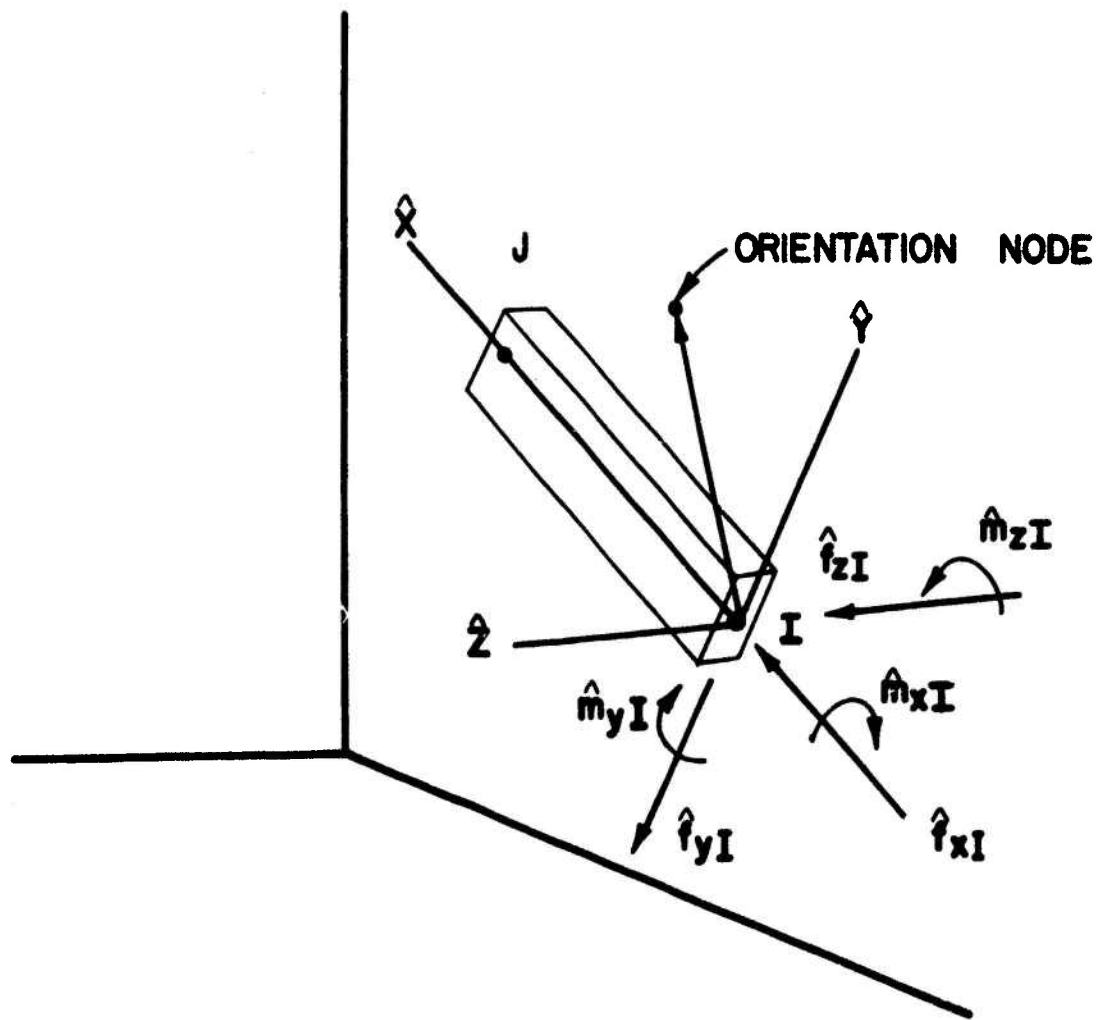


Figure 3. Beam Element

bending in \hat{x} - \hat{z} plane

$$\begin{Bmatrix} \hat{m}_{yI} \\ \hat{m}_{yJ} \end{Bmatrix} = \frac{k_y^b}{1+\phi_y} \begin{bmatrix} 4+\phi_y & 2-\phi_y \\ 2-\phi_y & 4+\phi_y \end{bmatrix} \begin{Bmatrix} \hat{\theta}_{yI} \\ \hat{\theta}_{yJ} \end{Bmatrix} \quad (1.4a)$$

bending in \hat{x} - \hat{y} plane

$$\begin{Bmatrix} \hat{m}_{zI} \\ \hat{m}_{zJ} \end{Bmatrix} = \frac{k_z^b}{1+\phi_z} \begin{bmatrix} 4+\phi_z & 2-\phi_z \\ 2-\phi_z & 4+\phi_z \end{bmatrix} \begin{Bmatrix} \hat{\theta}_{zI} \\ \hat{\theta}_{zJ} \end{Bmatrix} \quad (1.4b)$$

For linear homogeneous materials, the bending constants are given through standard engineering analysis by

$$k_y^b = \frac{E I_{yy}}{\ell} + \frac{1}{4} a_1 (|\hat{\theta}_{1y}| + |\hat{\theta}_{2y}|)^2 \quad (1.5)$$

$$k_z^b = \frac{E I_{zz}}{\ell} + \frac{1}{4} a_2 (|\hat{\theta}_{1z}| + |\hat{\theta}_{2z}|)^2$$

where E is Young's modulus, ℓ the length of the element, and I the section moduli, which are respectively

$$I_{yy} = \iint_A \hat{z}^2 d\hat{y}d\hat{z} \quad I_{zz} = \iint_A \hat{y}^2 d\hat{y}d\hat{z} \quad (1.6)$$

where the integral is over the cross-sectional area of the element, A . The shear factor is given by

$$\phi = \frac{12EI}{G A_s \ell^2} \quad (1.7)$$

where G is the shear modulus and A_s the effective area in shear. The constants a_1 and a_2 are included to permit an approximation to a cubic moment-curvature behavior.

The second method of computing the bending moments and axial force in the beam requires the cross-section of the beam to be defined as a thin-walled member. The cross-section is defined by the coordinates $\hat{y}_i, \hat{z}_i, i = 1$ to NI , and the shape is assumed to be prismatic, so that \hat{y}_i, \hat{z}_i are constant with respect to \hat{x} . If this mode is used, the moments are computed directly from the axial stresses σ by numerical integration. An arbitrary stress strain law of the form

$$\sigma = k_1^S \epsilon + k_2^S \epsilon^3 \quad (1.8)$$

may be used, with the option of tension cutoffs. No shear corrections are made. This mode is useful for modelling elements such as the walls of the torso.

In both modes, the torsional resistance is taken to be a linear function of the torsional deformation and independent of the other stresses in the element, i.e.

$$\hat{m}_x = k^t \hat{\theta}_{xIJ} \quad (1.9)$$

where \hat{m}_x is the torque, k^t the torsional spring constant and $\hat{\theta}_{xIJ}$ the torsional deformation. The shear forces are always obtainable from equilibrium so no force-deflection law is necessary.

Hydrodynamic Element. This element is illustrated in Fig. 4. The element is a pentahedron, with the two opposing triangular faces considered to be rigid. The three nodes of each triangular face must therefore be associated with the same primary node. There

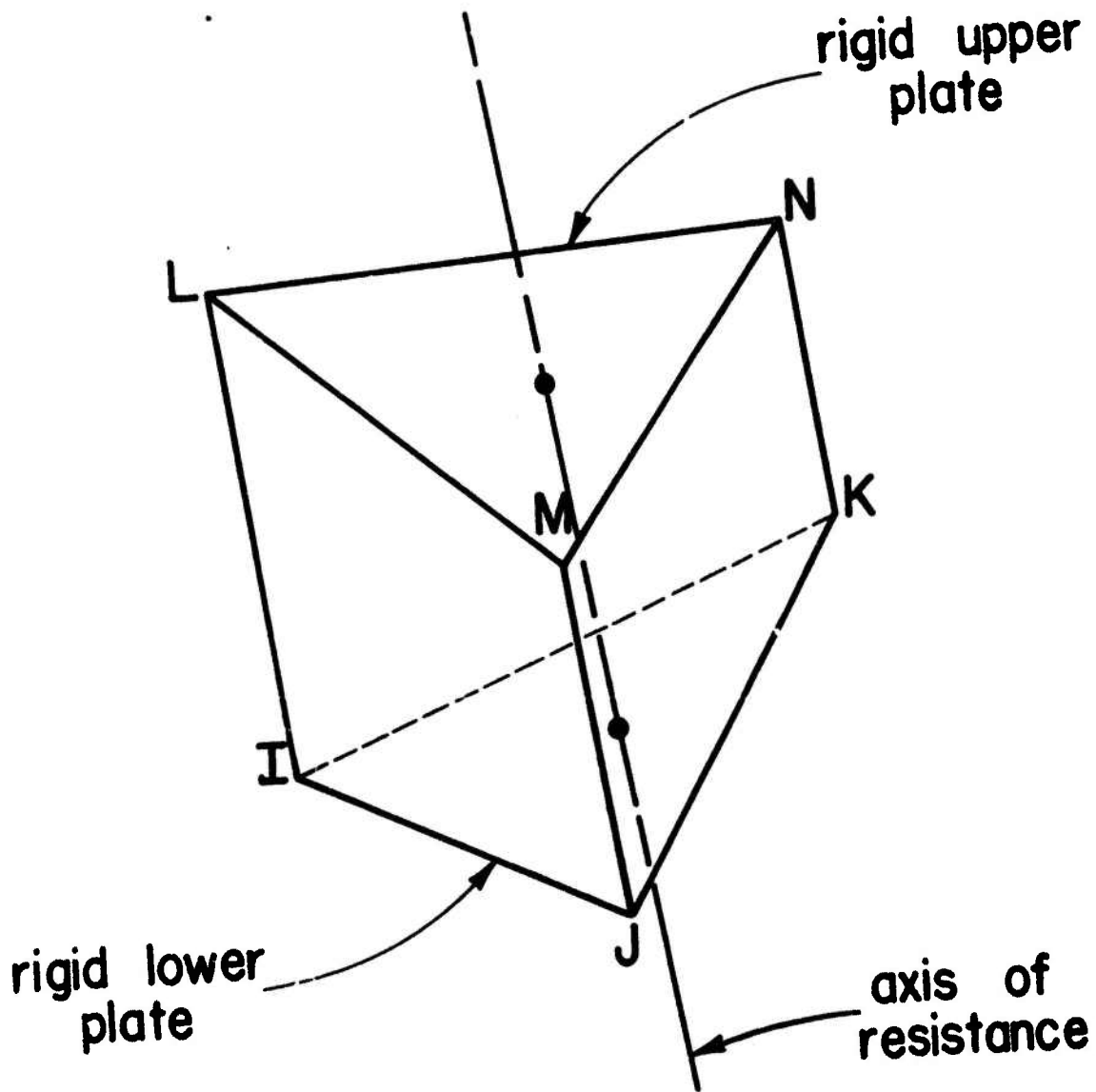


Figure 4. Hydrodynamic element.

are no restrictions on the geometry of the element, other than that the initial volume of the element be positive: this is insured by numbering the nodes appropriately.

The force deflection characteristics of this element are obtained from a linear pressure-dilatation relationship. The pressures are transmitted through the rigid triangular plates to the associated primary node in an energetically consistent fashion. In addition to the linear pressure-dilatation stiffness, a linear viscosity is available.

This element is useful for modelling components of the body that exert resistance primarily to compressive deformations. Because of the presence of the rigid plates, the resistance tends to be directed through a line of action connecting the centroids of the two triangular surfaces. Thus it is useful for modelling articular facets, which have very strong directional properties, and the viscera that effect resistance primarily through a vertical axis.

Elastic Planes. An assemblage of planes may be prescribed in the model to represent surfaces of the pilot's seat. Each plane is described by locating three points on the plane, as shown in Fig. 5. The planes restrain the motion of the nodes so that when a node penetrates the plane, a force proportional to the extent and rate of penetration is applied to the node in a direction normal to the plane.

All planes are considered to be rigidly linked together. The

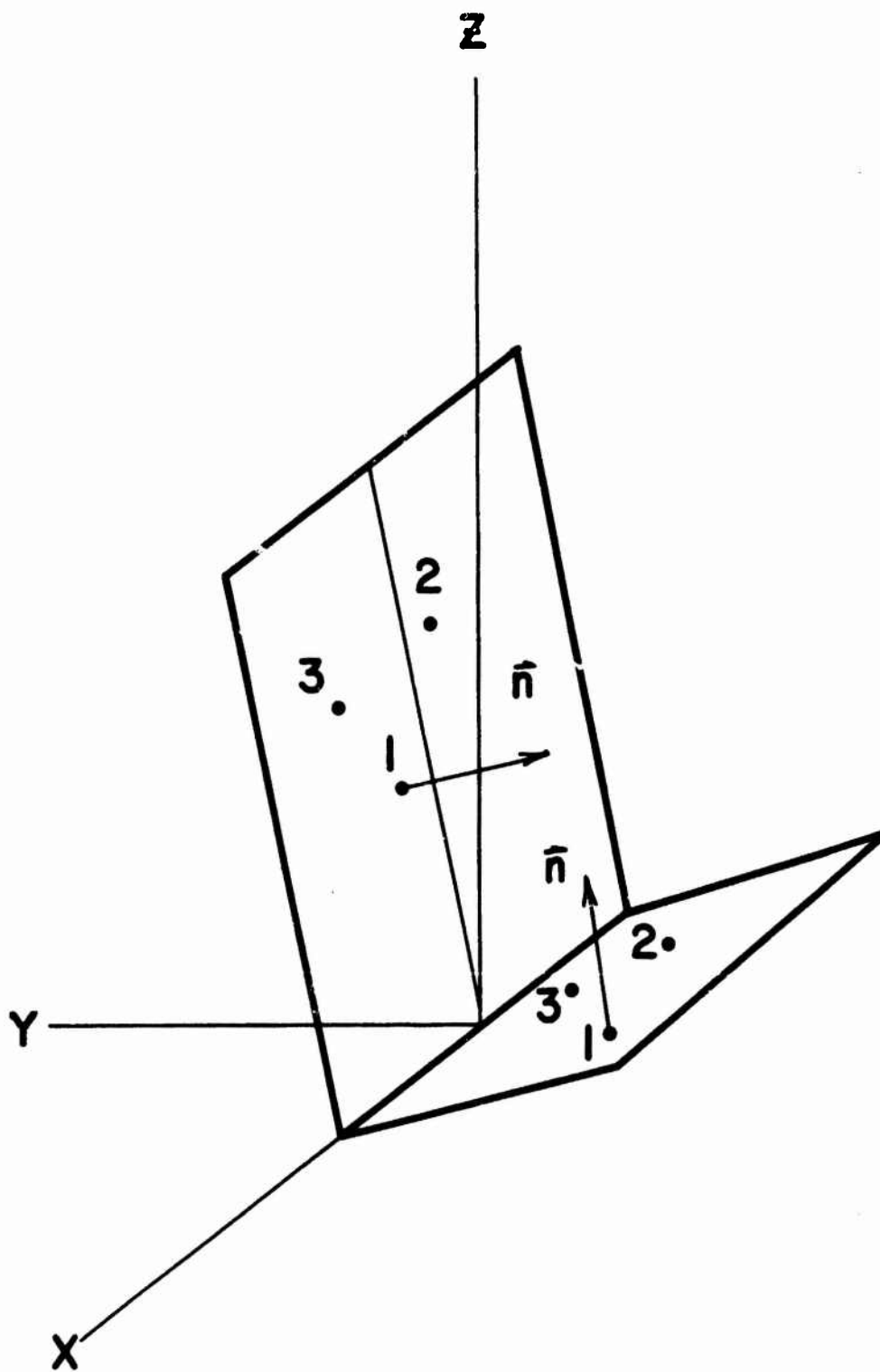


Figure 5. Seat model representation.

motion of this assemblage of planes is prescribed through either acceleration, velocity, or displacement histories.

5. General Description of Models

For purposes of illustrating how the mathematical model is used to represent the pilot's anatomy, we will here describe two representative models that have been used in these studies. The first model is restricted to the isolated throacolumbar spine, the cervical spine, the head, the seatback and restraint system. The second model, in addition to the preceding, includes a representation of the rib cage and viscera.

The first model is graphically depicted in Figs. 6 and 7, which show a back view and a side view of the model in the seated position, respectively. In all models described in this report, the standard orientation for the global coordinate system is as follows: the z-axis is positive vertically upward, the y-axis is positive towards the back and the x-axis is oriented sideways; thus the y-z plane corresponds to the sagittal plane, the x-z plane corresponds to the frontal plane and the x-y plane corresponds to the horizontal plane.

The graphical depiction in Figs. 6 and 7 show only the rigid bodies employed in the model. Each vertebra and the head is represented as a rigid body. The configuration of these rigid bodies are prescribed by the initial position of the primary nodes in x, y, z space: each primary node must coincide with the mass center of the rigid body. The positions of the primary nodes are

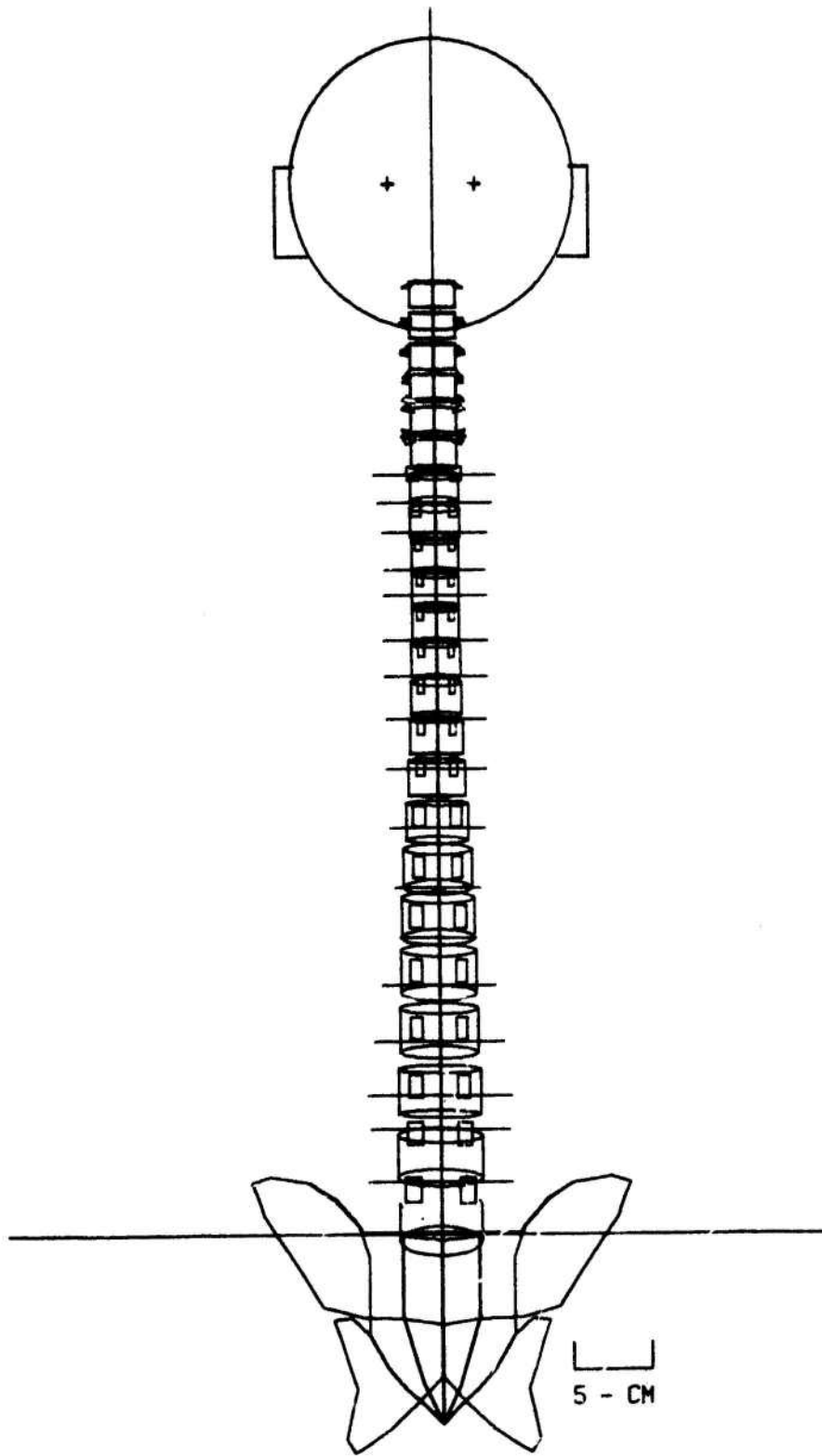


Figure 6. Back view of isolated ligamentous spine model.

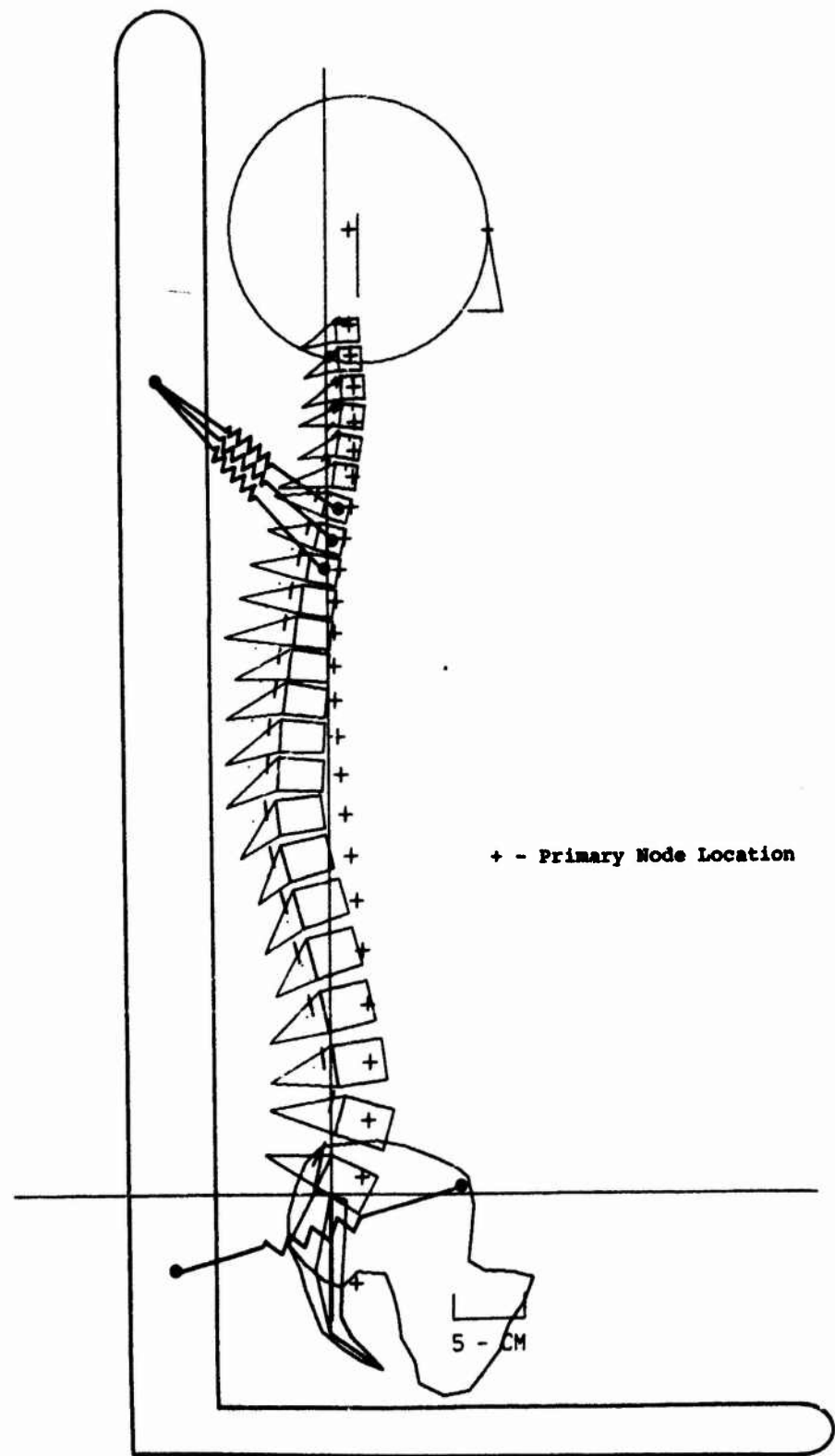


Figure 7. Side view of isolated ligamentous spine model.

indicated in Fig. 7 by plus signs. As can be seen from the figure, the primary nodes in many cases do not lie within the vertebrae because the Liu, et al (1973) segment data was used to represent the inertial properties of the body in this model, so that each vertebra is associated with a segment of the torso.

The conceptualization used in modelling the inertial properties of the human body differs markedly from that used in modelling the stiffness properties. The stiffness model considers each vertebra as a rigid body, with the spring elements and beam elements interconnecting these rigid bodies in a manner so as to approximate force deformation characteristics of the human body. On the other hand, from an inertial viewpoint, each rigid body represents a segment of the complete torso, and each vertebrae is considered to be rigidly embedded in an associated segment of the torso. This corresponds to the inertial approximation developed by Orne and Liu (1971) and used by Prasad and King (1974). The more complex models do not use this approximation, but as a consequence, are based on less reliable data.

In the thoracolumbar spine, each pair of vertebrae is connected by seven spring elements and one beam element. The intervertebral disc is represented by a beam element, which joins the geometrical centers of the endplates of each pair of adjacent vertebrae. The spring elements represent the following ligaments and connective tissues: the pair of spring elements which connect the transverse process tips represent the intertransverse ligaments; one spring element, which connects the spinous process tips, represents the intra- and supra-spinous ligaments; a pair of

elements which connect posterior points on the vertebral bodies, represent the ligamenta flava; two spring elements are used to represent the articular facets. The latter are short, stiff elements and are primarily intended to represent the kinematic constraints resulting from the facets. All of these elements interconnect secondary nodes on the rigid body. In addition, the primary nodes are connected by additional beam elements which represent the stiffness of the torso and rib cage. Cubic moment curvature relations are used in these elements so that their bearing on small-displacement response is negligible. Details as to the locations of the nodal points and the material properties of the deformable elements may be found in Chapter IV.

In the cervical spine, adjacent vertebrae are connected only by elements representing the disc, the interspinous ligaments, and the articular facets. The discs are represented by beam elements, the ligaments by spring elements, the articular facets are represented by hydrodynamic elements. The triangular endplates of the hydrodynamic element may be seen in Figs. 6 and 7. Because these elements have resistance primarily through a line joining the centroids of the two opposing triangular facets, these elements are more effective in representing the directional properties of articular facets than spring elements. The use of these elements for the representation of the facets would also be desirable in the lumbar and thoracic spines, but the procurement of data for the location of the facet planes in these portions of the spine has not been completed.

The head is a single rigid body joined to C2 by a beam

element (C1 was not included in the model). In all the simulations studied here, the helmet was assumed to move exactly like the head, so that if a helmet was included in the study, the moment of inertia and mass of the helmet was simply added to that of the head.

The seatback in this model is a plane surface, which is vertically aligned and the bottom of the seat is horizontal. The seat constrains the motion of the rigid bodies only when they come in contact. The definition of the seatback is quite arbitrary, as long as it can be described as a series of planes, so that alternative seatback designs can be studied by the model by simply altering the description of these planes.

The restraint system in this model consists of 4 springs, 3 connecting the vertebrae T1, T2, and T3 with the seatback, the other connecting a secondary node on the pelvis with another point on the seatback. The upper restraint belt is represented by three springs to reduce the shear deformation. Again the positions of these nodes are indicated in Fig. 7. The orientations and method of interconnection for these elements is completely arbitrary so that other harness systems can be modelled. However, important aspects such as friction and the actual details of the geometry of the restraint system have not yet been included.

One of the more complex models is represented in Figs. 8 and 9, which show the back and side views, respectively. The major aims of this model are the separation of the inertial aspects of the torso from that of the spine, the inclusion of certain structural aspects of the rib cage, and the addition of an independent load path through the viscera. These aims were implemented

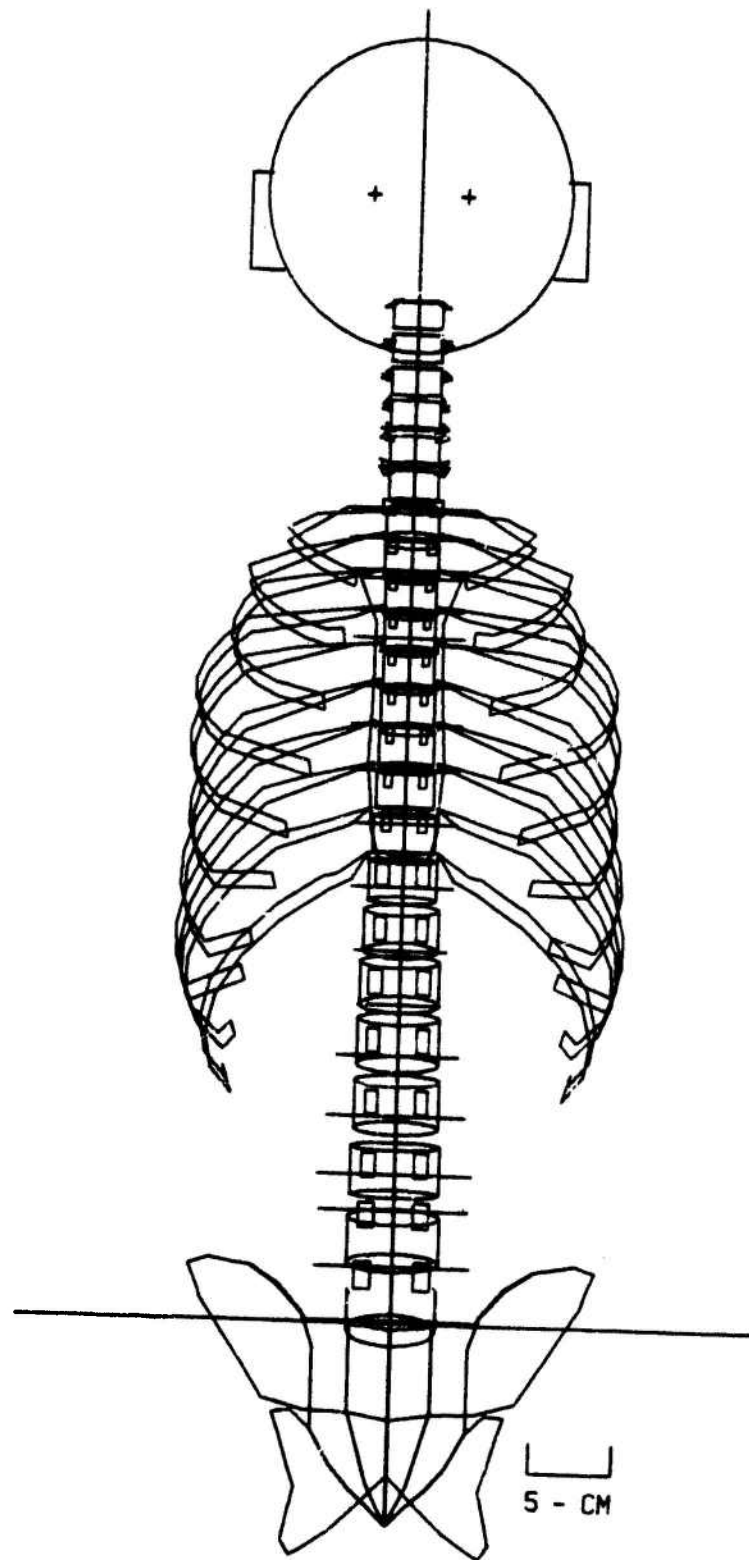


Figure 8. Back view of spine-torso model with rib cage.

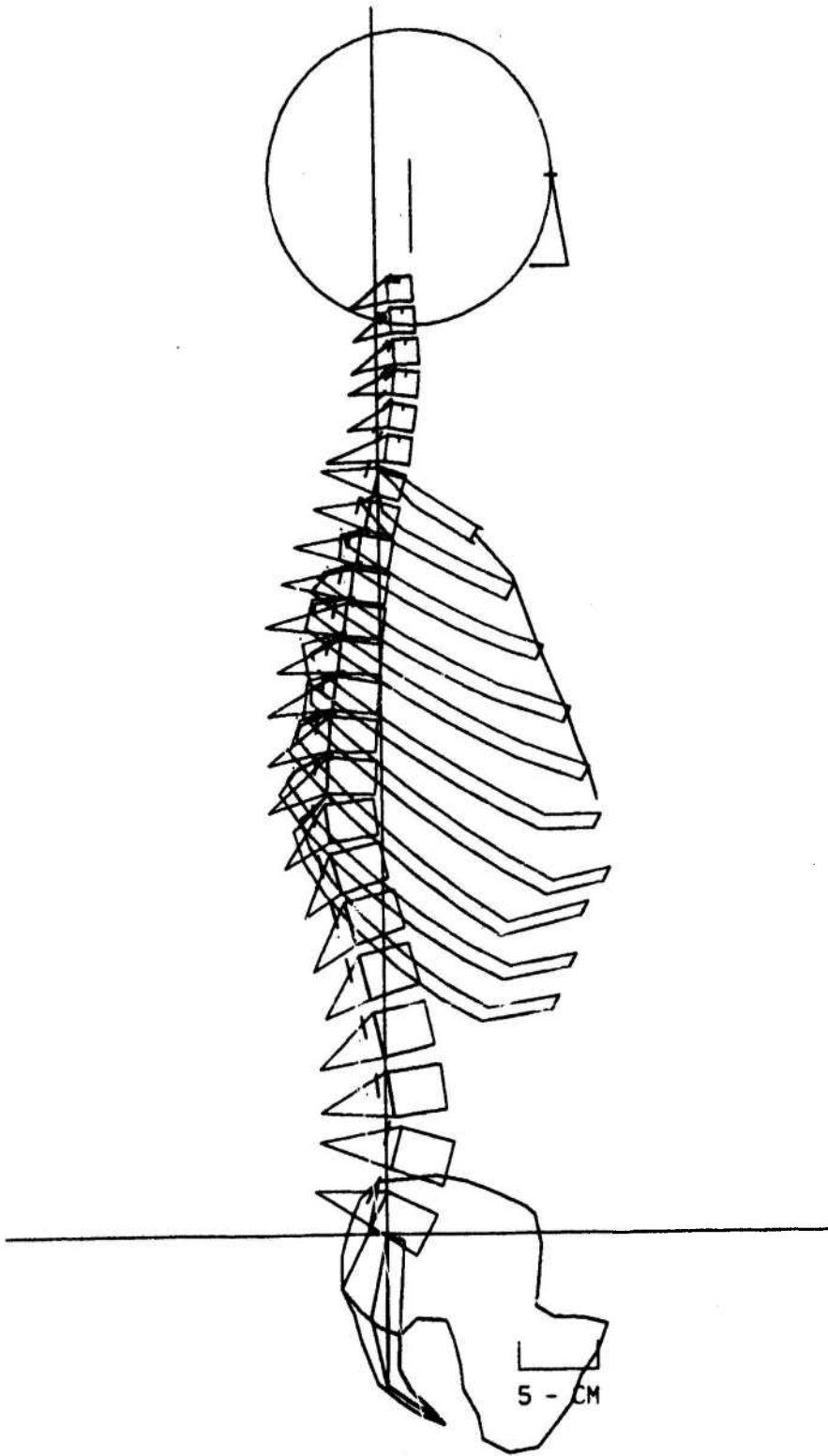


Figure 9. Side view of spine-torso model with rib cage.

as follows.

The rib cage is represented by a system of rigid bodies and deformable elements which includes separate rigid bodies for each of the ribs and the sternum. Since each rib is modelled as a rigid body, the deformation of the thorax as a whole results from the rotation of the ribs and the deformation of the costo-sternal cartilage. Each rib is connected to two vertebrae by means of three deformable elements, which represent the costo-vertebral joint. These deformable elements have been chosen so that the directional properties of the joint are represented and an axis of great rotational flexibility was included. The ribs are connected to the sternum through the costo-sternal joint by a deformable element, which represents the deformability of the costo-cartilage. This model is thus quite adequate for representing the additional bending stiffness of the torso that is provided by the rib cage; on the other hand, it is not suitable for representing frontal impact where significant deformations of the rib itself may take place. For the latter, it would be necessary to represent the deformation of the neck of the rib by modelling it by a beam element.

The viscera are represented by a stack of hydrodynamic elements, which are illustrated in Fig. 10. The hydrodynamic elements have stiffness only when deformed axially, so that this column does not have any resistance to shear. However because rigid endplates are included between each vertical layer of hydrodynamic elements, the system does resist bending and maintains coherence in response to transverse loads. The very bottom plate

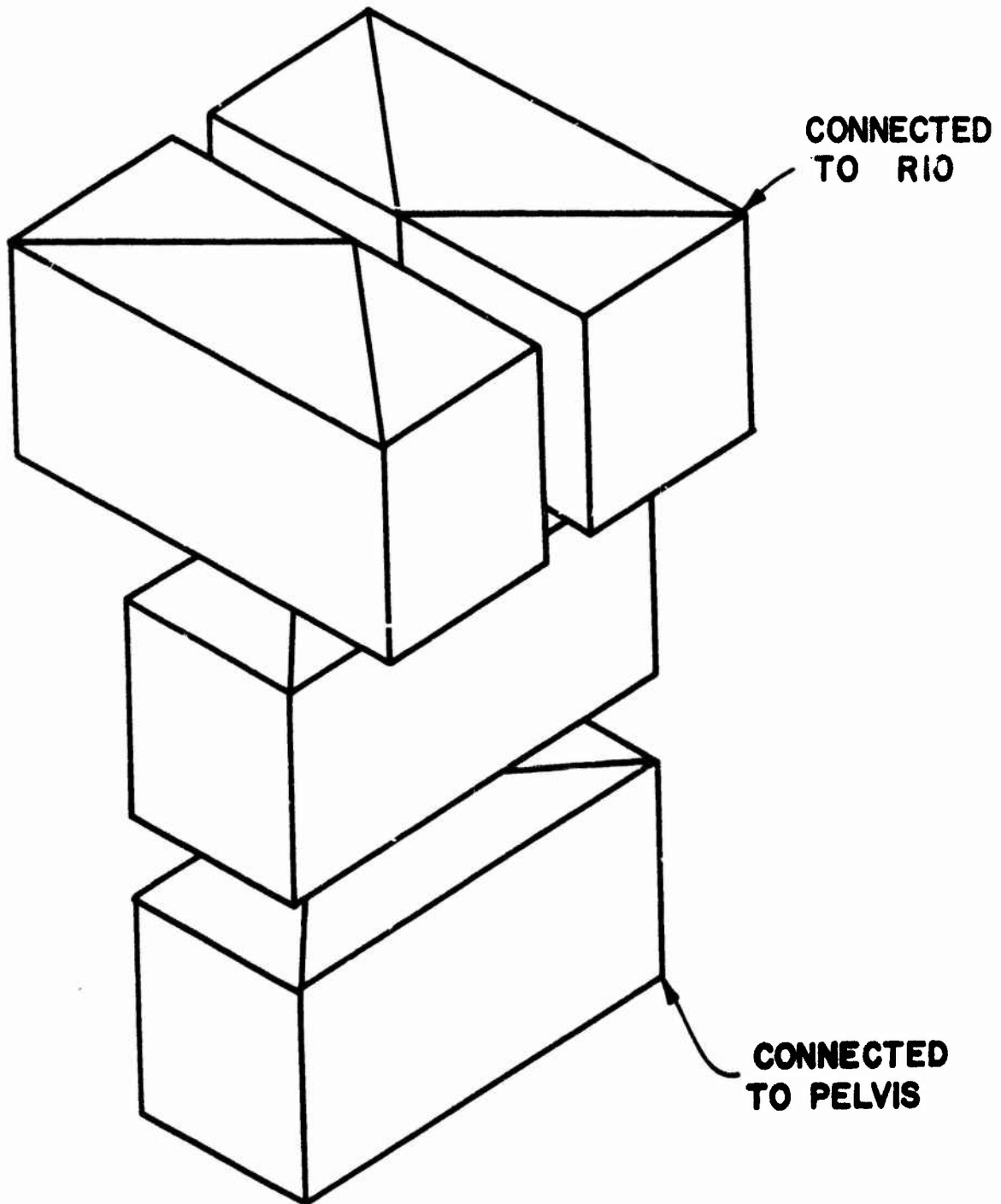


Figure 10. Viscera as modelled by hydrodynamic elements.

of the viscera is connected to the pelvis, whereas the uppermost plate is connected to ribs 10 on the left and right side; this interconnection represents the transfer of the load to the diaphragm. No hydrodynamic elements are included within the thorax.

The inertial properties of this model were obtained by subdividing the mass of each segment of the torso between the spine and the ribs and sternum in the thoracic regions, and between the spine and the viscera in the lumbar region. The distribution in each segment was chosen so that the total mass of each segment corresponds to the data of Liu, et al, and so that the moment of inertia of the masses of the components in each segment have a moment of inertia equal to that measured by Liu, et al. Because the mass of each body segment is partitioned into the inertia associated with the spine and the inertia of the thorax, the rotation of a body segment may differ from the rotation of an embedded vertebral body. The model of the thoracolumbar, cervical spine, head, seatback, restraints and pelvis are identical to that of the previous model. Both the details of the geometry and material properties may be found in Chapter IV.

CHAPTER II

MATHEMATICAL FORMULATION OF MODEL

1. Nomenclature and Coordinate Transformations

A general description of the modeling techniques has been given in Chapter 1. In this chapter, the detailed equations and mathematical procedures for the formulation and solution of the governing equations will be presented.

The coordinate systems have already been described in Chapter 1. In addition to a global coordinate system (x, y, z) , local coordinates for each element, $(\hat{x}, \hat{y}, \hat{z})_E$, and for each node, $(\bar{x}, \bar{y}, \bar{z})_I$, are used. The unit vectors for these coordinate systems are $(\vec{e}_1, \vec{e}_2, \vec{e}_3)_E$ for the coordinate system of element E and $(\vec{b}_1, \vec{b}_2, \vec{b}_3)_I$ for the coordinate system of rigid body I.

The unit vectors \vec{b}_{iI} and \vec{e}_{iE} immediately define the rotational transformation of any vector components between the coordinate systems. Thus, if we consider a vector \vec{A} with global components (A_x, A_y, A_z) , body coordinate components $(\bar{A}_x, \bar{A}_y, \bar{A}_z)$ and element coordinate components $(\hat{A}_x, \hat{A}_y, \hat{A}_z)$, we have the following transformations

$$\begin{pmatrix} A_x \\ A_y \\ A_z \end{pmatrix} = \begin{bmatrix} b_{1x} & b_{2x} & b_{3x} \\ b_{1y} & b_{2y} & b_{3y} \\ b_{1z} & b_{2z} & b_{3z} \end{bmatrix}_I \begin{pmatrix} \bar{A}_x \\ \bar{A}_y \\ \bar{A}_z \end{pmatrix} = [\lambda] \{\bar{A}\} \quad (2.1)$$

where b_{jx} , b_{jy} , b_{jz} are the global components of the body vectors.

Similarly,

$$\begin{pmatrix} A_x \\ A_y \\ A_z \end{pmatrix} = \begin{bmatrix} e_{1x} & e_{2x} & e_{3x} \\ e_{1y} & e_{2y} & e_{3y} \\ e_{1z} & e_{2z} & e_{3z} \end{bmatrix}_E \begin{pmatrix} \hat{A}_x \\ \hat{A}_y \\ \hat{A}_z \end{pmatrix} = [\mu] \{\hat{A}\} \quad (2.2)$$

where e_{ix} , e_{iy} , e_{iz} are the global components of the element vectors.

Also

$$\{\bar{A}\} = [\lambda]^T \{A\} \quad (2.3)$$

$$\{\hat{A}\} = [\mu]^T \{A\} \quad (2.4)$$

The translational motion of the system is described by the displacements u_{iI} , velocities \dot{u}_{iI} , and accelerations \ddot{u}_{iI} of the nodes.

Equations (2.1) to (2.4) can be written in indicial notation as

$$\begin{aligned} A_i &= \lambda_{ij} \bar{A}_j & \bar{A}_i &= \lambda_{ji} A_j \\ A_i &= \mu_{ij} \hat{A}_j & \hat{A}_i &= \mu_{ji} A_j \end{aligned} \quad (2.5)$$

The coordinate system in which a vector is expressed will henceforth be designated by the bars and hats. Thus the components of a vector \vec{A} in terms of the body coordinates of rigid body I are denoted by \bar{A}_{iI} , $i = 1$ to 3 denoting \bar{A}_{xI} , \bar{A}_{yI} , \bar{A}_{zI} , respectively. Furthermore, the set of three Cartesian components is often written as a matrix as in Eq. (2.3).

The orientation of a node is described by the unit vectors \vec{b}_{iI} , while the angular velocities and angular accelerations are treated in body coordinate components, $\bar{\omega}_{iI}$ and $\bar{\alpha}_{iI}$, respectively.

The forces and moments at the nodes are similarly denoted by F_{iI} and \bar{M}_{iI} , respectively, and may be subdivided into externally applied forces and moments, F_{iI}^{ext} and \bar{M}_{iI}^{ext} , and the forces and moments due to the resistance of the deformable elements, F_{iI}^{int} and \bar{M}_{iI}^{int} .

Only two unit vectors for the nodal coordinates, \vec{b}_{1I} and \vec{b}_{3I} , are stored per primary node. The third unit vector is then found by

$$\vec{b}_{2I} = \vec{b}_{3I} \times \vec{b}_{1I} \quad (2.6)$$

This method thus employs six numbers (three components of two vectors) to describe the three rotational degrees of freedom. Though this at first appears somewhat wasteful, it should be noted the alternative, a description by Euler angles, has serious shortcomings:

1. Euler angle formulations are not linearly independent for all values of the Euler angles.
2. The generalized moments corresponding to Euler angles are not easily interpreted in a physical sense.
3. The equations of motion and the transformations between body and global coordinates in terms of Euler angles are complex and computationally demanding because they involve many trigonometric functions.

All six components are stored, because if only a total of three of the six components of the two unit vectors were stored (with the remaining components computed from the fact that the two body vectors are orthogonal and unit vectors), then the remaining components would have to be determined from square roots. The signs of these components could not readily be determined.

Element nodal forces, moments, displacements and rotations are

denoted by \hat{f}_{iI} , \hat{m}_{iI} , \hat{u}_{iI} , and $\hat{\theta}_{iI}$, respectively, where I denotes the generic node number, which for each element ranges from 1 to the number of nodes in the element. Sometimes a superscript is used to indicate the pertinent element, i.e. $\hat{f}_{iI}^{(e)}$ are force components at node I of element e .

The inertial properties are described by the translational masses of the primary nodes, ρ_I , and the principal moments of inertia of the primary nodes, \bar{I}_{xxJ} , \bar{I}_{yyJ} , and \bar{I}_{zzJ} : The angular momenta of the nodes are then given by

$$\bar{L}_{jJ} = \bar{I}_{jkJ} \bar{\omega}_{kJ} \quad (\text{no sum on } J) \quad (2.7)$$

The element quantities are extracted from the global quantities in the usual manner by a Boolean connectivity matrix $\ell_{AI}^{(e)}$, so that

$$u_{iA}^{(e)} = \ell_{AI}^{(e)} u_{iI} \quad (2.8)$$

where

$$\ell_{AI}^{(e)} = 1 \quad \text{if the } A\text{th generic node of element } e \text{ corresponds to the } I\text{th primary node of the system.}$$

$$\ell_{AI}^{(e)} = 0 \quad \text{otherwise}$$

2. Derivation of Equations of Motion

We consider here the development of the equations of motion for the assemblage of rigid bodies and deformable elements. The equations are obtained from the principle of virtual work with the inertial forces included in a d'Alembert sense. The principle of virtual work, when applied to the system treated here, states that

$$\begin{aligned}
 \hat{u}_{iA}^{(e)} * \hat{f}_{iA}^{(e)} + \hat{\omega}_{iA}^{(e)} * \hat{m}_{iA}^{(e)} \\
 = \dot{u}_{iI} * F_{iI}^{ext} + \bar{\omega}_{iI} * \bar{M}_{iI}^{ext} \quad (2.9) \\
 - \rho_I \dot{u}_{iI} * \ddot{u}_{iI} - \bar{\omega}_{iI} * \dot{\bar{L}}_{iI}
 \end{aligned}$$

where the superscript e is summed over all elements, subscript A over all nodes of each element, and I over all primary nodes. Superscript dots denote time derivatives, while asterisks denote virtual quantities

The left hand side of Eq. (2.9) represents the rate of work expended on the deformable elements, that is, the internal rate of work, while the first two terms of the right hand side represent the rate of external work. The rate of work of the inertial forces is represented by the last two terms of the right hand side.

To obtain the equations of motion, the virtual nodal velocities of the element on the left hand side of Eq. (2.9) must be expressed in terms of the global virtual nodal velocities. In deriving these expressions we will separately consider the case when A is a primary node and when A is a secondary node.

When A is a primary node, the required relationships are obtained directly from Eq. (2.5), which gives

$$\hat{u}_{iA}^{(e)} = \mu_{ji} \ell_{AI}^{(e)} \dot{u}_{Ij} \quad (2.10)$$

$$\hat{\omega}_{iA}^{(e)} = \mu_{ji} \lambda_{jk} \ell_{AI}^{(e)} \bar{\omega}_{kI} \quad (2.11)$$

When A is a secondary node, the required relationships are developed as follows. We note that whenever A is a secondary node associated with a primary node J, then both nodes are points of a single rigid body, so that

$$\bar{\omega}_{iA}^{(e)} = \bar{\omega}_{jI} \quad (2.12)$$

and consequently Eq. (2.11) follows for the angular velocities. To obtain the counterpart of Eq. (2.10), we first designate the vector from I to A by \bar{X}_{iIA} . Because both points are on the same rigid body, the components of this vector in the body coordinates will not vary with time. The global components of this vector are given by

$$X_{iIA} = \lambda_{ij} \bar{X}_{jIA} \quad (2.13)$$

while the global components of the initial vector between I and A are given by

$$X_{iIA}^{\circ} = \lambda_{ij}^{\circ} \bar{X}_{jIA} \quad (2.14)$$

where the superscript nought denotes the original (i.e. at time zero) value of the variable. The displacement of the secondary node is then given by

$$\begin{aligned} u_{iA} &= X_{iA} - X_{iA}^{\circ} \\ &= X_{iI} + X_{iIA} - X_{iI}^{\circ} - X_{iIA}^{\circ} \end{aligned} \quad (2.15)$$

By substituting Eqs. (2.13) and (2.14) into Eq. (2.15), we find

$$u_{iA} = u_{iI} + \lambda_{ij} \bar{x}_{iIA} - \lambda_{ij}^{\circ} \bar{x}_{jIA} \quad (2.16)$$

Transforming the above to the body coordinates of body I and taking its derivative with respect to time, we find

$$\dot{u}_{iA} = \dot{u}_{iI} + \Omega_{ij} \bar{\omega}_{jI} \quad (2.17)$$

where

$$\Omega_{ij} = \begin{bmatrix} 0 & \bar{z}_{IA} & -\bar{y}_{IA} \\ -\bar{z}_{IA} & 0 & \bar{x}_{IA} \\ \bar{y}_{IA} & -\bar{x}_{IA} & 0 \end{bmatrix} \quad (2.18)$$

By again applying the appropriate transformations from Eqs. (2.5), we then find

$$\hat{u}_{iA}^{(e)} = \mu_{ji}^{\ell AI} \dot{u}_{jI}^{(e)} + \mu_{ji}^{\lambda} \lambda_{jk} \Omega_{k\ell}^{\ell AI} \bar{\omega}_{\ell I}^{(e)} \quad (2.19)$$

Eqs. (2.10), (2.11), and (2.19) hold both for the actual velocities and the virtual velocities. If we substitute these equations into the left hand side (LHS) of Eq. (2.9), using Eq. (2.10) whenever node A is a primary node and Eq. (2.19) whenever A is a secondary node, we obtain

$$\text{LHS} = \dot{u}_{jI}^* F_{jI}^{\text{int}} + \dot{\omega}_{kI}^* \bar{M}_{kI}^{\text{int}} \quad (2.20)$$

where

$$F_{jI}^{\text{int}} = \lambda_{AI}^{(e)} f_{jA}^{(e)} \quad (2.21)$$

$$\bar{M}_{kI}^{\text{int}} = \lambda_{AI}^{(e)} \bar{m}_{kA}^{(e)} \quad (2.22)$$

and

$$f_{Aj}^{(e)} = \mu_{ji} \hat{f}_{iA}^{(e)} \quad (2.23)$$

for both primary and secondary nodes A; while if A is primary

$$\bar{m}_{kA}^{(e)} = \lambda_{jk} \mu_{ji} \hat{m}_{iA}^{(e)} \quad (2.24)$$

and if A is secondary

$$\bar{m}_{kA}^{(e)} = \lambda_{lk} \mu_{li} \hat{m}_{iA}^{(e)} + \Omega_{jk} \lambda_{lj} \mu_{li} \hat{f}_{iI}^{(e)} \quad (2.25)$$

Equations (2.23) to (2.25) may be written in matrix form as follows

$$\{f^{(e)}\} = [\mu] \{\hat{f}\} \quad (2.26)$$

$$\{\bar{m}^{(e)}\} = [\lambda]^T [\mu] \{\hat{m}\} \quad (2.27)$$

$$\{\bar{m}^{(e)}\} = [\lambda]^T [\mu] \{\hat{m}\} + [\Omega]^T [\lambda]^T [\mu] \{\hat{f}\} \quad (2.28)$$

Thus for primary nodes, the nodal forces and moments are simply related by the coordinate transformations, while for secondary nodes an additional moment is introduced in the transformation because of the moment arm effected by the vector between the nodes. The total internal nodal forces are obtained from the terms given in Eqs. (2.23) to (2.25) by Eqs. (2.21) and (2.22). The latter equations just represent an appropriate summation of the element forces, for as can be seen from Eq. (2.8), $\ell_{IA}^{(e)}$ are Boolean matrices consisting of ones and zeroes.

The equations of motion are now obtained by substituting Eq. (2.20) into Eq. (2.9), which gives (after a change of dummy indices and collection of terms)

$$\begin{aligned} \dot{u}_{iI}^* (F_{iI}^{int} - F_{iI}^{ext} + \rho_I \ddot{u}_{iI}) \\ + \dot{\omega}_{iI}^* (\bar{M}_{iI}^{int} - \bar{M}_{iI}^{ext} + \dot{\bar{L}}_{iI}) = 0 \end{aligned} \quad (2.29)$$

Since the virtual velocities are arbitrary, the terms within the parentheses must vanish. The terms within the first parenthesis immediately yield the translational equations of motion

$$\rho_I \ddot{u}_{iI} = F_{iI}^{ext} - F_{iI}^{int} \quad (\text{no sum on } I) \quad (2.30)$$

We note from Eq. (2.7) that

$$\dot{\bar{L}}_{jJ} = \bar{I}_{jkJ} \bar{\alpha}_{kJ} + e_{ijl} \bar{I}_{ikJ} \bar{\omega}_{kJ} \bar{\omega}_{lJ} \quad (\text{no sum on } J) \quad (2.31a)$$

where e_{ijl} is the alternative tensor. By noting that the quantity in the second parenthesis must vanish because of the arbitrariness of ω_{iI}^* , we obtain

$$\bar{I}_{jkJ} \bar{\alpha}_{kJ} + e_{ijl} \bar{I}_{ikJ} \bar{\omega}_{kJ} \bar{\omega}_{lJ} = \bar{M}_{jJ}^{\text{ext}} - \bar{M}_{jJ}^{\text{int}} \quad (2.31b)$$

(no sum on J)

Since the \bar{x}_i coordinates are principal coordinates of \bar{I}_{jk} , we can write these equations as follows

$$\bar{I}_{xxI} \bar{\alpha}_{xI} + (\bar{I}_{zzI} - \bar{I}_{yyI}) \bar{\omega}_{yI} \bar{\omega}_{zI} = \bar{M}_{xI}^{\text{ext}} - \bar{M}_{xI}^{\text{int}}$$

$$\bar{I}_{yyI} \bar{\alpha}_{yI} + (\bar{I}_{xxI} - \bar{I}_{zzI}) \bar{\omega}_{xI} \bar{\omega}_{zI} = \bar{M}_{yI}^{\text{ext}} - \bar{M}_{yI}^{\text{int}}$$

$$\bar{I}_{zzI} \bar{\alpha}_{zI} + (\bar{I}_{yyI} - \bar{I}_{xxI}) \bar{\omega}_{xI} \bar{\omega}_{yI} = \bar{M}_{zI}^{\text{ext}} - \bar{M}_{zI}^{\text{int}} \quad (2.32)$$

(no sum on I)

These are the rotational equations of motion, and they correspond to the Euler equations.

3. Deformable Elements

The deformable elements are treated by a rigid-convected (or corotational) formulation previously described by Belytschko and Hsieh (1972). In this technique, the displacements of each element are decomposed into rigid body displacements r_i and deformation displacements d_i

$$u_i = r_i + d_i \quad (2.33)$$

The strains are then given by

$$\hat{\epsilon}_{ij} = \frac{1}{2} \left(\frac{\partial \hat{d}_i}{\partial \hat{x}_j} + \frac{\partial \hat{d}_j}{\partial \hat{x}_i} \right) \quad (2.34)$$

Belytschko and Hsieh have shown that the matrix $\hat{\epsilon}_{ij}$ corresponds to the difference between the stretch tensor and the unit tensor. Hence, this strain corresponds closely to the common definition of engineering strain.

For purposes of developing element relations, Eq. (2.33) is expressed in matrix form

$$\{\hat{\epsilon}\} = [E] \{\hat{d}\} \quad (2.35)$$

where $\{\hat{d}\}$ is the matrix of nodal deformation displacements. It is also necessary to find a matrix $[T]$ such that

$$\{\hat{d}\} = [T] \{\hat{u}\} \quad (2.36)$$

It then follows that the nodal element forces $\{f^{(e)}\}$ are given by

$$\{f^{(e)}\} = [T]^T \{f^d\} \quad (2.37)$$

$$\{f^d\} = \int_V [E]^T \{\hat{\sigma}\} dV \quad (2.38)$$

where V is the volume of the element, $\{\hat{\sigma}\}$ the stresses measured in the corotational coordinates, and $\{f^d\}$ the nodal forces conjugate to $\{\dot{d}\}$, so that

$$\dot{W}^{int} = \{\dot{d}\}^T \{f^d\} \quad (2.39)$$

where W^{int} is the internal work. Note that both $\{\hat{\epsilon}\}$ and $\{\hat{\sigma}\}$ are measured in corotational coordinates, so their rates or increments are frame invariant and may be used directly in incremental constitutive equations without any corrections for rotations.

Spring Element. Consider a spring element with nodes I and J. The deformation of the spring is completely defined by its change in length

$$\delta_{IJ} = l - l^0 \quad (2.40)$$

where l and l^0 are the current and original lengths of the element. Since direct use of this formula will result in large round-off errors, an alternative formula was used which is derived as follows. If the displacement and position of the nodes are considered to be vectors,

then

$$\{x\}_J - \{x\}_I = \{x\}_J^{\circ} - \{x\}_I^{\circ} + \{u\}_J - \{u\}_I \quad (2.41)$$

Taking the scalar product of each side of this equation with itself, it follows that

$$l^2 = l^{\circ 2} + 2\{x\}_{JI}^T \{u\}_{JI} + \{u\}_{JI}^T \{u\}_{JI} \quad (2.42)$$

where

$$\{x\}_{JI} = \{x\}_J - \{x\}_I \quad \text{etc.}$$

after rearranging and factoring, it follows that

$$l - l^{\circ} = \frac{1}{l + l^{\circ}} [2\{x\}_{JI}^T \{u\}_{JI} + \{u\}_{JI}^T \{u\}_{JI}] \quad (2.43)$$

or in component form

$$\begin{aligned} \delta_{IJ} = l - l^{\circ} = \frac{1}{l + l^{\circ}} [2(x_{JI}u_{xJI} + y_{JI}u_{yJI} + z_{JI}u_{zJI}) \\ + u_{xJI}^2 + u_{yJI}^2 + u_{zJI}^2] \end{aligned} \quad (2.44)$$

The element strain is then given by

$$\hat{\epsilon} = \frac{\delta_{IJ}}{l^{\circ}} \quad (2.45)$$

The nodal force conjugate to δ_{IJ} is the tension $T = \hat{f}_{xJ}$, hence by

Eq. (2.38)

$$\hat{f}_{XJ} = \int_V \frac{1}{l} \hat{\sigma} dv \quad (2.45)$$

$$= A \hat{\sigma} \quad (2.46)$$

where A is the area of the cross-section.

The stress $\hat{\sigma}$ may be an arbitrary function of $\hat{\epsilon}$. In this program, the stress-strain law is

$$\hat{\sigma} = k_1 \hat{\epsilon} + k_2 \hat{\epsilon}^3 + 2\beta \sqrt{(k_1 + 3k_2 \epsilon^2) \rho} \dot{\epsilon} \quad (2.47)$$

where k_1 , k_2 and β are constants input by the user; k_1 is the linear spring constant. The last term is a linear viscosity with β the fraction of critical damping for the vibration of this element.

Beam Element. Consider a generic beam element with nodes I and J as shown in Fig. 11. The \hat{x} axis always moves with the beam element so that it joins the two nodes, while the \hat{y} axis is considered to rotate with the beam in the sense that its rotation is an average of the rotation of the two nodes about the \hat{x} axis. The deformation of the beam is then defined by its displacements relative to the rigid-convected coordinates $(\hat{x}, \hat{y}, \hat{z})$ of the element. The deformation displacements are given by

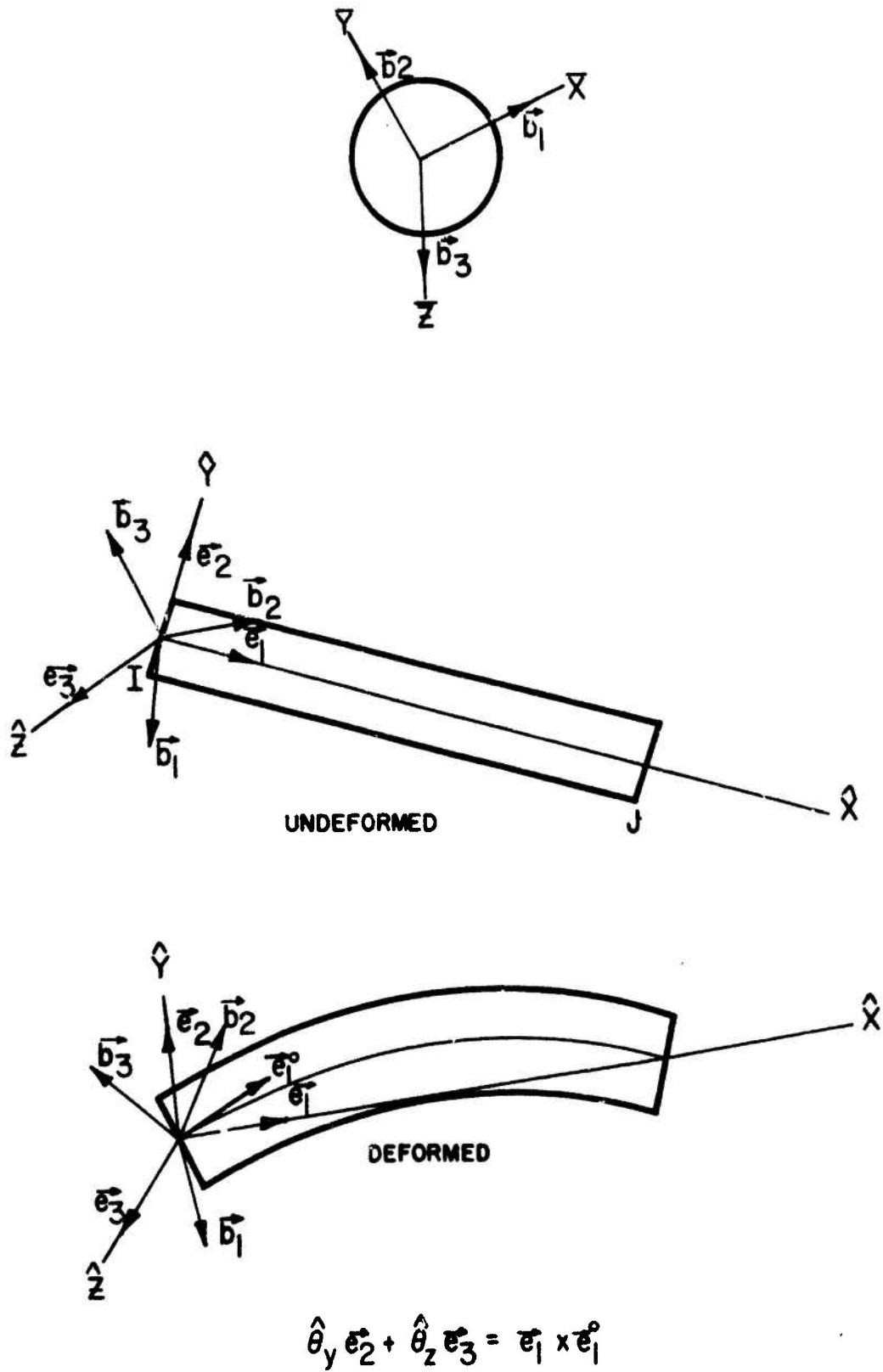


Figure 11. Beam element nomenclature.

$$\{d\}^T = \{\delta_{IJ}, \hat{\theta}_{xJI}, \hat{\theta}_{yI}, \hat{\theta}_{zI}, \hat{\theta}_{yJ}, \hat{\theta}_{zJ}\} \quad (2.48)$$

where δ_{IJ} = elongation, computed by Eq. (2.44)

$$\begin{aligned} \hat{\theta}_{xIJ} &= \text{torsional deformation} \\ \hat{\theta}_{yI}, \hat{\theta}_{yJ}, \hat{\theta}_{zI}, \hat{\theta}_{zJ} &= \text{bending deformation rotations} \end{aligned}$$

Because of the way the motion of the \hat{x} -axis is defined, the rigid body motion r_i need not be computed explicitly for the decomposition needed in Eqs. (2.33) and (2.34): the quantities defined above define the deformation of the element directly regardless of the extent of rigid body rotation.

For the purpose of computing the relative rotations, $\hat{\theta}_{yI}, \hat{\theta}_{zI}, \hat{\theta}_{yJ}, \hat{\theta}_{zJ}$, and $\hat{\theta}_{xJI}$, the body components of the unit vectors \vec{e}_1° and \vec{e}_2° (superscript noughts denote the vectors in the undeformed configuration) must be stored for each of the two nodes of the element. From a knowledge of the body components of \vec{e}_1° and \vec{e}_2° , the rotations are found as follows. Since the vector \vec{e}_1° rotates with the node, it indicates the direction of the axis of the element if there was no deformation; the angle between \vec{e}_1° and \vec{e}_1 indicates the magnitude of the deformation, this is illustrated in Fig. 11. Thus

$$\hat{\theta}_y \vec{e}_2 + \hat{\theta}_z \vec{e}_3 = \vec{e}_1 \times \vec{e}_1^\circ \quad (2.49)$$

For the purpose of this computation, we transform the components of \vec{e}_1° from body to element coordinates using Eqs. (2.3) and (2.4) so that

$$\begin{Bmatrix} \hat{e}_{1x}^\circ \\ \hat{e}_{1y}^\circ \\ \hat{e}_{1z}^\circ \end{Bmatrix} = [\mu]^T [\lambda] \begin{Bmatrix} \bar{e}_{1x}^\circ \\ \bar{e}_{1y}^\circ \\ \bar{e}_{1z}^\circ \end{Bmatrix} \quad (2.50)$$

Then substituting into Eq. (2.49), we find

$$\hat{\theta}_y \vec{e}_2 + \hat{\theta}_z \vec{e}_3 = \det \begin{bmatrix} \vec{e}_1 & \vec{e}_2 & \vec{e}_3 \\ 1 & 0 & 0 \\ \hat{e}_{1x}^\circ & \hat{e}_{1y}^\circ & \hat{e}_{1z}^\circ \end{bmatrix} = -\hat{e}_{1z}^\circ \vec{e}_2 + \hat{e}_{1y}^\circ \vec{e}_3 \quad (2.51)$$

Thus

$$\hat{\theta}_y = -\hat{e}_{1z}^\circ \quad \hat{\theta}_z = \hat{e}_{1y}^\circ \quad (2.52)$$

The deformation torsional rotation is found by taking the cross-product of \vec{e}_{2I}° and \vec{e}_{2J}° and projecting this vector on the current axis of the beam. This yields

$$\begin{aligned} \hat{\theta}_{xIJ} &= \vec{e}_1 \cdot (\vec{e}_{2I}^\circ \times \vec{e}_{2J}^\circ) = \vec{e}_1 \cdot \det \begin{bmatrix} \vec{e}_1 & \vec{e}_2 & \vec{e}_3 \\ \hat{e}_{x2I}^\circ & \hat{e}_{y2I}^\circ & \hat{e}_{z2I}^\circ \\ \hat{e}_{x2J}^\circ & \hat{e}_{y2J}^\circ & \hat{e}_{z2J}^\circ \end{bmatrix} \\ &= \hat{e}_{y2I}^\circ \hat{e}_{z2J}^\circ - \hat{e}_{y2J}^\circ \hat{e}_{z2I}^\circ \end{aligned} \quad (2.53)$$

Eqs. (2.52) and (2.53) require the assumption that the deformation displacements of an element be small. This implies that the relative rotations are sufficiently small so that the decomposition of the rotation vector into $\hat{\theta}_y$ and $\hat{\theta}_z$ implicit in Eq. (2.49) be valid. However, the overall rotation of the beam element may be arbitrarily large.

The deformation displacement field for the beam element is considered to consist of transverse displacements that are cubic

functions of \hat{x} , while the axial displacement is a linear function of \hat{x} . This can be written

$$\hat{d}_x^m = (1-\xi) \hat{d}_{xI} + \xi d_{xJ} \quad (2.54a)$$

$$\hat{d}_y^m = (\xi - 2\xi^2 + \xi^3) \ell \hat{\theta}_{zI} + (-\xi^2 + \xi^3) \ell \hat{\theta}_{zJ} \quad (2.54b)$$

$$\hat{d}_z^m = (-\xi + 2\xi^2 - \xi^3) \ell \hat{\theta}_{yI} + (\xi^2 - \xi^3) \ell \hat{\theta}_{yJ} \quad (2.54c)$$

$$\hat{\theta}_x = \xi \hat{\theta}_{xJI} \quad (2.54d)$$

where

$$\xi = \frac{\hat{x}}{\ell} \quad (2.54e)$$

and \hat{x} is taken to originate at node J; the superscript m is used to indicate that these are the displacements of the mid surface. If we impose the usual Euler-Bernoulli beam assumptions that normals to the midline remain straight and normal, we obtain

$$\hat{d}_x = \hat{d}_x^m - \hat{y} \frac{\partial \hat{d}_y^m}{\partial \hat{x}} - \hat{z} \frac{\partial \hat{d}_z^m}{\partial \hat{x}} + H(\hat{y}, \hat{z}) \frac{\partial \hat{\theta}_x}{\partial \hat{x}} \quad (2.55a)$$

$$\hat{d}_y = \hat{d}_y^m - \hat{z} \hat{\theta}_x \quad (2.55b)$$

$$\hat{d}_z = \hat{d}_z^m + \hat{y} \hat{\theta}_x \quad (2.55c)$$

where $H(\hat{y}, \hat{z})$ is the warping function.

The strain displacement equations, Eq. (2.34), can now be written

$$\hat{\epsilon}_x = \frac{\partial \hat{d}_x}{\partial \hat{x}} \quad (2.56a)$$

$$\hat{\epsilon}_{xy} = \frac{1}{2} \left(\frac{\partial \hat{d}_x}{\partial \hat{y}} + \frac{\partial \hat{d}_y}{\partial \hat{x}} \right) \quad (2.56b)$$

$$\hat{\epsilon}_{xz} = \frac{1}{2} \left(\frac{\partial \hat{d}_x}{\partial \hat{z}} + \frac{\partial \hat{d}_z}{\partial \hat{x}} \right) \quad (2.56c)$$

These equations are valid as long as $(\partial \hat{d}_y / \partial \hat{x})^2$ and $(\partial \hat{d}_z / \partial \hat{x})^2$ are small compared to $(\partial \hat{d}_x / \partial \hat{x})^2$. Although this condition is similar in appearance to that of moderate rotation theories, it is far less restrictive, because \hat{d}_y and \hat{d}_z are the displacements relative to the corotational coordinate \hat{x} . By reducing the size of the element, \hat{d}_y and \hat{d}_z can be made as small as needed, albeit at a rapidly increasing cost.

For the beam

$$\{\hat{\epsilon}\}^T = (\hat{\epsilon}_x, 2\hat{\epsilon}_{xy}, 2\hat{\epsilon}_{xz}) \quad (2.57)$$

and

$$[E] = \frac{1}{l} \begin{bmatrix} 1 & 0 & \hat{z}(6\xi-4) & \hat{y}(4-6\xi) & \hat{z}(6\xi-2) & \hat{y}(2-6\xi) \\ 0 & (\partial H / \partial \hat{y}) - \hat{z} & 0 & 0 & 0 & 0 \\ 0 & (\partial H / \partial \hat{z}) - \hat{y} & 0 & 0 & 0 & 0 \end{bmatrix} \quad (2.58)$$

So, having defined the strain-displacement relations, the stress $\{\hat{\sigma}\}^T = \{\hat{\sigma}_x, \hat{\sigma}_{xy}, \hat{\sigma}_{xz}\}$ can be computed for any constitutive law, and then the deformation nodal forces by Eq. (2.38).

Referring to Eqs. (2.39) and (2.40), it may be noted that $\{f^d\}$ for the beam is given by

$$\{f^d\}^T = (\hat{f}_{xJ}, \hat{m}_{xJ}, \hat{m}_{yI}, \hat{m}_{zI}, \hat{m}_{yJ}, \hat{m}_{zJ}) \quad (2.59)$$

The complete nodal force matrix could be computed from Eq. (2.37) after [T], as defined by Eq. (2.36), is found. However, it is simpler to first find $\{\hat{f}\}$ by equilibrium and then transform to the global components by a simple vector transformation; the two procedures are equivalent. Equilibrium yields

$$\begin{aligned} \hat{f}_{xI} &= -\hat{f}_{xJ} & \hat{m}_{xI} &= -\hat{m}_{xJ} \\ \hat{f}_{zJ} &= \frac{\hat{m}_{yI} + \hat{m}_{yJ}}{l} & \hat{f}_{zI} &= -\hat{f}_{zJ} \\ \hat{f}_{yJ} &= \frac{\hat{m}_{zI} + \hat{m}_{zJ}}{l} & \hat{f}_{yI} &= -\hat{f}_{yJ} \end{aligned} \quad (2.60)$$

The global components can then be found by Eq. (2.1) and (2.2).

As indicated in Chapter I, the program has two methods for treating the moment stiffness of the beam. For linear beams or beams with simple nonlinear characteristics where the overall bending moments can be determined as functions of the deformation rotations, the bending moments may be determined directly by Eqs. (1.4).

The second method for obtaining the nodal moments is by integrating the stresses appropriately through Eqs. (2.38), with [E] defined by Eq. (2.58). This integration is done only to obtain the axial force and moment. The numerical integration for torsion is included neither in this description nor in the program. If torsion were included, both the state of stress and strain would be biaxial, which increases computations immensely. Since Euler-Bernoulli theory

does not include the shear stresses that arise from bending, only the shear strains due to torsion are available. Thus the additional computations would not appear to be justified.

The integral for the nodal forces, Eq. (2.38), is evaluated numerically. Many investigators have used Gaussian quadrature formulas for this integration. However, these formulas involve far more computations than trapezoidal integrations, with little advantage in accuracy. The only drawback of a strict trapezoidal integration is that the elastic bending stiffness of the element is not recovered. A modified trapezoidal integration originally described in Marchertas and Belytschko (1974) is used here. The beam is subdivided into strips as shown in Fig. 3. In each strip, as for example the strip indicated by cross-hatching in Fig. 3, the axial stress $\hat{\sigma}$ is assumed to vary bilinearly in η and ξ , so

$$\begin{aligned} \sigma(\eta, \xi) = & \sigma_{iI}(1-\xi)(1-\eta) + \sigma_{jI}\eta(1-\xi) \\ & + \sigma_{iJ}(1-\eta)\xi + \sigma_{jJ}\eta\xi \end{aligned} \quad (2.61)$$

Substituting this form into Eq. (2.37) and integrating over η and ξ , we find the expressions for \hat{f}_{xJ}^{ℓ} and \hat{m}_{yJ}^{ℓ} to be

$$\hat{f}_{xJ}^{\ell} = \frac{1}{4} \text{th} [\sigma_{iI} + \sigma_{jI} + \sigma_{iJ} + \sigma_{jJ}] \quad (2.62)$$

$$\hat{m}_{yJ}^{\ell} = \frac{1}{6} \text{th} [2\sigma_{iJ}\hat{z}_i + 2\sigma_{jJ}\hat{z}_j + \sigma_{iJ}\hat{z}_j + \sigma_{jJ}\hat{z}_i] \quad (2.63)$$

The formulas for \hat{m}_{yI}^{ℓ} , \hat{m}_{zJ}^{ℓ} and \hat{m}_{zI}^{ℓ} are similar. The total nodal forces are then found by adding the contributions of all of the layers. The

major distinction from a trapezoidal integration is in Eq. (2.63), which is based on a form quadratic in \hat{z} . This modification preserves the exact elastic bending stiffness of the element. Moreover, the assumption of a linear stress variation in \hat{x} implies a linear moment field, which is consistent with equilibrium of the element. The approximation errors therefore lie entirely in the stress-strain law, which is necessarily satisfied only at the end points of the element for nonlinear materials.

Hydrodynamic Element. The hydrodynamic element is a pentahedron with six nodes at its corners, as shown in Fig. 4. The triangular surfaces of the pentahedrons are called the top and bottom surfaces, respectively, and each of these is defined by three nodes. All of the nodes on each of these surfaces must be associated with the same primary node, for the top and bottom surfaces are considered rigid. The generic element is numbered counterclockwise and viewed from top to bottom. The edges of the element are defined by the lines connecting nodes I - L, nodes J - M, and nodes K - N, respectively. The deformation of the hydrodynamic element is characterized by the dilatation, Δ , which is given by

$$\Delta = \frac{V - V^0}{V^0} \quad (2.64)$$

where V is the volume of the element, and a superscript nought denotes the original volume. For the purpose of computing the volume and change in volume, the pentahedron is subdivided into three tetrahedrons.

The volume of any tetrahedron with generic node numbers I, J, K and L is given by

$$\begin{aligned}
 V_{IJKL} &= \frac{1}{6} \det \begin{bmatrix} x_{JI} & x_{KJ} & x_{LK} \\ y_{JI} & y_{KJ} & y_{LK} \\ z_{JI} & z_{KJ} & z_{LK} \end{bmatrix} \\
 &= \frac{1}{6} [z_{JI}(x_{LK}y_{KJ} - x_{KJ}y_{LK}) + z_{KJ}(x_{JI}y_{LK} - x_{KL}y_{JI}) \\
 &\quad + z_{LK}(x_{KJ}y_{JI} - x_{JI}y_{KJ})] \\
 x_{IJ} &= x_I - x_J, \text{ etc.} \tag{2.65}
 \end{aligned}$$

The volume of the pentahedron is

$$V = V_{IJKL} + V_{JLMN} + V_{JKLN} \tag{2.66}$$

To define the matrix [E] of Eq. (2.35), we take the time derivative of the dilatation as defined in terms of the nodal coordinates in Eqs. (2.66). Noting that the time derivatives of the nodal coordinates are the velocities, we obtain [E], which is given in Table 1.

The pressure in the hydrodynamic element is assumed to be constant, so that the integral expression for the nodal forces given by Eq. (2.38) yields that the nodal forces are given by

$$\{f\} = -p [E]^T \tag{2.67}$$

Table 1. The [E] Matrix for Hydrodynamic Elements

$$\begin{aligned}
 & Y_{KJ}^z LK - Y_{LK}^z KJ \\
 & X_{LK}^z KJ - X_{KJ}^z LK \\
 & X_{KJ}^y LK - X_{LK}^y KJ \\
 & Y_{LK}^z NI - Y_{NI}^z LK + Y_{NM}^z LN - Y_{LN}^z NM \\
 & X_{NI}^z LK - X_{LK}^z NI + X_{LN}^z NM - X_{NM}^z LN \\
 & X_{LK}^y NI - X_{NI}^y LK + X_{NM}^y LN - X_{LN}^y NM \\
 & Y_{JI}^z LJ - Y_{LJ}^z JI + Y_{NJ}^z LN - Y_{LN}^z NJ \\
 & X_{LJ}^z JI - X_{JI}^z LJ + X_{LN}^z NJ - X_{NJ}^z LN \\
 & X_{JI}^y LJ - X_{LJ}^y JI + X_{NJ}^y LN - Y_{LN}^y NJ \\
 & Y_{KJ}^z JI - Y_{JI}^z KJ + Y_{NM}^z MJ - Y_{MJ}^z NM + Y_{KN}^z NJ - Y_{NJ}^z KN \\
 & X_{JI}^z KJ - X_{KJ}^z JI + X_{MJ}^z NM - X_{NM}^z MJ + X_{NJ}^z KN - X_{KN}^z NJ \\
 & X_{KJ}^y JI - X_{JI}^y KN + X_{NM}^y MJ - X_{MJ}^y NM + X_{KN}^y NJ - X_{NJ}^y KN \\
 & Y_{LN}^z NJ - X_{NJ}^z LN \\
 & X_{NJ}^z LN - X_{LN}^z NJ \\
 & X_{LN}^y NJ - X_{NJ}^y LN \\
 & Y_{MJ}^z LM - Y_{LM}^z MJ + Y_{LK}^z KJ - Y_{KJ}^z LK \\
 & X_{LM}^z MJ - X_{MJ}^z LM + X_{KJ}^z LK - X_{LK}^z KJ \\
 & X_{MJ}^y LM - X_{LM}^y MJ + X_{LK}^y KJ - X_{KJ}^y LK
 \end{aligned}$$

[E]^T = $\frac{1}{6}$

The pressure is computed by

$$p = B\Delta + \alpha B\dot{\Delta} \quad (2.68)$$

where α is a linear viscosity coefficient and B is a bulk modulus. For the nodes that are secondary, the nodal forces are then transformed by Eq. (2.28).

Elastic Planes. The ejection seat geometries are represented by an assemblage of piecewise linear surfaces, which may be either elastic or rigid. This assemblage of planes may translate in an arbitrary direction in space as an arbitrary function of time, which is prescribed in the input. When any of the rigid bodies contacts one of the planes, its equations of motion are modified so as to reflect its interaction with the plane.

Each of the piecewise linear surfaces is defined by three points \vec{x}_I^o , $I = 1$ to 3, in the original configuration. The coordinates of these points are given in the global system. The three points must be oriented so that the normal vector as obtained by the right hand rule points in the direction of the skeletal model. In order to establish the required equations, the normal to the surface is first computed by the formula

$$\vec{n} = \frac{\vec{x}_{21}^o \times \vec{x}_{31}^o}{|\vec{x}_{21}^o| |\vec{x}_{31}^o|} \quad (2.69)$$

The minimum distance between any node, \vec{x}_p , and the surface is given by

$$D^{\circ} = \vec{p}^{\circ} \cdot \vec{n}$$

(2.70)

$$\vec{p}^{\circ} = \vec{x}_p^{\circ} - \vec{x}_1^{\circ}$$

where \vec{p}° is a vector from any point in the surface to \vec{x}_p° . As the surface translates, (rotations of the surface are not included), the unit normal remains unchanged, while the positions of \vec{x}_1° and \vec{x}_p° become

$$\vec{x}_1^{\circ} = \vec{x}_1^{\circ} + \vec{u}_1$$

(2.71)

$$\vec{x}_p^{\circ} = \vec{x}_p^{\circ} + \vec{u}_p$$

where \vec{u}_p is the prescribed displacement of the ejection seat. The distance of point P from the surface can then be computed by

$$D = \vec{p} \cdot \vec{n}$$

(2.72)

When the distance of the node from the surface is negative or zero, the node is assumed to be in contact with the surface. It is then necessary to check its acceleration normal to the plane. If the acceleration is into the plane, the node will remain in contact with the plane, whereas when the acceleration is away from the plane, there is no contact and no modifications of the equations of the node are needed.

If the node is in contact with the plane, a force normal to the plane is applied to the node which is proportional to the

magnitude of the penetration of the point, i.e.

$$f_n = k D \quad (2.73)$$

where f_n is the force component normal to the surface. In addition, if friction is present, tangential forces proportional to f_n may be applied in the form

$$f_t = \mu f_n \quad (2.74)$$

CHAPTER III

MATHEMATICAL ASPECTS OF SOLUTION PROCEDURES

1. Explicit Time Integration

One of the methods for solving the equations of motion of this model is the explicit method. This method is by far the most efficient per time step, but the time step must be quite small if the model has a high frequency content, that is, low masses connected by stiff springs. The stability limits are discussed subsequently in this Section.

The explicit integration employs the Newmark β -formulas (Newmark (1959)) with $\beta=0$, which are almost identical to the central difference formulas (see Belytschko (1974)). These formulas predict the velocities and displacements at a time step in terms of the accelerations at the previous step. For the translational components, these formulas may be used directly, so

$$\dot{u}_{iI}^{j+1} = \dot{u}_{iI}^j + \frac{1}{2} \Delta t (\ddot{u}_{iI}^j + \ddot{u}_{iI}^{j+1}) \quad (3.1)$$

$$u_{iI}^{j+1} = u_{iI}^j + \Delta t \dot{u}_{iI}^j + \frac{1}{2} \Delta t^2 \ddot{u}_{iI}^j \quad (3.2)$$

where the superscripts denote the time step and Δt the time increment during a step.

For the rotational degrees of freedom, Eqs. (3.2) cannot be used directly because the orientations are described by unit vectors \vec{b}_{iI} and its rates are not equivalent to the angular velocities and

accelerations. The counterpart of Eq. (3.2) is

$$\vec{b}_i^{j+1} = \vec{b}_i^j + \Delta t \frac{d\vec{b}_i^j}{dt} + \frac{1}{2} \Delta t^2 \frac{d^2\vec{b}_i^j}{dt^2} \quad (3.3)$$

From vector analysis

$$\frac{d\vec{b}_i}{dt} = \vec{\omega} \times \vec{b}_i \quad (3.4)$$

$$\frac{d^2\vec{b}_i}{dt^2} = \vec{\omega} \times (\vec{\omega} \times \vec{b}_i) + (\vec{\alpha} \times \vec{b}_i) \quad (3.5)$$

and substituting Eqs. (3.4) and (3.5) into Eq. (3.3) yields a formula for the updated unit vectors

$$\begin{aligned} \vec{b}_i^{j+1} = \vec{b}_i^j + \Delta t (\vec{\omega} \times \vec{b}_i^j) \\ + \frac{1}{2} \Delta t^2 [\vec{\omega} \times (\vec{\omega} \times \vec{b}_i^j) + (\vec{\alpha} \times \vec{b}_i^j)] \end{aligned} \quad (3.6)$$

To obtain a formula for the updated components of the unit vectors, we temporarily fix the \bar{x}_i coordinates and consider a particular unit vector \vec{b}_i in Eq. (3.6); we then dot Eq. (3.6) with the unit vector corresponding to the component of \vec{b}_i to be updated. For example, the updated \bar{x} -component of \vec{b}_3 is found by letting $i=3$ in Eq. (3.6) and taking the scalar product of both sides of the equation with \vec{b}_1 , which yields, after some simplification

$$\bar{b}_{3x}^{j+1} = \bar{b}_1^j \cdot \bar{b}_3^{j+1} = \Delta t \bar{\omega}_y^j + \frac{1}{2} \Delta t^2 (\bar{\omega}_x^j \bar{\omega}_z^j + \bar{\alpha}_y^j) \quad (3.7a)$$

Similarly

$$\bar{b}_{3y}^{j+1} = \bar{b}_2^j \cdot \bar{b}_3^{j+1} = -\Delta t \bar{\omega}_x^j + \frac{1}{2} \Delta t^2 (\bar{\omega}_y^j \bar{\omega}_z^j - \bar{\alpha}_x^j) \quad (3.7b)$$

$$\bar{b}_{1y}^{j+1} = \bar{b}_1^j \cdot \bar{b}_2^{j+1} = \Delta t \bar{\omega}_z^j + \frac{1}{2} \Delta t^2 (\bar{\omega}_x^j \bar{\omega}_y^j + \bar{\alpha}_z^j) \quad (3.7c)$$

Normality and orthogonality are used to find the remaining components of \bar{b}_3^{j+1} and \bar{b}_1^{j+1} , and it is assumed that the rotations during a time step are small so that second order terms can be neglected. From the normality of \bar{b}_3 , it follows that

$$\bar{b}_{3z}^{j+1} = \left[1 - (\bar{b}_{3x}^{j+1})^2 - (\bar{b}_{3y}^{j+1})^2 \right]^{\frac{1}{2}} \quad (3.8)$$

while, if it is first assumed that $\bar{b}_{1x}^{j+1} \sim 1$, orthogonality yields

$$\bar{b}_{1z}^{j+1} = -(\bar{b}_{3x}^{j+1} + \bar{b}_{1y}^{j+1} \bar{b}_{3y}^{j+1}) / \bar{b}_{3z}^{j+1} \quad (3.9)$$

The component \bar{b}_{1x}^{j+1} can then be found by normality

$$\bar{b}_{1x}^{j+1} = \left[1 - (\bar{b}_{1y}^{j+1})^2 - (\bar{b}_{1z}^{j+1})^2 \right]^{\frac{1}{2}} \quad (3.10)$$

The components of the \bar{b}_1 and \bar{b}_3 vectors given above are in terms of the \bar{x}_i coordinates of that node at time step j . Using Eq. (2.3) with the $[\lambda]$ matrix defined in the previous time step, the components

are transformed to global coordinates; the vector \vec{b}_2^{j+1} is then found by a vector product.

The flowchart for this numerical procedure is shown in Table 2. Besides the approximations of small rotations implicit in Eqs. (3.9) and (3.10), the major source of truncation error lies in the evaluation of the angular accelerations from the equations of angular motion, (2.32). These equations involve quadratic combinations of the angular velocities at the same time step as angular accelerations, so that the new angular velocities must be approximated. This source of error can be mitigated by an iterative procedure, i.e. finding the angular accelerations from an approximation to Eq. (2.32), integrating these accelerations to find the new angular velocities, and then repeating the computation of the angular accelerations. This procedure was tried, but it was found to have insignificant effects on the solution.

Another consequence of the existence of the quadratic combination of velocities in Eq. (2.32) is that the classical Fourier theories of numerical stability are not applicable even for linear material problems. Therefore, it has been necessary to pick time steps with the standard formula in terms of the maximum eigenvalue λ of the system

$$\Delta t^2 \leq \frac{4}{\lambda}$$

only serving as a guideline. To insure post facto that the computations are stable, energy balance checks were made as follows.

Table 2

Flow Chart of Explicit Integration Procedure

1. Set initial conditions, $t=0$
2. Compute $\{u(t+\Delta t)\}$ by Eq. (3.2)
3. Update unit vectors \vec{b}_I by Eqs. (3.7) to (3.10) and transform to global components by Eq. (2.3)
4. Find deformation displacements $\{d\}$ by Eqs. (2.44), (2.49) and (2.53)
5. Find the strain in the convected coordinates, $\{\hat{\epsilon}\}$ by Eq. (2.34)
6. Stress-strain law
7. Find local nodal forces $\{f^d\}$ by Eq. (2.38)
8. Add $\{f^d\}$ into $\{F^{int}\}$
9. Compute $\{\ddot{u}(t+\Delta t)\}$ by Eqs. (2.30) and (2.31)
10. Compute $\{\dot{u}(t+\Delta t)\}$ by Eq. (3.1)
11. $t = t + \Delta t$; go to 2

The kinetic energy at each time step j is defined by

$$T^j = \frac{1}{2} \rho_i \dot{u}_{iI}^j + \frac{1}{2} \bar{\omega}_{iI}^j \bar{I}_{iI} \bar{\omega}_{iI}^j$$

where I is summed over the primary nodes in the system. The external work is defined by a trapezoidal integration in time, so

$$W^{\text{ext},0} = 0$$

$$W^{\text{ext},j} = W^{\text{ext},j-1} + \frac{1}{2} (u_{iI}^j - u_{iI}^{j-1}) (F_{iI}^{\text{ext},j} + F_{iI}^{\text{ext},j-1})$$

The internal work is similarly defined by

$$W^{\text{int},0} = 0$$

$$W^{\text{int},j} = W^{\text{int},j-1} + \frac{1}{2} (\hat{u}_{iA}^{(e),j} - \hat{u}_{iA}^{(e),j-1}) (\hat{f}_{iA}^{(e),j} + \hat{f}_{iA}^{(e),j-1})$$

Energy balance then requires that

$$W^{\text{int},j} + T^j - W^{\text{ext},j} < \epsilon (W^{\text{int},j} + T^j)$$

If ϵ is greater than about 0.05, a solution is considered unacceptable. The source of the energy error may be an arrested or incipient numerical instability, or excessive truncation error.

2. Implicit Time Integration

The second method for integrating the equations of motion in time is the implicit method. This method permits the use of rather large time steps, particularly if the high frequency aspects of the response are unimportant. However, the method involves the solution of nonlinear equations in each time step. The nonlinear equations are solved by a Newton-Raphson procedure, so that a sequence of solutions to linear algebraic equations are used to obtain the solution to the nonlinear equations. The linear equations are solved by a Cholesky decomposition technique; hence the solution time is bandwidth dependent. Therefore the method becomes quite uneconomical for the complex models, where the bandwidth is usually quite large, for in spite of the possibility of taking large time steps, the computational effort required per time step is so great as to preclude its use. More specific figures for solution times are given subsequently.

The implicit integration employs the trapezoidal integratic: formulas, which correspond to the Newmark β -formulas with $\beta=1/4$ (Newmark (1959)). These formulas are

$$\dot{u}_{iI}^{j+1} = \dot{u}_{iI}^j + \frac{1}{2} \Delta t (\ddot{u}_{iI}^j + \ddot{u}_{iI}^{j+1}) \quad (3.16)$$

$$u_{iI}^{j+1} = u_{iI}^j + \Delta t \dot{u}_{iI}^j + \frac{1}{4} \Delta t^2 (\ddot{u}_{iI}^j + \ddot{u}_{iI}^{j+1}) \quad (3.17)$$

From the above, it immediately follows that

$$\ddot{u}_{iI}^{j+1} = \frac{4}{\Delta t^2} (\Delta u_{iI}) - \ddot{u}_{iI}^j - \frac{4}{\Delta t} \dot{u}_{iI}^j \quad (3.19)$$

$$\dot{u}_{iI}^{j+1} = \frac{2}{\Delta t} \Delta u_{iI} - \dot{u}_{iI}^j \quad (3.20)$$

where

$$\Delta u_{iI} = u_{iI}^{j+1} - u_{iI}^j \quad (3.21)$$

The above equations must hold both for increments in rotations and translations, provided that the increments in rotations are small, so

$$\dot{\omega}_{iI}^{j+1} = \frac{2}{\Delta t} \Delta \bar{\theta}_{iI} - \dot{\omega}_{iI}^j \quad (3.22)$$

The increment $\Delta \bar{\theta}$ has no precise meaning, for it is neither referred to the \vec{b}_I^j or the \vec{b}_I^{j+1} coordinate systems, but to some intermediate coordinates. However $\Delta \bar{\theta}$ is not a basic variable, for orientations are ultimately described by the body coordinate system \vec{b}_I so this ambiguity is not important.

The equations for implicit integration are best developed in matrix form, so we define the nodal matrices $\{D\}$, $\{\dot{D}\}_I$ and $\{F\}_I$.

$$\{D\}_I = \begin{matrix} u_{xI} \\ u_{yI} \\ u_{zI} \\ \bar{\theta}_{xI} \\ \bar{\theta}_{yI} \\ \bar{\theta}_{zI} \end{matrix} \quad \{\dot{D}\}_I = \begin{matrix} \dot{u}_{xI} \\ \dot{u}_{yI} \\ \dot{u}_{zI} \\ \dot{\omega}_{xI} \\ \dot{\omega}_{yI} \\ \dot{\omega}_{zI} \end{matrix} \quad \{F\}_I = \begin{matrix} F_{xI} \\ F_{yI} \\ F_{zI} \\ \bar{M}_{xI} \\ \bar{M}_{yI} \\ \bar{M}_{zI} \end{matrix} \quad (3.23)$$

The complete matrix of nodal displacements is $\{D\}$, which consists of $\{D\}_I$, with I from the number of nodes stacked vertically in order in the column matrix.

The implicit solution procedure requires a linearized estimate of the internal forces at the end of the time step in terms of the incremental forces. This is provided by the tangential stiffness matrix $[k]$ which gives

$$\{F^{j+1, \text{int}}\} = \{F^j, \text{int}\} + [K]\{\Delta D\} \quad (3.24)$$

The tangential stiffness here contains the damping terms; details are given in Appendix 2.

The basis of the implicit method is to solve the equations of motion at time step $j+1$ directly in terms of the displacements. For this purpose, the equations of motion are expressed at $j+1$ in terms of the solution at the previous step. The right hand sides of the equations of motion, Eqs. (2.30) and (2.31) are expressed in terms of increments of displacements by means of Eqs. (3.24), which gives

$$\begin{aligned} \rho_I (\Delta u_{iI} - \Delta t \dot{u}_{iI}^j - \frac{\Delta t^2}{4} \ddot{u}_{iI}^j) \\ = \frac{\Delta t^2}{4} (F_{iI}^{j+1, \text{ext}} - F_{iI}^{j+1, \text{int}}) \end{aligned} \quad (3.25)$$

$$\begin{aligned} \bar{I}_{rsI} (\Delta \bar{\theta}_{sI} - \Delta t \bar{\omega}_{sI}^j - \frac{\Delta t^2}{4} \bar{\alpha}_{sI}^j) \\ + e_{rts} \bar{I}_{su} (\frac{\Delta t^2}{4} \bar{\omega}_u^j \bar{\omega}_t^j + \Delta t \bar{\omega}_t^j \Delta \bar{\theta}_u + \Delta t \bar{\omega}_u^j \Delta \bar{\theta}_t + \Delta \bar{\theta}_u \Delta \bar{\theta}_t) \\ = \frac{\Delta t^2}{4} (\bar{M}_{rI}^{j+1, \text{ext}} - \bar{M}_{rI}^{j+1, \text{int}}) \end{aligned} \quad (3.26)$$

We now (1) use Eq. (3.24) to estimate the internal forces at $j+1$,
 (2) neglect the quadratic terms $\Delta\bar{\theta}_u \Delta\bar{\theta}_t$ and (3) neglect any anti-symmetric terms arising from the rate of change of angular momentum.
 Eq. (3.25) and (3.26) can then be written

$$\begin{aligned}
 & ([M1] + \frac{\Delta t}{4} [M2] + \frac{\Delta t^2}{4} [K]) \{\Delta D\} \\
 &= \Delta t [M1] \{\dot{D}^j\} + \frac{\Delta t^2}{4} ([M1] \{D^j\} \\
 &\quad + \{F^{j+1, ext}\} - \{F^j, int\} - \{R^j\}) \quad (3.27)
 \end{aligned}$$

where

$$[M1]_{II} = \begin{bmatrix} \rho & 0 & 0 & 0 & 0 & 0 \\ 0 & \rho & 0 & 0 & 0 & 0 \\ 0 & 0 & \rho & 0 & 0 & 0 \\ 0 & 0 & 0 & \bar{I}_{xx} & 0 & 0 \\ 0 & 0 & 0 & 0 & \bar{I}_{yy} & 0 \\ 0 & 0 & 0 & 0 & 0 & \bar{I}_{zz} \end{bmatrix}_I \quad (3.28)$$

$$[M2]_{II} = \begin{bmatrix} \begin{bmatrix} 0 \\ -3 \times 3 \end{bmatrix} & & \begin{bmatrix} 0 \\ -3 \times 3 \end{bmatrix} \\ \begin{bmatrix} 0 \\ -3 \times 3 \end{bmatrix} & \begin{bmatrix} 0 & (\bar{I}_{xx} - \bar{I}_{yy}) \bar{\omega}_z & (\bar{I}_{xx} - \bar{I}_{zz}) \bar{\omega}_y \\ 0 & & (\bar{I}_{zz} - \bar{I}_{yy}) \bar{\omega}_x \\ \text{sym} & & 0 \end{bmatrix} \end{bmatrix}_I \quad (3.29)$$

$$R_{iI}^j = e_{ist} \bar{I}_{su} \bar{\omega}_u^j \bar{\omega}_t^j \quad (3.30)$$

Eqs. (3.27) are solved in each time step. The error is then computed by

$$F_{iI}^{err} = F_{iI}^{j+1,ext} - F_{iI}^{j+1,int} - \rho \ddot{u}_{iI}^{j+1} \quad (3.31)$$

$$\bar{M}_{iI}^{err} = \bar{M}_{iI}^{j+1,ext} - \bar{M}_{iI}^{j+1,int} - \dot{L}_{iI}^{j+1} \quad (3.32)$$

The error must satisfy the criterion

$$\{\Delta D\}^T \{F^{err}\} < \epsilon (W^{j,int} + T^j) \quad (3.33)$$

where ϵ is a tolerance, and $W^{j,int}$ and T^j are the internal and kinetic energies, as defined by Eqs. (3.12) and (3.14). This criterion requires that the energy transfer to the system arising from error be bounded. If Eq. (3.33) is not met, Eqs. (3.27) are resolved with $\{F^{err}\}$ added to $\{F^{ext}\}$. This does not require much extra time, for the coefficient matrix is triangulated, at most, only once per time step.

Belytschko and Schoeberle (1975) have shown that this procedure leads to a stable algorithm regardless of the size of the time step as long as Eq. (3.33) is met. The cited proof was only for nonlinear materials, but so far no unstable computations have been reported, when Eq. (3.33) was satisfied for a reasonable tolerance.

The unit vectors are updated as follows. The vector counterpart of Eqs. (3.16) and (3.17) are

$$\vec{b}_I^{j+1} = \vec{b}_I^j + \Delta t \dot{\vec{b}}_I^j + \frac{\Delta t^2}{4} (\ddot{\vec{b}}_I^j + \ddot{\vec{b}}_I^{j+1}) \quad (3.34)$$

$$\dot{\vec{b}}_I^{j+1} = \dot{\vec{b}}_I^j + \frac{\Delta t}{2} (\ddot{\vec{b}}_I^j + \ddot{\vec{b}}_I^{j+1}) \quad (3.35)$$

Multiplying Eq. (3.34) by $-\frac{2}{\Delta t}$ and adding to Eq. (3.35), we obtain

$$-\frac{2}{\Delta t} \vec{b}_I^{j+1} + \dot{\vec{b}}_I^{j+1} = -\frac{2}{\Delta t} \vec{b}_I^j - \dot{\vec{b}}_I^j \quad (3.36)$$

and rearranging and using Eq. (3.4) yields

$$\vec{b}_I^{j+1} - \frac{\Delta t}{2} (\vec{\omega}^{j+1} \times \vec{b}_I^{j+1}) = \vec{b}_I^j + \frac{\Delta t}{2} (\vec{\omega}^j \times \vec{b}_I^j) \quad (3.37)$$

To obtain a formula for the updated components of the unit vectors, we temporarily fix the \bar{x}_I coordinates and consider a particular unit vector \vec{b}_I^j in Eq. (3.37). We then take the scalar product of Eq. (3.37) with the unit vector corresponding to the component of \vec{b}_I to be updated. For example, the updated \bar{x} -component of \vec{b}_3 is found by letting $I=3$ in Eq. (3.37) and taking the scalar product of both sides of the equation with \vec{b}_1^j , which yields, after simplification

$$b_{3x}^{j+1} = \vec{b}_1^j \cdot \vec{b}_3^{j+1} = \frac{\Delta t}{2} \vec{b}_1^j \cdot (\vec{\omega}^{j+1} \times \vec{b}_3^{j+1}) + \frac{\Delta t}{2} \vec{\omega}_y^j \quad (3.38)$$

Similarly, the \bar{y} -components of \vec{b}_3 is given by

$$b_{3y}^{j+1} = \vec{b}_2^j \cdot \vec{b}_3^{j+1} = \frac{\Delta t}{2} \vec{b}_2^j \cdot (\vec{\omega}^{j+1} \times \vec{b}_3^{j+1}) - \frac{\Delta t}{2} \vec{\omega}_x^j \quad (3.39)$$

The evaluation of triple scalar products in Eqs. (3.38) and (3.39) yields

$$\vec{b}_1^{j+1} \cdot (\vec{\omega}^{j+1} \times \vec{b}_3^{j+1}) = \bar{\omega}_y^{j+1} b_{3z}^{j+1} - \bar{\omega}_z^{j+1} b_{3y}^{j+1} \quad (3.40)$$

Hence Eqs. (3.38) and (3.39) can be written as

$$b_{3x}^{j+1} = \frac{\Delta t}{2} (\bar{\omega}_y^{j+1} b_{3z}^{j+1} - \bar{\omega}_z^{j+1} b_{3y}^{j+1}) + \frac{\Delta t}{2} \bar{\omega}_y^j \quad (2.41)$$

$$b_{3y}^{j+1} = \frac{\Delta t}{2} (\bar{\omega}_z^{j+1} b_{3x}^{j+1} - \bar{\omega}_x^{j+1} b_{3z}^{j+1}) - \frac{\Delta t}{2} \bar{\omega}_x^j \quad (3.42)$$

Now if it is assumed that $b_{3z}^{i+1} \sim 1$, Eqs. (3.41) and (3.42) can be solved simultaneously to yield

$$b_{3x}^{j+1} = \frac{\Delta t}{2} \left[\frac{\Delta t}{2} \bar{\omega}_z^{j+1} (\bar{\omega}_x^j + \bar{\omega}_x^{j+1}) + (\bar{\omega}_y^j + \bar{\omega}_y^{j+1}) \right] / \left(1 + \frac{\Delta t^2}{4} \bar{\omega}_z^{j+1} \bar{\omega}_z^{j+1} \right) \quad (3.43)$$

$$b_{3y}^{j+1} = \frac{\Delta t}{2} \left[\frac{\Delta t}{2} \bar{\omega}_z^{j+1} (\bar{\omega}_y^j + \bar{\omega}_y^{j+1}) - (\bar{\omega}_x^j + \bar{\omega}_x^{j+1}) \right] / \left(1 + \frac{\Delta t^2}{4} \bar{\omega}_z^{j+1} \bar{\omega}_z^{j+1} \right) \quad (3.44)$$

In a similar manner the \bar{y} -component of \vec{b}_1^{j+1} is found to be

$$b_{1y}^{j+1} = \frac{\Delta t}{2} \left[\frac{\Delta t}{2} \bar{\omega}_x^{j+1} (\bar{\omega}_y^j + \bar{\omega}_y^{j+1}) + (\bar{\omega}_z^j + \bar{\omega}_z^{j+1}) \right] / \left(1 + \frac{\Delta t^2}{4} \bar{\omega}_x^{j+1} \bar{\omega}_x^{j+1} \right) \quad (3.45)$$

Equations (3.37), when substituted into the above, yield

$$b_{3x}^{j+1} = \left(\frac{\Delta t}{2} \omega_z^{-j+1} \Delta \bar{\theta}_x + \Delta \bar{\theta}_y \right) / \left(1 + \frac{\Delta t^2}{4} \omega_z^{-j+1} \omega_z^{-j+1} \right) \quad (3.46)$$

$$b_{3y}^{j+1} = \left(\frac{\Delta t}{2} \omega_z^{j+1} \Delta \bar{\theta}_y - \Delta \bar{\theta}_x \right) / \left(1 + \frac{\Delta t^2}{4} \omega_z^{-j+1} \omega_z^{-j+1} \right) \quad (3.47)$$

$$b_{1y}^{j+1} = \left(\frac{\Delta t}{2} \omega_x^{j+1} \Delta \bar{\theta}_y + \Delta \bar{\theta}_z \right) / \left(1 + \frac{\Delta t^2}{4} \omega_x^{-j+1} \omega_x^{-j+1} \right) \quad (3.48)$$

The remaining components are then updated as described in the previous section.

The major computational effort in this procedure is in triangulating Eq. (3.27). If the number of degrees of freedom is N and the semibandwidth is B , triangulation requires NB^2 multiplications. The semibandwidth is given by

$$B = \max(I-J) \quad (3.49)$$

where I and J are the node numbers of any primary nodes connected by a deformable element, either directly or through secondary nodes. It is thus of advantage to number nodes so that B is minimized.

The equations are triangulized at most once in each time step. The iterative procedure is performed using the triangularized matrix with direct backsubstitution. This only requires $2NB$ multiplications. If the system is only mildly nonlinear, the equations are solved with the triangular decomposition obtained from a previous time step. The computational procedure is shown in Table 3.

Table 3

Flow Chart of Iterative, Implicit Integration Procedure

1. Set initial conditions: $t=0$; $\{\ddot{u}(0)\}$ must be computed if initial conditions are nonzero
2. Compute coefficient of $\{\Delta D\}$ and R.H.S. of Eq. (3.27) with $\{R\} = 0$
3. Solve Eq. (3.27) for tentative increment in displacement
4. Compute tentative displacement, acceleration and velocity by Eqs. (3.21), (3.19) and (3.20), respectively
5. Update unit vectors \vec{b}_I by Eqs. (3.46) to (3.48) and transform to global components by Eq. (2.3)
6. Find tentative strain by Eq. (2.34)
7. Stress-strain law
8. Find tentative nodal forces by Eq. (2.38) and add into internal force array
9. Compute error force by Eqs. (3.31) and (3.32)
10. If energy error criteria, Eq. (3.33) is not met, set $\{F^{ext}\} = \{F^{ext}\} + \{F^{err}\}$ and go to 3
11. Solution for step complete; update dependent variables
12. $t = t + \Delta t$; go to 2

3. Modal Analysis

The modes of the system are obtained by a linear eigenvalue technique. The use of this technique thus requires that the material properties be linearized in the domain of interest, so that

$$\{F^{int}\} = [K]\{D\} \quad (3.50)$$

The use of a linear eigenvalue analysis also requires that the product terms $\bar{\omega}_x \bar{\omega}_z$, $\bar{\omega}_y \bar{\omega}_z$ in Eqs. (2.32) be neglected: thus the modal analysis requires that the motion be restricted to two dimensions or that the rigid bodies have equal moments of inertia about all axes. In this study, the first assumption was usually made. In addition, for purposes of simplicity, the effect of damping on the modal behavior was neglected. Provided that the damping is proportional to the stiffness, which is the case here, the effect of damping on the frequencies could then be ascertained after the completion of the analysis as described subsequently.

The modal equations are obtained in the usual manner (see Przemieniecki (1968)) by assuming harmonic response of the form

$$\{D(t)\} = \{X\}e^{i\omega t} \quad (3.51)$$

Substituting Eqs. (3.50) and (3.51) into (2.30) and (2.32) and invoking the above assumptions, yields

$$([K] - \omega^2 [M1])\{X\} = 0 \quad (3.52)$$

which is linear eigenvalue problems, with the eigenvalues ω^2 corresponding to the natural frequencies, and the eigenvectors $\{X\}$ corresponding to the natural modes of vibration.

The eigenvalue problem of Eq. (3.52) is put into standard eigenvalue form as follows. Since the products of angular velocities appearing in the rotational equations of motion are not treated, $[M1]$ is diagonal and a matrix $[M1]^{-1/2}$ can be constructed by taking the reciprocal of the square root of each diagonal term of the matrix. Defining

$$\{\bar{X}\} = [M1]^{1/2}\{X\} \quad (3.53)$$

we obtain from (3.52) and (3.53) that

$$([M]^{-1/2}[K][M]^{1/2} - \omega^2 [1])\{\bar{X}\} = 0 \quad (3.54)$$

The eigenvalues and eigenvectors are found by either of two methods:

- i. a Jacobian iteration procedure as implemented in subroutine EIGEN in the IBM Scientific Subroutine Package (1967);
- ii. a power method iteration procedure.

The first method is relatively time consuming and cannot take advantage of the bandedness of the stiffness matrix. Hence it can be used only for relatively small models. However, it provides all frequencies and modes of the system.

The second method can take advantage of bandedness and hence is applicable to larger models. However, in the present version only the lowest mode can be found. The determination of subsequent modes

would entail the implementation of shift and sweeping procedures into the algorithm; see Gourlay and Watson (1973) or Belytschko (1974).

If the system is damped by a stiffness proportional damping of magnitude α as used herein, then the frequencies of the damped system may be determined directly from the undamped modes. Standard harmonic analysis then shows (see for example, Hurty and Rubinstein (1974)), that the frequency of the damped vibration is given by

$$\omega_{\text{damp}} = \omega \sqrt{1 - \frac{\alpha^2 \omega^2}{4}} \quad (3.55)$$

CHAPTER IV
MATERIAL PROPERTIES AND GEOMETRY

This chapter describes the geometrical and material property data used in the models and the sources and basis for this data. For purposes of convenience, the description of this data is subdivided into sections dealing with the spine, the head and pelvis, and the rib cage. The inertial properties are described in a separate Section. Finally, the combinations of these data used in models of various complexity are summarized by describing Models I, II, and III.

1. Thoracolumbar and Cervical Spine

Each vertebra of the thoracolumbar spine is modelled as a rigid body. The geometry of each vertebra is described by the locations of the secondary nodes, which serve to connect the various deformable elements to the vertebra. An inertial segment usually does not coincide with a vertebral body. Instead, each vertebra is embedded in an inertial segment, and the primary node of the segment is its centroid. Therefore, it is worthwhile in describing the geometry of the vertebrae to define a base point which is independent of the location of the primary node of the inertial segment. This base point is chosen to be the center of the lower end plate of the vertebral body. The geometry of each vertebra is then characterized by the positions in the vertebra's body coordinates of twelve additional points: (1) the spinous process tip; (2) left and right transverse process tips; (3) the left and right/inferior-superior articular facet points; and (4) the left and right/inferior-superior ligamenta flava

points. A set of coordinates for vertebra L3 is given in Table 4. This data was obtained from a skeletal model by measurement and was then scaled to conform to the measurement of the measured averages of Lanier (1939) by Schultz and Galante (1970).

The second aspect of the geometry is the positioning and orientation of the vertebrae in space. In all of these studies, it was assumed that there is no curvature in the frontal plane, so only the curvature in the sagittal plane was included. The first sets of data were generated by taking the previous model of Schultz, et al. (1974), which was for a standing position, and reducing the curvature so as to correspond more closely with a seated position. Subsequently, several radiographs of seated pilots were obtained and digitized so that the configuration could be determined. The base point coordinates in the y-z plane for the ad hoc configuration and one of the radiograph configurations is given in Table 5. The overall length of the thoracolumbar columns for this data corresponds closely to that of an average male. Clauser (1968) reported that in a sample of 13 male cadavers, the mean distance from omphalian to cervicale is 43.5 cm and cited an earlier unpublished Air Force study in which the same figure was reported. The nearest corresponding dimension in this model, the distance from L4 to T1, is 43.3 cm., which is in good agreement.

The vertebral body heights and the disc heights along the central axis are based on the data of Lanier and Todd and Pyle (1928), in the thoracolumbar spine. In the cervical spine, the dimensions are based on data provided by AMRL and the orientations were measured from radiographs.

Table 4 Typical Vertebral Geometry
for Lumbar and Thoracic Vertebrae

L3 Vertebral Body Point	\bar{x} -coordinate (cm)	\bar{y} -coordinate (cm)	\bar{z} -coordinate (cm)
ICE	0.	0.	0.
SCE	0.	0.4	2.78
SP	0.	6.51	0.93
LTP	4.63	3.45	1.59
RTP	-4.63	3.45	1.59
LIAF	2.38	3.85	-0.53
RIAF	-2.38	3.85	-0.53
LSAF	2.00	4.12	2.52
RSAF	-2.00	4.12	2.52
LILF	0.25	5.13	0.93
RILF	-0.25	5.13	0.93
LSLF	2.50	3.85	1.59
RSLF	-2.50	3.85	1.59

Table 4 (continued)

T6 Vertebral Body Point	\bar{x} -coordinate (cm)	\bar{y} -coordinate (cm)	\bar{z} -coordinate (cm)
ICE	0.	0.	0.
SCE	0.	-0.2	1.98
SP	0.	4.98	-0.41
LTP	3.35	3.74	1.83
RTP	-3.35	3.74	1.83
LIAF	1.49	2.44	0.51
RIAF	-1.49	2.44	0.51
LSAF	1.36	1.73	2.54
RSAF	-1.36	1.73	2.54
LILF	0.25	3.96	0.41
RILF	-0.25	3.96	0.41
LSLF	3.35	3.05	1.83
RSLF	-3.35	3.05	1.83

Table 5 Geometry of Spine

Vertebral Level	Coordinates of Inferior End Plate Center		Vertebral Body Height (cm)	Intervertebral Disc Height* (cm)
	y (cm)	z (cm)		
L5	1.800	2.020	2.392	1.859
L4	1.100	5.700	2.636	1.354
L3	1.000	9.550	2.751	1.223
L2	1.331	13.450	2.792	1.173
L1	2.142	17.150	2.726	0.996
T12	3.003	20.590	2.567	0.822
T11	3.882	23.680	2.433	0.645
T10	4.594	26.500	2.298	0.477
T9	4.849	29.240	2.146	0.460
T8	4.638	31.830	2.073	0.459
T7	4.580	34.300	2.019	0.404
T6	4.250	36.610	1.990	0.314
T5	3.990	38.850	1.957	0.266
T4	3.690	41.000	1.902	0.214
T3	3.350	43.150	1.850	0.274
T2	2.920	45.260	1.790	0.306
T1	2.410	47.440	1.648	0.448
C7	1.909	49.420	1.612	0.394
C6	1.760	51.448	1.516	0.434
C5	1.460	53.516	1.515	0.576
C4	1.290	55.439	1.513	0.417
C3	1.484	57.332	1.511	0.398
C2	1.636	59.239	1.500	0.408

* Indicates disc below vertebral level.

The secondary nodes of the vertebrae are interconnected by deformable elements which represent the connective tissues, ligaments and the intervertebral disc. The center line of each intervertebral disc element connects the centers of the endplates of adjacent vertebra. Each intervertebral disc has stiffness in bending due to both flexion-extension and lateral bending, in torsion, and in the axial mode.

The stiffnesses are based primarily on the experimental work of Markolf (1970), Brown, Hansen and Yorra (1957), Rolander (1966) and Kazarian (1972). These experimental measurements were augmented by model studies of the intervertebral disc under axial load performed by Kulak (1974). A large part of the procedure of assigning these stiffnesses has been summarized in Schultz, Belytschko, et al (1973). That paper also lists 12 other sources of intervertebral disc data which have been considered in developing the data used in the model.

In spite of the wealth of literature available on this topic, the experimental data is inadequate for assigning stiffnesses at each vertebral level. However, geometrical dimensions at every level have been provided by Lanier (1939). In order to estimate stiffnesses at each level, it was assumed that stiffnesses vary in relation to the geometry. This is equivalent to assuming that intrinsic material properties do not vary significantly with vertebral level. Thus, by using the experimental values at the levels at which they are available and by using the geometrical ratios for other levels, stiffnesses were assigned to every level of the spine.

The procedure by which this was done follows. First, each disc was idealized as an elliptical ring of linear, elastic material

corresponding to the annulus fibrosis. The outside ellipse is defined by major and minor diameters a_o and b_o , respectively, and the inner ellipse by major and minor axes a_i and b_i , respectively. These two ellipses were assumed to be concentric. Lanier's mean values of the transverse and sagittal diameters of each vertebral body were assigned to a_o and b_o , respectively, and to the height h . The interior diameters were assumed to be 0.75 of the outer diameters, based on Farfan et al. (1970). It was assumed that this elliptical ring, representing the annulus fibrosis and longitudinal ligaments, provides the major resistance to bending, torsion and shear. This assumption is realistic in view of the hydrostatic behavior of the nucleus pulposus reported by Nachemson (1960), for a hydrostatic material does not contribute to shear or torsional resistance, and contributes to bending resistance only if it is located asymmetrically with respect to the neutral bending plane. The axial stiffness was assumed to be proportional to the total cross-sectional area of the disc.

It follows then from strength of materials that the stiffnesses vary from level to level in proportion to the following geometric factors: for tension, compression, and shear

$$r_A = \frac{1}{h} (a_o b_o - a_i b_i) \quad (4.1)$$

for bending about the minor diameter

$$r_m = \frac{1}{h} (a_o^3 b_o - a_i^3 b_i) \quad (4.2)$$

for bending about the major diameter

$$r_m = \frac{1}{h} (a_o b_o^3 - a_i b_i^3) \quad (4.3)$$

for torsion

$$r_t = \frac{1}{h} \left(\frac{a_o^3 b_o^3}{a_o^2 + b_o^2} - \frac{a_i^3 b_i^3}{a_i^2 + b_i^2} \right) \quad (4.4)$$

Extensive data is available on the stiffnesses at the L3/L4 and T8/T9 levels from cadaver material measurements. There is also some data on the upper thoracic spine. From the data the disc stiffnesses at other levels were calculated by using the geometrical ratios listed above. Finally, measured stiffnesses at several other levels were used to check on the consistency of the data, which was found to be quite good.

Because the discs are very short, shear action is quite strong. To account for this, shear factors ϕ which appear in Eq. (1.4) were added to account for the shear behavior.

Another aspect which had to be considered in this study is the nonlinearity of the force deflection characteristic of the disc. Very little data is available from which the nonlinearity could be precisely established, except for perhaps the axial force-deflection behavior of the disc. The nonlinearity in the axial mode is distinctly different in the lumbar and throacic regions. As can be seen from Fig. 12, the axial behavior of the disc is quite nonlinear, particularly if one considers both the tensile and compressive regimes. However, if the preloaded state resulting from body weight is

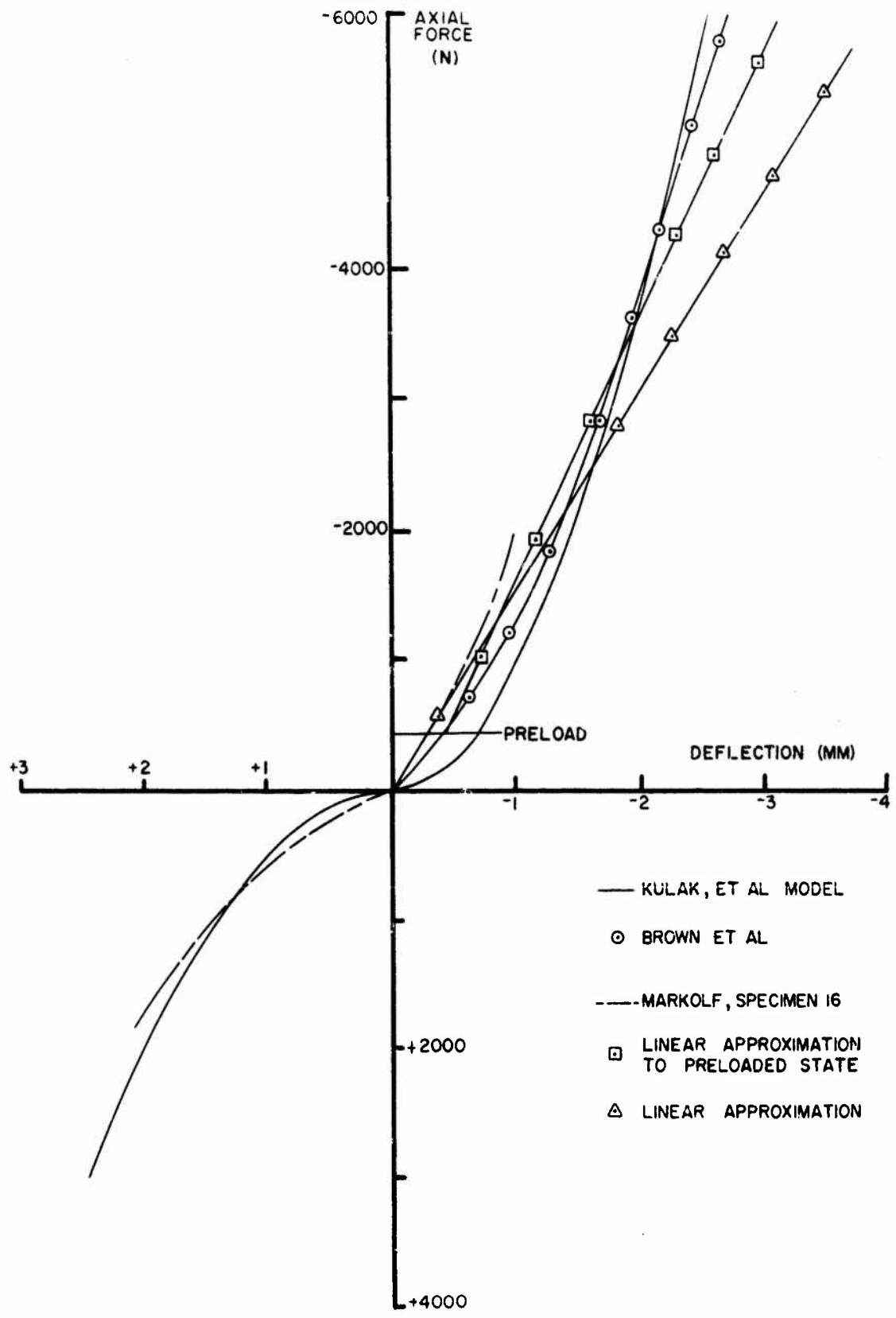


Figure 12. Response of L3 to axial load.

considered as a point of reference, then the behavior of the disc for compressive loads above that point is rather linear. In addition, it can be seen that a linear approximation to the behavior above that point requires a greater stiffness coefficient than from the unloaded state, by a factor of about 1.33. However, the data used in the model does not include this factor. Although the model could handle a cubic force deflection curve which would approximate the behavior shown in Fig. 12 quite closely, it was not used because of the difficulties of introducing the preloaded state into the cubic curve.

The axial force deflection characteristics in a thoracic spine are illustrated in Fig. 13. It can be seen that both experimental measurements and computer model results based on the nonlinear stress-strain curve as reported by Kulak, et al. exhibit very linear behavior. Therefore in the thoracic and cervical regions, a linear curve is adequate and no further modifications are contemplated. It may be mentioned that the increased linearity of the axial behavior of the thoracic and cervical discs is related to the reduced relative height of these discs, where the relative height is defined as the ratio of height to average diameter. This relative height is considerably smaller in the thoracic and cervical regions. For discs with small relative height, the application of axial load does not result primarily in hoop stress in the annulus, but a combination of compressive and tensile stresses, so that the nonlinearities of the material tends to cancel. The damping coefficients were based on the work of Payne (1971) and Kazarian (1972). A summary of all material properties for the discs is given in Table 6.

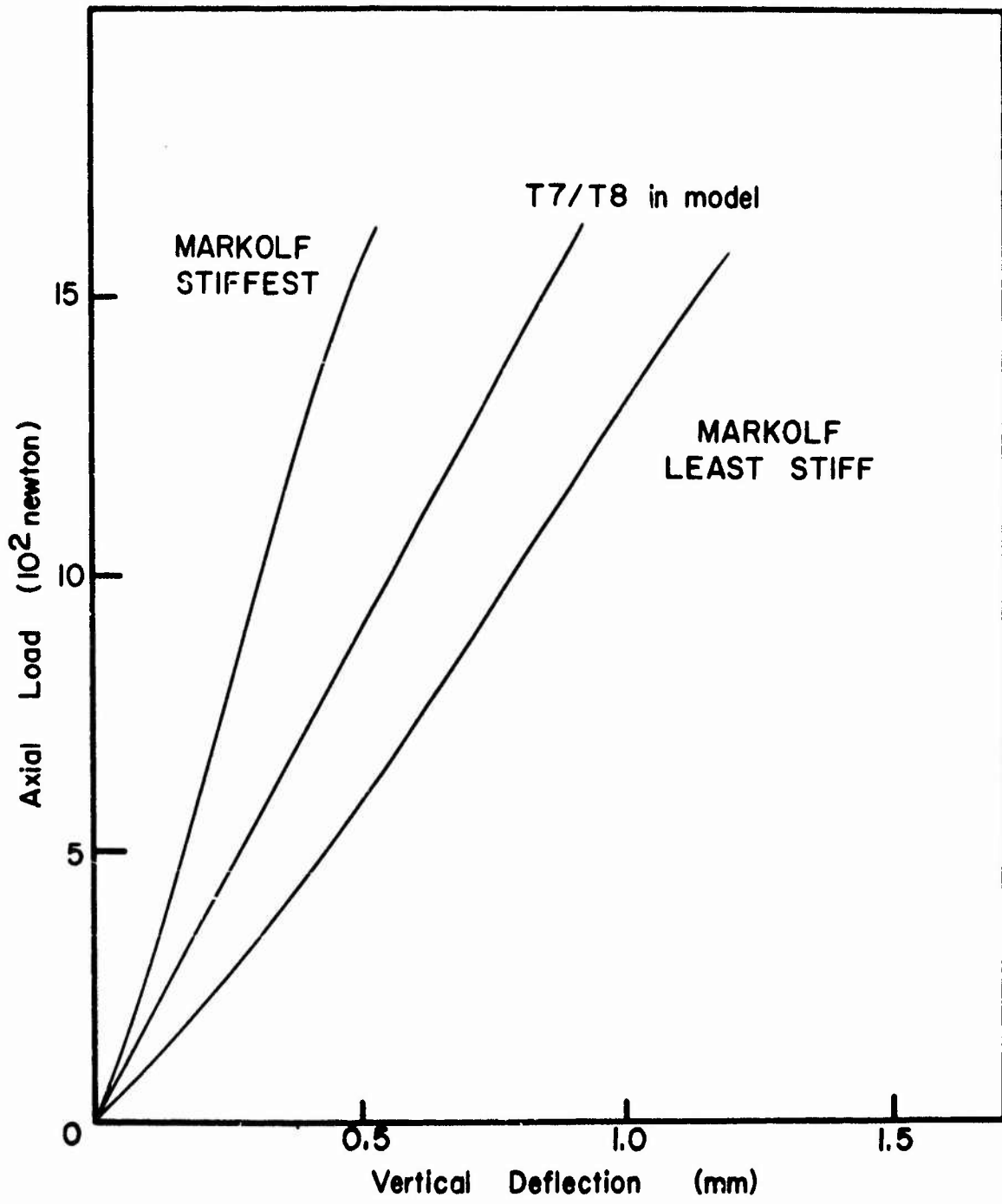


Figure 13. Response of T1 to axial load

Table 6 Stiffness Properties of Intervertebral Discs

Disc Level	Axial Stiffness Dyne/cm x 10 ⁹	Torsional Stiffness Dyne-cm x 10 ⁹	Bending Stiffness Dyne-cm x 10 ⁹ Sagittal Plane	Bending Stiffness Dyne-cm x 10 ⁹ Frontal Plane	Shear Deformation Parameter ϕ
S-L5	1.10	0.90	0.70	1.57	7
L5-L4	1.40	1.10	0.80	1.81	9
L4-L3	1.50	1.20	0.90	2.19	9
L3-L2	1.50	1.20	0.90	2.16	13
L2-L1	1.60	1.20	0.90	2.20	14
L1-T12	1.80	1.00	0.90	2.27	16
T12-T11	1.50	0.80	1.00	2.34	30
T11-T10	1.50	0.70	1.20	2.44	41
T10-T9	1.50	0.70	1.10	1.93	72
T9-T8	1.50	0.60	1.10	1.76	78
T8-T7	1.50	0.60	1.00	1.59	66
T7-T6	1.80	0.60	1.00	1.62	82
T6-T5	1.90	0.60	1.00	1.68	177
T5-T4	2.10	0.60	1.00	1.81	158
T4-T3	1.50	0.40	0.60	1.22	128
T3-T2	1.20	0.30	0.40	1.04	48
T2-T1	0.70	0.20	0.20	0.63	34
T1-C7	1.10	0.18	0.20	0.62	45

Table 6 (Continued)

Disc Level	Axial Stiffness Dyne/cm x 10 ⁹	Torsional Stiffness Dyne-cm x 10 ⁹	Bending Stiffness Dyne-cm x 10 ⁹ Sagittal Plane	Frontal Plane	Shear Deformation Parameter ϕ
C7-C6	2.84	0.11	0.11	0.25	45
C6-C5	1.01	0.07	0.06	0.10	45
C5-C4	0.60	0.04	0.04	0.06	45
C4-C3	0.67	0.05	0.04	0.05	45
C3-C2	0.70	0.05	0.04	0.05	45
C2-C1	0.60	0.04	0.04	0.10	45

All ligament and facet axial stiffness 1.5×10^7 dyne/cm.

All disc elements were axially damped using a 0.2% stiffness proportional viscous damping.

The ligaments are represented by spring elements which connect the secondary nodes representing the spinous process tips (inter and intra spinous ligaments), spring elements connecting the transverse process tips (inter-transverse ligaments) and springs connecting points on the vertebral body, which represent mainly the ligamenta flava. All of these elements are nonlinear in that they have no resistance in compression, i.e., when they are slack. In the thoracolumbar spine, the articular facets are also represented by spring elements. The locations of the secondary nodes to which these spring elements are connected were adjusted so that the line of action of the facet forces corresponds to the normal to the facet planes. Typical lines of action for articular facets in the lumbar and thoracic spine are given in Table 7.

The model of the cervical spine is similar to that of the thoracolumbar spine, except that no ligaments were included at this time and that each articular facet plane was represented by three points, so that the hydrodynamic element could be used to model the facet joint. The intervertebral disc heights in the cervical spine were obtained from data provided by AMRL. The data included both an anterior and posterior disc height, so these were averaged for use in the model. The vertebral geometry was obtained from direct measurement of a cadaver spine. These measurements included vertebral body height, endplate areas, spinous process location and three points on each superior articular facet plane. Both right and left superior articular facet planes were measured and these were then averaged to obtain a symmetric configuration. The inferior articular facet planes were obtained by placing the cervical vertebrae in a standard configuration

Table 7. Lines of Action of Articular Facets

Vertebral Level	x-component	y-component	z-component
L5-L4	-0.96	0.2	0.18
L4-L3	-0.87	0.48	0.
L3-L2	-0.85	0.42	0.31
L2-L1	-0.99	0.09	0.08
L1-T12	-0.71	0.54	0.43
T12-T11	-1.00	0.	0.
T11-T10	0.13	0.97	0.14
T10-T9	0.13	0.89	0.44
T9-T8	0.16	0.92	0.33
T8-T7	0.14	0.93	0.31
T7-T6	0.39	0.76	0.51
T6-T5	0.	0.99	0.13
T5-T4	0.	0.99	0.07
T4-T3	0.44	0.69	0.56
T3-T2	0.22	0.81	0.53
T2-T1	0.31	0.69	0.65

obtained from a radiograph and then defining the points of the inferior articular facet planes so that they are parallel and a prescribed distance from the superior facet planes; this distance was measured in a direction normal to the facet plane. The resulting configuration is illustrated in Fig. 14. The facet planes in these figures appear as triangles. The force deflection characteristics of the facet joint was then modelled with the hydrodynamic element described in Chapter II.

2. Rib Cage

The model of the rib cage consists of rib pairs 1 - 10 and the sternum. Each rib is modelled as a rigid body, with the deformability of the rib cage represented by deformable elements which represent the costo-transverse and costo-vertebral articulations. The location of the superior and inferior costo-vertebral CV articulations and the costo-transverse CT articulations were based on those reported in Schultz, Benson and Hirsch (1974). The diagram from Andriacchi, et al. (1974) indicates the nature of these data. The geometry of each rib is characterized by 8 points placed as follows: two coincident points in the costo-tubercle defining the position of the costo-transverse articulation, a pair of inferior and superior points placed at the rib head at the positions of the costo-vertebral articulations, two points placed along the inferior and superior borders of the rib shaft at the mid axillary line to provide points of attachment for deformable elements representing the elastic behavior of soft tissues occupying the intercostal spaces, and a pair of points at the interior end of the calcified portion of the rib providing points of attachment

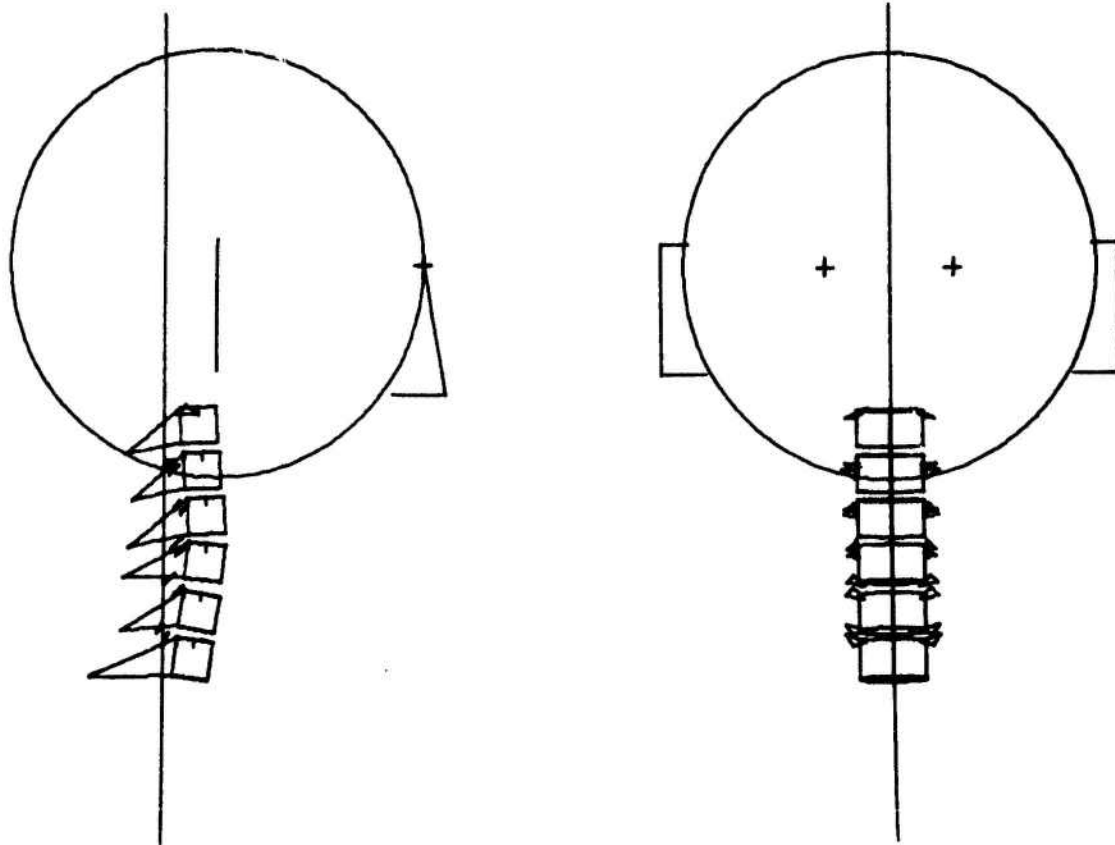


Figure 14. Cervical spine geometry.

for deformable elements which represent the costo-cartilages. Rib geometry data were obtained from measurements reported in Schultz, Benson and Hirsch, (1974a). Data describing the rib shaft geometry are reported in Table 9, taken from Andriacchi, et al. The rib cage geometry is illustrated in Figs. 8 and 9. The stiffness properties of the deformable elements used in the rib cage are summarized in Table 10.

3. Viscera and Abdominal Cavity

The abdominal cavity and viscera are represented by hydrodynamic elements stacked in series with rigid bodies between each layer as shown in Fig. 10. The compressibility of the model from an analytical viewpoint is thus entirely axial. In the actual viscera, the wave motion is mainly governed by the interaction of the walls of the torso and its contents. Thus, in response to a compressive load, the viscera would move vertically and laterally, with the latter component stretching the abdominal walls.

The mechanism of wave propagation through the viscera by an interaction of the membrane lining and the hydrodynamic contents has been studied by Torvik (1970). He derived relationships for both large deformations of the membrane and nonlinear membrane response. For small deflection, linear membrane response, he gives the standard water hammer formula for wave speed

$$c = \sqrt{\frac{Et}{2r\rho}} \quad (4.5)$$

where E is Young's modulus for the membrane wall, t the thickness of the wall, r its radius and ρ the density of the fluid, which in this

Table 8. Costo-vertebral geometry

Level	C1*	Inf. + Trans. Diam.	C2*	Spinal Diam. + Sup./Inf.	C3*	Vert. + Diam.	E2*	F1*	F2*	F3*
T1		3.16		1.69 1.75		1.62		.030	1.90	4.0
T2	3.03	3.22	2.05	1.79 1.95	1.95	1.77	1.22	.033	3.36	3.81
T3		3.09		2.0 2.18		1.84		.033	3.50	3.0
T4	3.09	3.04	2.47	2.23 2.37	2.07	1.88	1.92	.035	4.70	3.01
T5		3.09		2.42 2.56		1.90		.035	4.73	3.30
T6	3.22	3.20	2.88	2.61 2.73	2.23	1.90	2.45	.035	4.96	3.33
T7		3.34		2.74 2.86		1.89		0.0	4.90	3.30
T8	3.60	3.52	2.98	2.97 3.03	2.45	1.97	2.72	0.0	5.36	3.02
T9		3.74		3.04 3.08		2.06		0.0	5.30	2.80
T10	4.12	4.08	3.22	3.07 3.14	2.55	2.23	3.06	0.0	5.14	2.53

* Mean value of 5 specimen reported in Schultz, Benson and Hirsch (1974b)

+ Data reported by Lanier (1939) [All data in cm.]

EXPLANATION OF SYMBOLS

C1-Max. lateral diameter

C2-Midline AP diameter

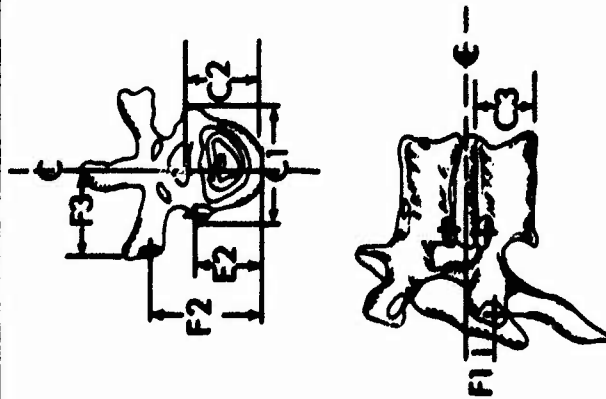
C3-Anterior vertebral body height

E2-Posterior distance from anterior edge of disc to costo-vertebral facet

F2-Posterior distance from anterior edge of disc to costo-transverse facet

F3-Lateral distance from centerline to costo-transverse facet

F1-Superior departure from centerline to costo-transverse facet



From Andriacchi, et al (1974)

Table 9. Rib geometry

Rib	Y _L cm	Y _A cm	X _C cm	Y _C cm	r _{CA} cm	∠AD degrees	Z _H (cm)	Z _L (cm)
1	7.0	-2.5	1.0	-1.5	11.4	31.0	0.0	0.0
2	1.0	-3.2	5.0	-1.9	11.0	50.0	0.0	0.0
3	5.4	-1.2	2.5	-5.7	9.0	83.0	0.0	0.0
4	6.6	-0.9	2.4	-5.7	11.0	88.0	0.0	0.0
5	3.3	-.65	6.5	-8.35	14.5	66.0	0.0	0.0
6	2.4	-2.8	10.5	-9.8	8.0	57.0	1.05	-1.0
7	3.2	-2.3	10.6	-10.3	18.0	61.0	.05	-1.95
8	3.9	-1.8	0.6	-10.7	18.0	70.0	.05	-2.9
9	1.4	-1.3	5.6	-9.3	13.0	90.0	.1	-2.5
10	19.8	-0.3	4.9	-9.1	11.0	105.0	.1	-2.9

From Andriacchi, et al (1974)

Table 10. Stiffness Properties of Deformable Elements in Rib Cage

Joint Name	Connecting Motion Segment	Motion Segment Level	Axial Stiffness dyne/cm x 10 ⁷	Torsional Stiffness dyne-cm x 10 ⁸	Bending Stiffness dyne-cm x 10 ⁷
Costo-Vertebral	Rib-vertebrae	T1-T10	5.0	0.35	7.5
Costo-Transverse Process	Rib-vertebrae	T1-T10	5.0		
Intercostal	Rib-rib	T6-T10	5.0	1.0	2.5
Interchondral Cartilages	Rib-rib	T1-T10	2.0		
Costo-Sternal	Rib-sternum	T1-T2	5.0	1.0	7.0
		T3-T5	5.0	1.0	2.5
		T6-T7	5.0	1.0	1.5

case are the viscera. This formula neglects the compressibility of the viscera. If we let E, the modulus of skin (although the passive resistance of muscles is also included) be 60×10^6 dynes/cm², and let $t=1$ cm, $r=10$ cm, we obtain $c = 1700$ cm/sec. This corresponds very well with the values measured by Weis and Mohr (1967), which are 1980 cm/sec.

The bulk modulus is then computed by the standard formula for acoustic wave speed.

$$B = \rho c^2 \quad (4.6)$$

This gives an effective value for B of 3.92×10^6 dynes/cm². This bulk modulus should not be interpreted as a bulk modulus of the viscera; it represents a constant that reflects the combined action of the membrane walls and the abdomen.

The visceral elements are connected through rigid bodies to ribs T10. This implies that all axial load in the abdominal cavity is transferred to the rib cage; no axial load transfer to the interior of the thoracic cavity is assumed. The bottom visceral elements are connected to the pelvis.

4. Head

The head is modelled as a rigid body. In the examples studied, any helmet or helmet mounted devices were assumed rigidly attached to the head, so the mass and mass moments of inertia of these were simply added to the head. However, it is possible to separate the inertias of the head and helmet and interconnect the two by springs

as shown in Fig. 15.

The mass of the head was chosen to be 4.6 kg, the mass moments of inertia about 400 kg-cm^2 based on the anthropometric dummy measurements of Bartz (1972). The helmet masses were based on the average of 3 helmets measured by the investigators. These had an average mass of 1.4 kg and mass moments of 100 kg-cm^2 .

5. Pelvis

The pelvis was represented as a rigid body with a mass and mass moments of inertia given in Table 11. The data is taken from Bartz (1972). The geometrical aspects of the pelvic representation are shown in Figs. 8 and 9.

6. Preliminary Evaluation of Injury Potential

In order to obtain a qualitative estimate of the injury potential of various combinations of sagittal plane moments and axial force for the vertebrae, a method of calculating the maximum stress in the vertebrae based on the combined axial force and moment predicted by the model was developed. This is only a simplified model, but it is indicative of the effects of moments on stress levels in the vertebral bodies. Since injury is probably related to stress levels, this method gives a means for evaluating the effects of the moments. We idealize the vertebral body as a cylindrical shell of radius r_0 and height h . The shell is considered to be cortical bone with a Young's modulus of $1.5 \times 10^{11} \text{ dynes/cm}^2$. The interior of the shell (vertebral

Table 11. Inertial Properties
for Isolated Ligamentous Spine

Motion Segment	Mass ρI Grams $\times 10^3$	\bar{I}_{xxI} Gram-cm ² $\times 10^4$	\bar{I}_{yyI} Gram-cm ² $\times 10^5$	\bar{I}_{zzI} Gram-cm ² $\times 10^5$
Pelvis	16.200	128.000	20.000	19.300
L5	2.240	8.185	1.795	2.832
L4	2.187	8.083	1.704	2.291
L3	2.152	8.264	1.682	2.280
L2	2.012	8.354	1.695	2.291
L1	1.960	8.061	1.569	2.212
T12	1.676	7.022	1.309	1.919
T11	1.603	7.056	1.230	1.941
T10	1.352	6.028	1.129	1.648
T9	1.417	6.164	1.230	1.716
T8	1.326	5.543	1.208	1.670
T7	1.308	5.347	1.219	1.659
T6	1.193	4.425	1.162	1.546
T5	1.175	3.838	1.151	1.490
T4	1.064	3.138	1.060	1.354
T3	1.160	2.878	1.174	1.422
T2	1.074	2.077	1.029	1.230
T1	1.359	0.745	0.518	1.716
Head	5.612	44.786	4.044	3.385

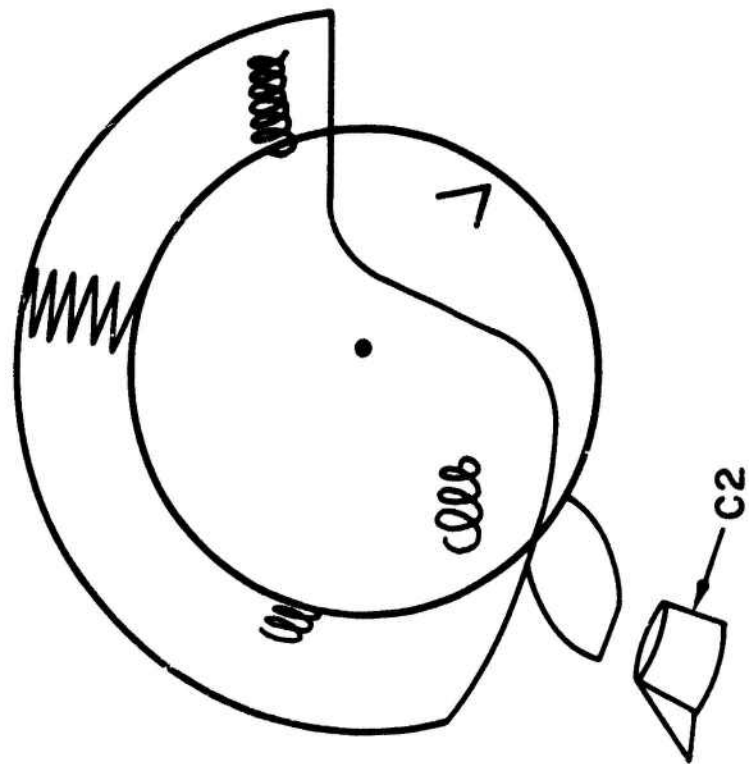
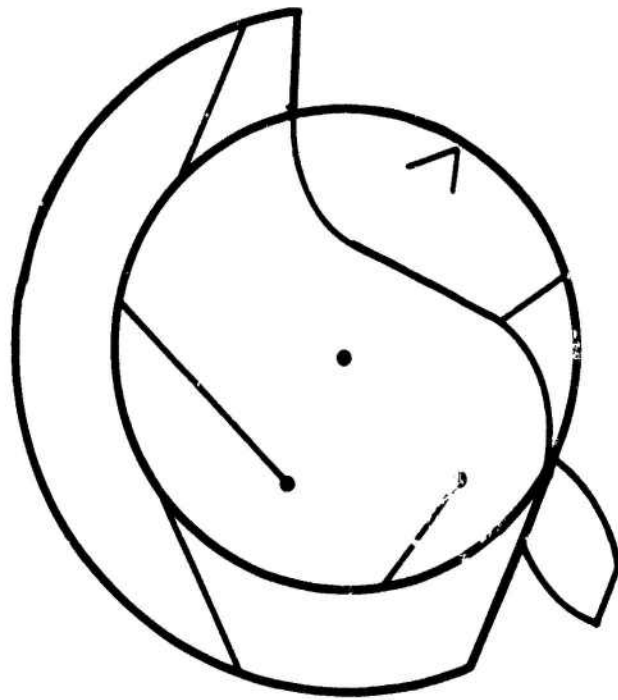


Figure 15. Head-helmet representation.

core) is trabecular bone (soft bone), with a mean modulus of elasticity $E_i = 7.35 \times 10^8$ dynes/cm². These moduli were obtained from Evans (1970). The following aspects of the vertebra's geometry have been neglected:

1. The variation of cross section with z , the cross section of the vertebral body as shown in Fig. 16 is simplified as shown.
2. The ellipticity of the endplates is neglected and a circular cross section is assumed.

The maximum stress for any combination of moment M and axial force P occurs in the cortical bone and is obtained by superimposing the stress due to bending σ_B and the axial stress σ_A . The bending stress is computed from

$$\sigma_B = \frac{x}{\rho} E(r) \quad (4.7)$$

where ρ is the radius of curvature, E is Young's modulus, which is given by

$$E(r) = \begin{cases} E_i & r < r_i \\ E_o & r > r_i \end{cases} \quad (4.8)$$

$$\begin{aligned} M &= \int_A x \sigma_B dA = 4 \int_0^{r_o} \int_0^{\pi/2} \frac{r \cos \theta}{\rho} E(r) r \cos \theta r dr d\theta \\ &= \frac{\pi}{4\rho} \{E_i r_i^4 + E_o (r_o^4 - r_i^4)\} \end{aligned} \quad (4.9)$$

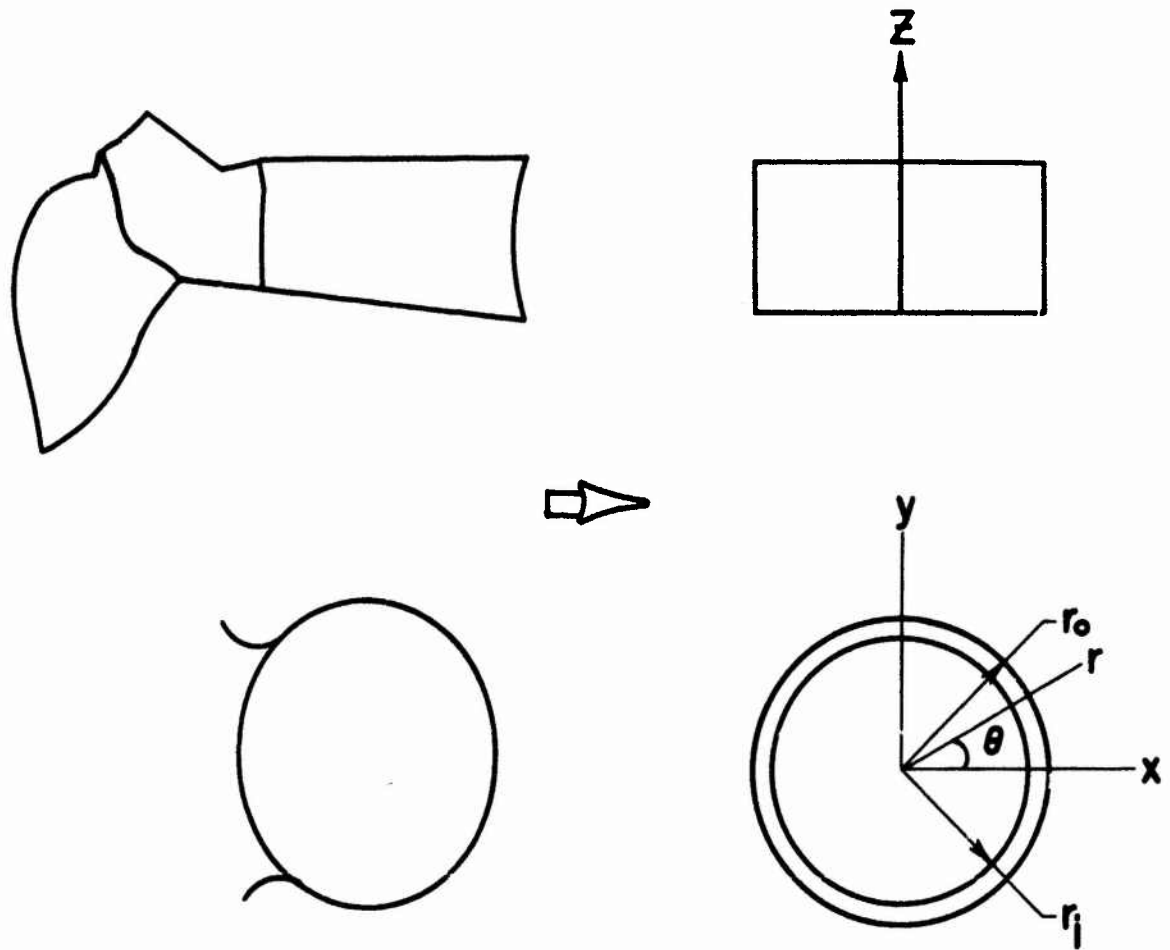


Figure 16. Idealization of vertebral body for preliminary evaluation of injury criteria.

or

$$\frac{1}{\rho} = \frac{4M}{\pi\{E_i r_i^4 + E_o(r_o^4 - r_i^4)\}} \quad (4.10)$$

and

$$\sigma_B = \frac{4Mr\cos\theta E(r)}{\pi\{E_i r_i^4 + E_o(r_o^4 - r_i^4)\}} \quad (4.11)$$

The axial stress due to axial force is given by

$$\sigma_A = E(r)\epsilon_o \quad (4.12)$$

where ϵ_o is constant, and

$$\begin{aligned} P &= \int_A \sigma_A dA = 2\pi\epsilon_o \int_o^{r_o} E(r) r dr \\ &= \pi\epsilon_o \{E_i r_i^2 + E_o(r_o^2 - r_i^2)\} \end{aligned} \quad (4.13)$$

or

$$\epsilon_o = \frac{P}{\pi\{E_i r_i^2 + E_o(r_o^2 - r_i^2)\}} \quad (4.14)$$

and

$$\sigma_A = \frac{P E(r)}{\pi\{E_i r_i^2 + E_o(r_o^2 - r_i^2)\}} \quad (4.15)$$

Next, we superimpose the two stresses and note the maximum occurs at $r = r_o$ and $\theta = 0$. This gives

$$\sigma_{\max} = \frac{4Mr_o E_o}{\pi(E_i r_i^4 + E_o(r_o^4 - r_i^4))} + \frac{PE_o}{\pi(E_i r_i^2 + E_o(r_o^2 - r_i^2))} \quad (4.16)$$

An equivalent circular radius r_o for the vertebral bodies was determined so that the area of the two geometries was the same. The thickness of the cortical bone was assumed to be a constant 0.3 mm for all the vertebrae, i.e. $r_i = r_o - 0.3$ mm. The maximum axial force for each vertebrae were obtained from Payne (1971), who summarized the results of several experiments concerned with the compressive breaking load of individual vertebrae. From this data, the maximum breaking stress under only axial load and the pure moment without axial force were determined. The results of these calculations are summarized in Table 12. As can be seen, the breaking strength as computed by this formula is fairly constant over the entire spine, except for moderate deviations in the lumbar and upper thoracic vertebrae. Figure 25 depicts the moment-axial force interaction line of several vertebral levels (alternating levels were omitted for clarity). Each point on a line represents the combination of moment and axial force which corresponds to the maximum stress for that vertebral level.

Table 12

Summary of Maximum Stress Calculations

Level	Equivalent Radius r_0 (cm)	Experimental Axial Failure Load (10^8 dynes)	Computed Failure Moment (10^8 dyne-cm)	Axial Failure Stress by Eq. (4.15) (10^9 dyne/cm ²)
L5	2.165	10.29	10.19	2.18
L4	2.203	9.80	9.87	2.03
L3	2.154	9.31	9.18	1.98
L2	2.078	8.82	8.40	1.95
L1	2.019	8.33	7.72	1.91
T12	1.972	7.84	7.11	1.84
T11	1.883	7.35	6.37	1.82
T10	1.781	6.86	5.64	1.81
T9	1.690	6.37	4.98	1.78
T8	1.619	5.88	4.41	1.73
T7	1.538	5.58	3.98	1.74
T6	1.437	5.29	3.53	1.78
T5	1.388	4.90	3.16	1.71
T4	1.323	4.60	2.84	1.69
T3	1.271	4.21	2.49	1.62
T2	1.226	3.92	2.24	1.57
T1	1.162	3.62	1.96	1.54

7. Inertial Properties

Inertial properties for the motion segments of the isolated thoracolumbar spine were taken from Liu, et al (1973) and are given in Table 11. Inertial properties for the rib cage model were assigned by attributing 10% of the thoracic mass to this portion of skeletal structure. For the viscera model the lumbar mass was equally distributed among the five vertebrae and two rigid bodies used in the model. The sagittal plane rotational inertia of the lumbar vertebrae were reduced based on measurements and calculations obtained from anatomical cross sectional geometries. A summary of the inertial properties of the spine torso model with rib cage is given in Table 13. Inertial properties for the cervical motion segments were obtained by distributing the mass uniformly at each vertebral level; see Table 13.

Table 13. Inertial Properties for Complete Model

Motion Segment	Mass ρ_I Grams x 10^3	\bar{I}_{xxI} Gram-cm 2 x 10^4	\bar{I}_{yyI} Gram-cm 2 x 10^5	\bar{I}_{zzI} Gram-cm 2 x 10^5
Pelvis	16.200	128.000	20.000	19.300
L5	1.500	2.783	1.795	2.382
L4	1.500	2.748	1.704	2.291
L3	1.500	2.809	1.682	2.280
L2	1.500	2.840	1.695	2.291
L1	1.500	2.740	1.569	2.212
T12	1.556	7.002	1.309	1.919
T11	1.453	7.056	1.230	1.941
T10	1.202	6.028	1.129	1.648
T9	1.267	6.164	1.230	1.716
T8	1.176	5.543	1.208	1.670
T7	1.158	5.347	1.219	1.659
T6	1.043	4.425	1.162	1.546
T5	1.025	3.383	1.151	1.490
T4	0.964	3.138	1.060	1.354
T3	1.010	2.878	1.174	1.422
T2	0.974	2.007	1.029	1.230
T1	1.209	0.745	0.518	1.716
C7-C2	1.000	0.700	0.500	1.500
Head	5.612	44.786	4.044	3.385
Ribs T1 to T10	0.074	0.373	0.074	0.074
Lower Viscera	1.500	10.700	0.550	1.000
Upper Viscera	1.500	10.700	0.550	1.000

8. Summary of Models

Model I, shown in Figure 17, consists of

- i. thoracolumbar spine
- ii. a single beam element which represents the cervical spine
- iii. pelvis
- iv. head

Model II, shown in Figure 18, consists of

- i. thoracolumbar spine
- ii. a single beam element for cervical spine
- iii. rib cage
- iv. viscera represented by hydrodynamic elements
- v. pelvis
- vi. head

Model III, shown in Figure 19, consists of

- i. thoracolumbar spine
- ii. cervical spine modelled as individual vertebrae
- iii. pelvis
- iv. head

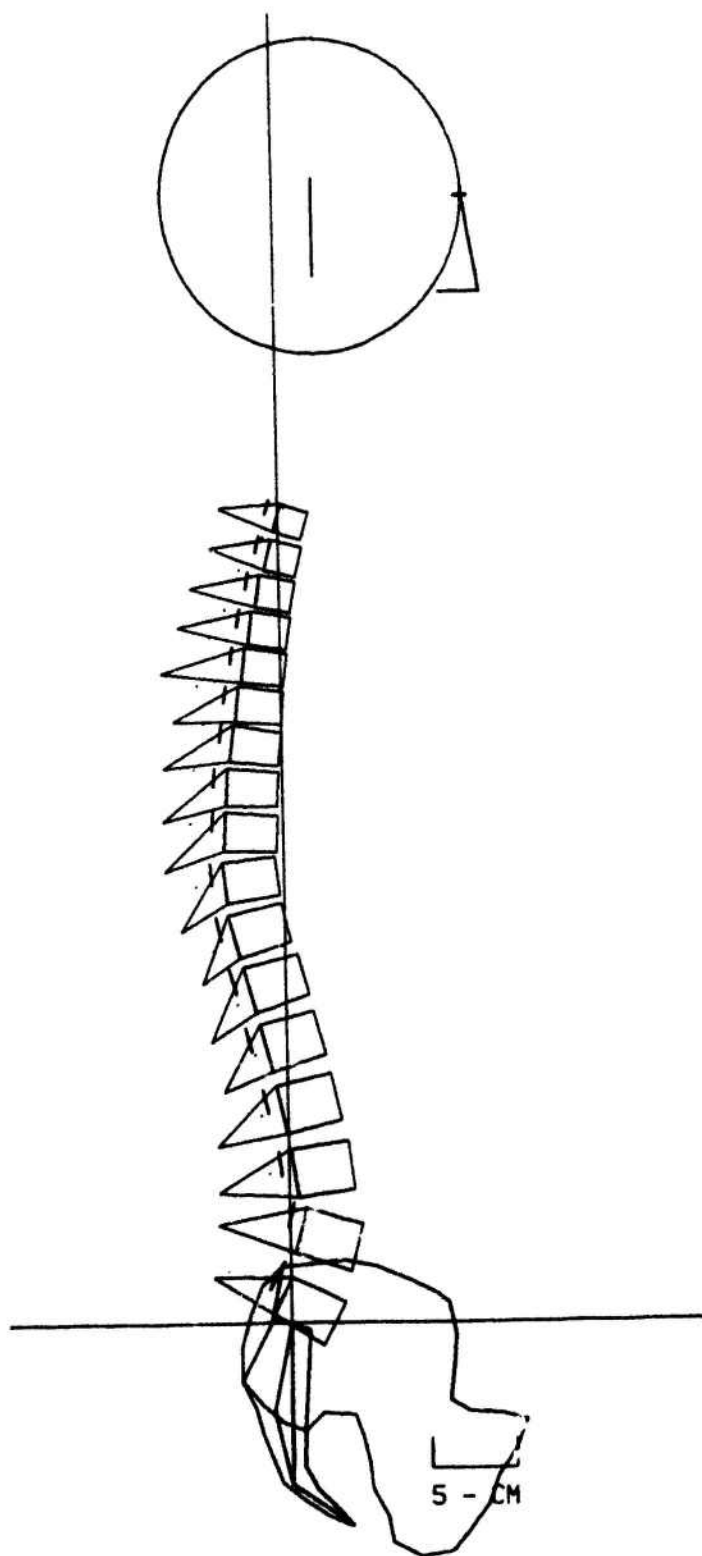


Figure 17. Side view of Model I.

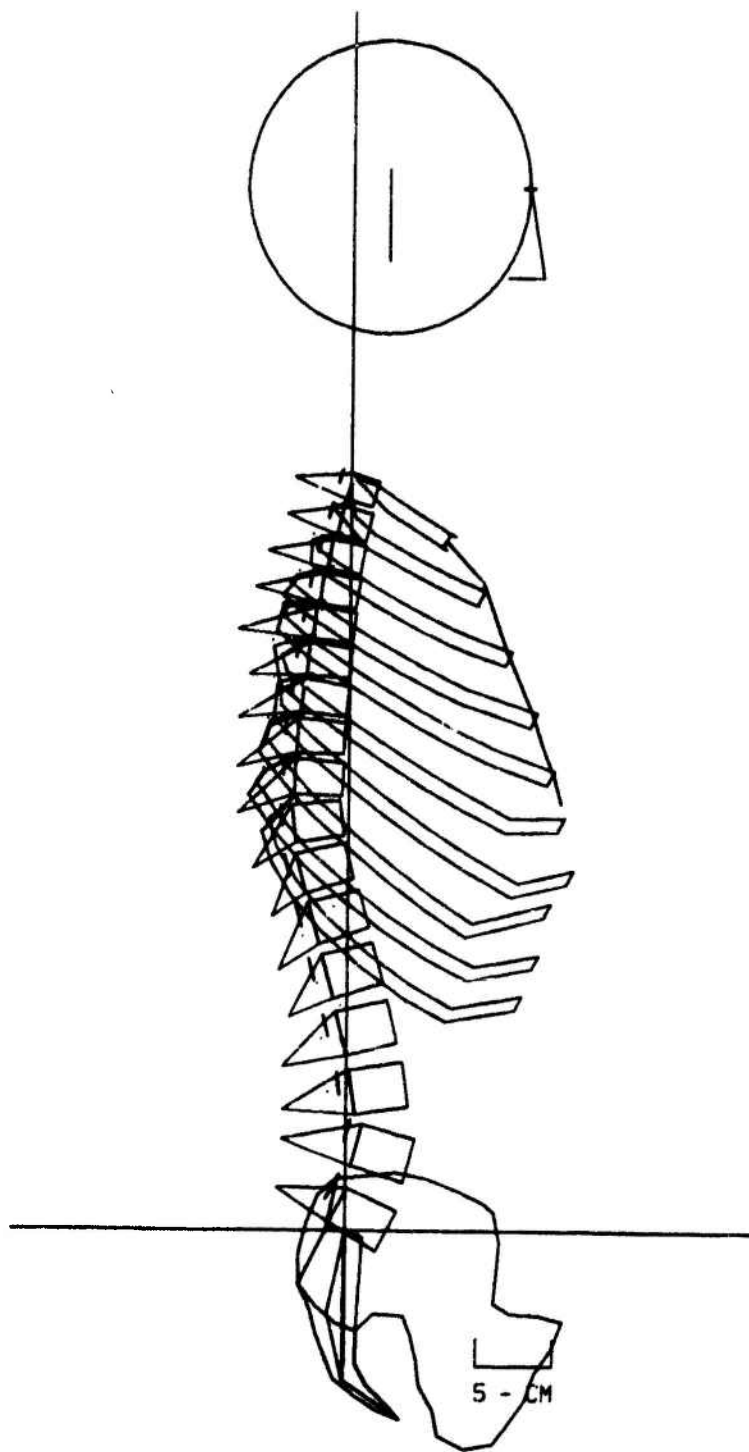


Figure 18. Side view of Model II.

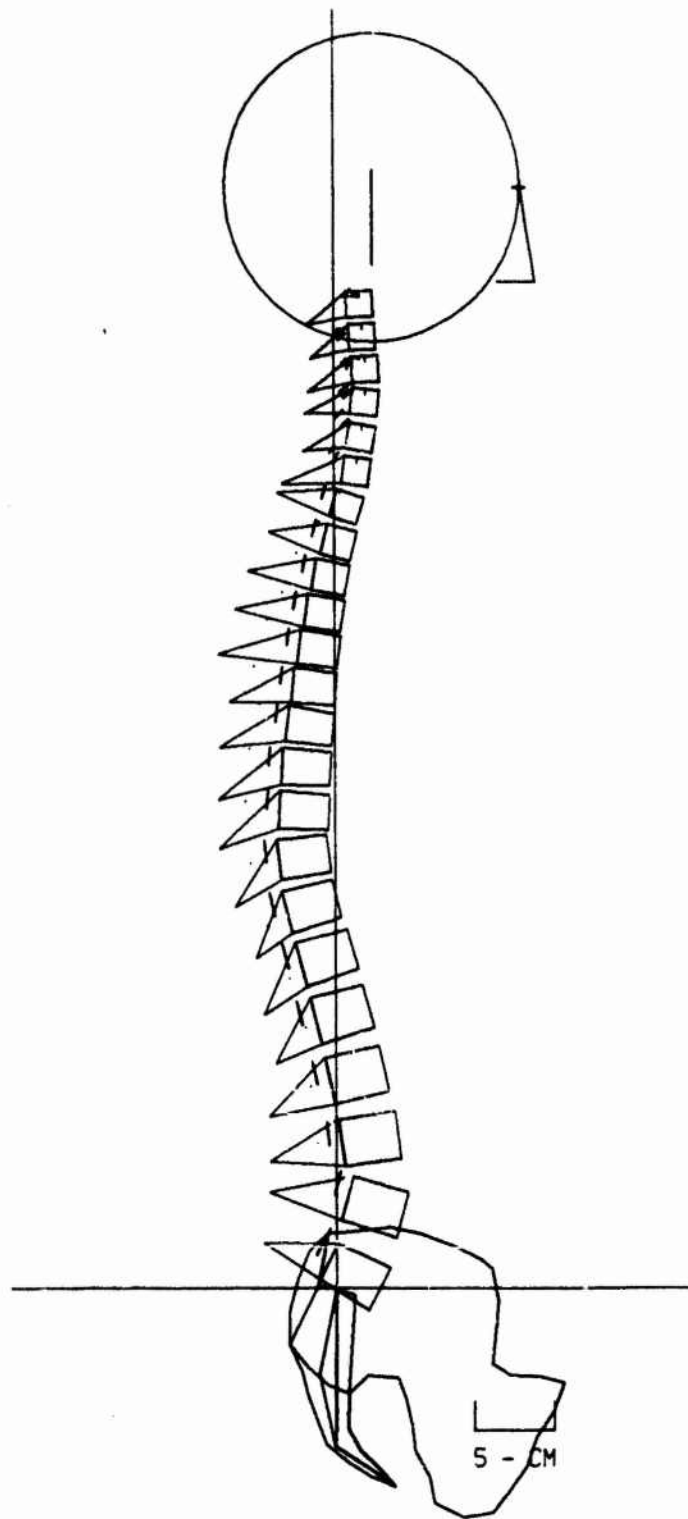


Figure 19. Side view of Model III.

CHAPTER V
STUDIES OF SPINAL RESPONSE

1. Isolated Ligamentous Spine Model

The first group of studies reported here were conducted with the model of the isolated ligamentous spine described as Model I in the previous chapter. All of these problems were studied as three dimensional problems, even though in most cases a two dimensional model would have been adequate. In all cases, explicit integration was used with a time increment of 10^{-4} seconds, requiring 800 time steps for a solution at 80 msec.

Response of unrestrained spine under $10 G_z$. The first study was made to evaluate the response of the isolated ligamentous spine under a perfectly vertical $10G_z$ acceleration. A rate of onset of 714 g/sec was used; the acceleration was then maintained at a constant level of 10g for 66 msec. Unlike other studies described in this section, no seatback or restraints were included in this solution.

The deformed configurations at 40, 60 and 80 msec are shown in Figs. 20, 21, and 22. As can be seen, particularly at 80 msec, severe curvatures of the spine have developed, and the spinal column can be considered to have buckled. Once the column has buckled, the computed response is quite unrealistic. For example, moments on the order of 3000 N-cm are developed in the lumbar spine.

Liu, et al (1973) have observed a similar response in a homo-

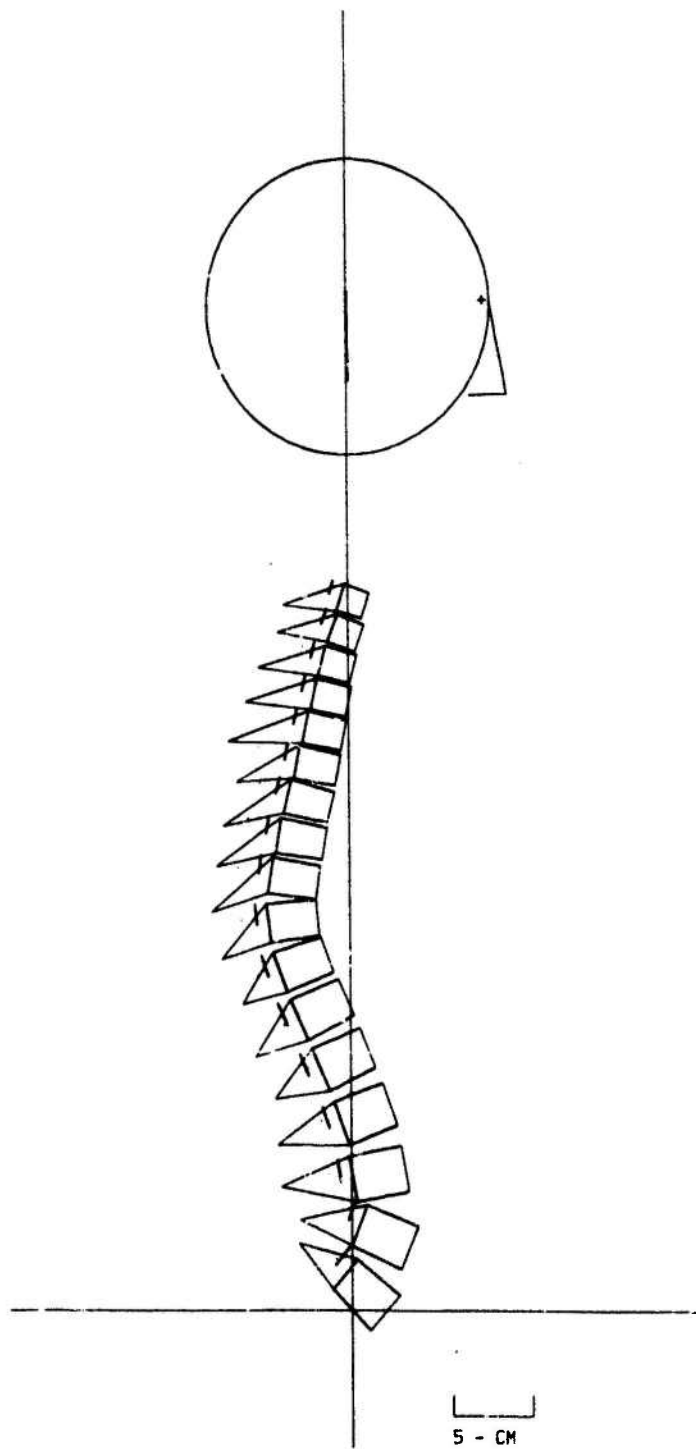


Figure 20. Response of unrestrained spine at 40 msec.

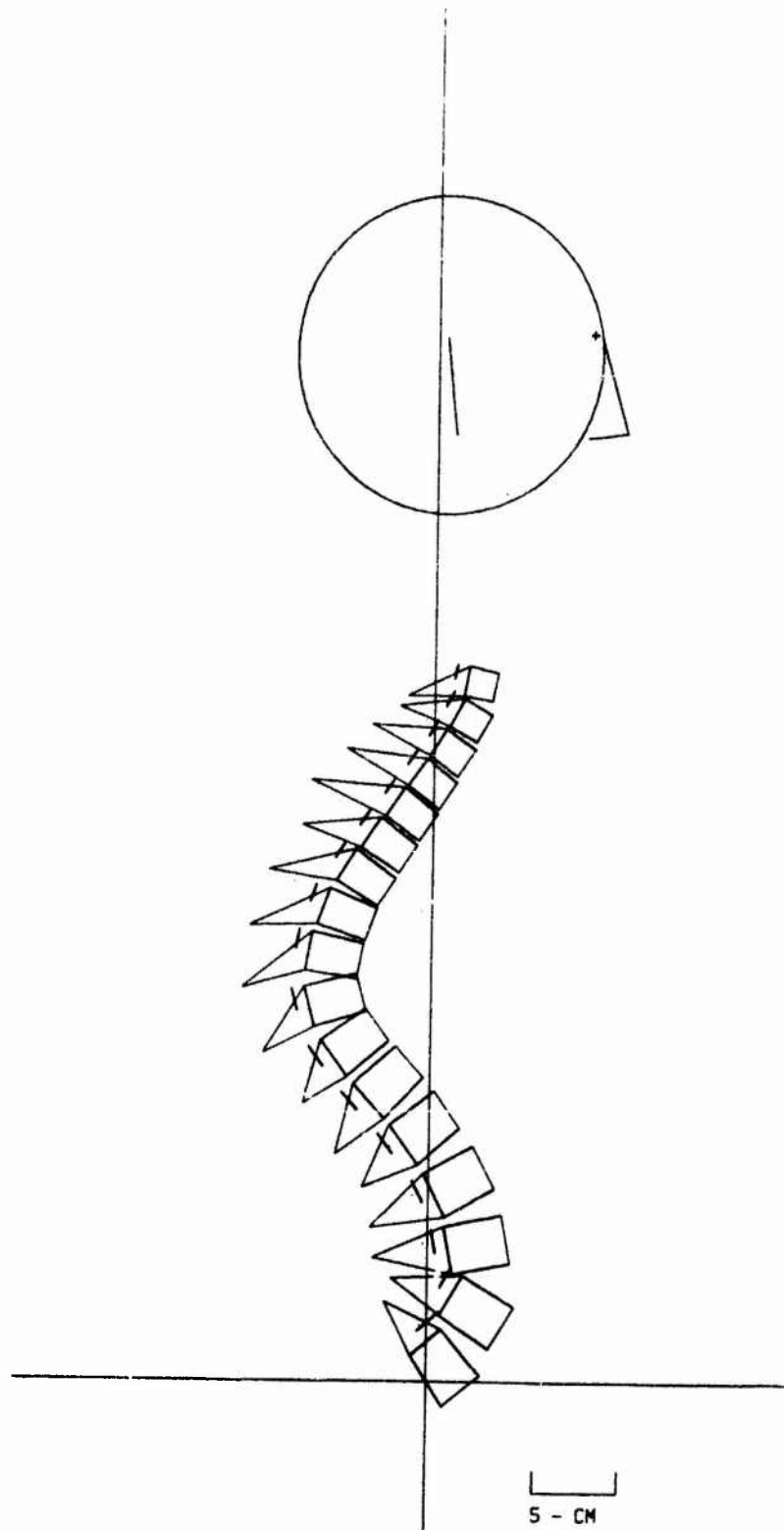


Figure 21. Response of unrestrained spine at 60 msec.

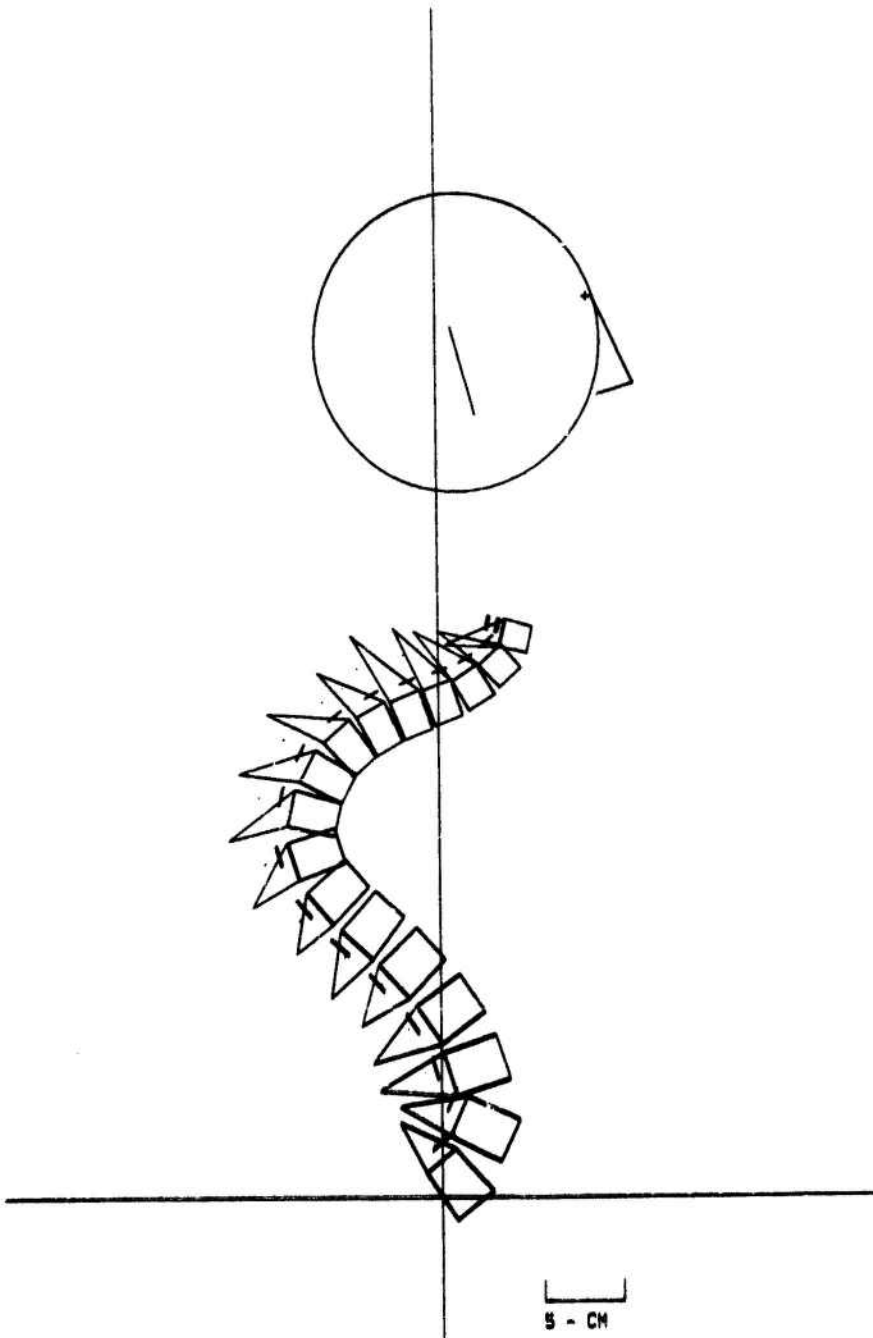


Figure 22. Response of unrestrained spine at 80 msec.

geneous bar model of the spine, but were inconclusive as to whether this response is correct. However, if one considers that Lucas and Bressler (1961) have shown a static frontal plane buckling load of 20 to 100 Newtons for the thoracolumbar spine constrained against sagittal plane buckling, then this response is not unexpected. The bending stiffness of the isolated spine in the sagittal plane is of the same order as the bending stiffness in the frontal plane, and the initial sagittal plane curvature of the spine reduces its sagittal mode buckling even further. The $10G_z$ environment results in axial loads of 4500 Newtons, and the duration is on the order of 200 msec, which, as shown subsequently, is of the order of the lowest flexural periods and 4 times the axial period of the spinal column, so inertial effects cannot preclude buckling. Hence it is not unexpected that the unrestrained spine will buckle in this environment.

There are essentially two mechanisms that prevent buckling in the actual spine:

- i. the action of the restraint system, seatback and musculature;
- ii. the interaction with the torso and rib cage, which may significantly increase the bending stiffness of the composite spine/torso.

The results in subsequent Sections reflect some attempts to study the effects of the second mechanism. In all studies described in the remainder of this section, the seatback, restraint system, and a simplified torso representation were included. These were sufficient to eliminate buckling.

An alternative to including constraints in the model would be to use a small displacement method of analysis. However, small displacement analyses are valid only as long as the actual displacements of the spine are small. In problems such as that of eccentric head loading, large displacements are undoubtedly encountered and would invalidate a small displacement analysis.

Another point of interest in the response of this model is that the effects of the ligaments are minimal. Because of the large compression of the discs, the ligaments as modelled here all become slack and provide no stiffness. This situation continues even as buckling is initiated: the ligaments do not prevent buckling. This is also true of the spring models of the articular facet joint.

Effect of sagittal plane curvature. Two distinct curves characterize the sagittal plane curvature; the lumbar curve formed by the vertebrae L5 through L1, and the thoracic curve consisting of T12 through T1. Sagittal plane curvature changes from concave to convex (when viewed posteriorly) in the region between L2 and T11. In this study three magnitudes of sagittal curvature were simulated. The first, shown in Fig. 23, represents a seated configuration in which the lumbar curvature averages 0.045 cm^{-1} and the thoracic curvature 0.017 cm^{-1} . This configuration was chosen to illustrate an occupant with large lumbar curvature. The second, shown in Fig. 24, is an erect configuration in which the average lumbar curvature is 0.025 cm^{-1} . This configuration is based on several radiographs of pilots in ejection seats. The

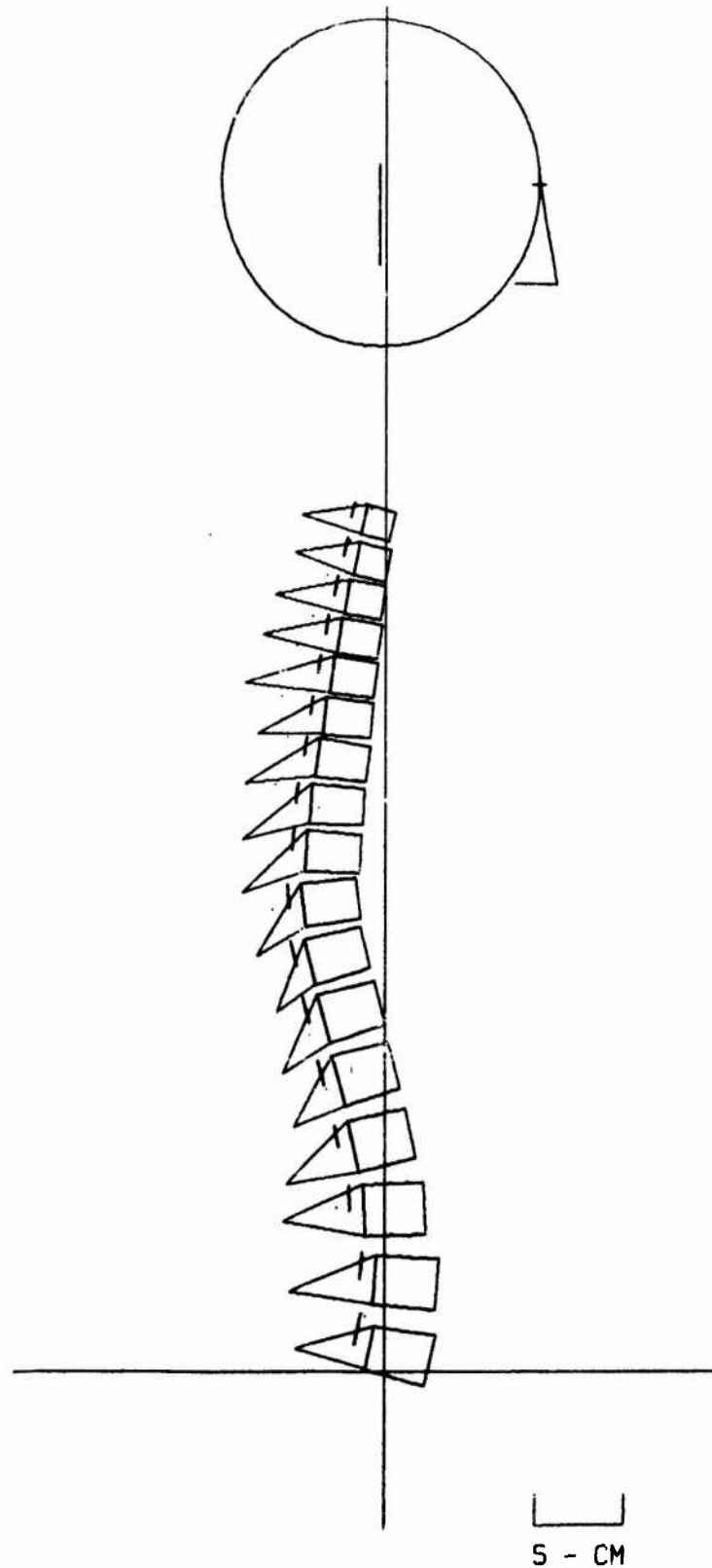


Figure 23. Seated Configuration with Large Lumbar Curvature.

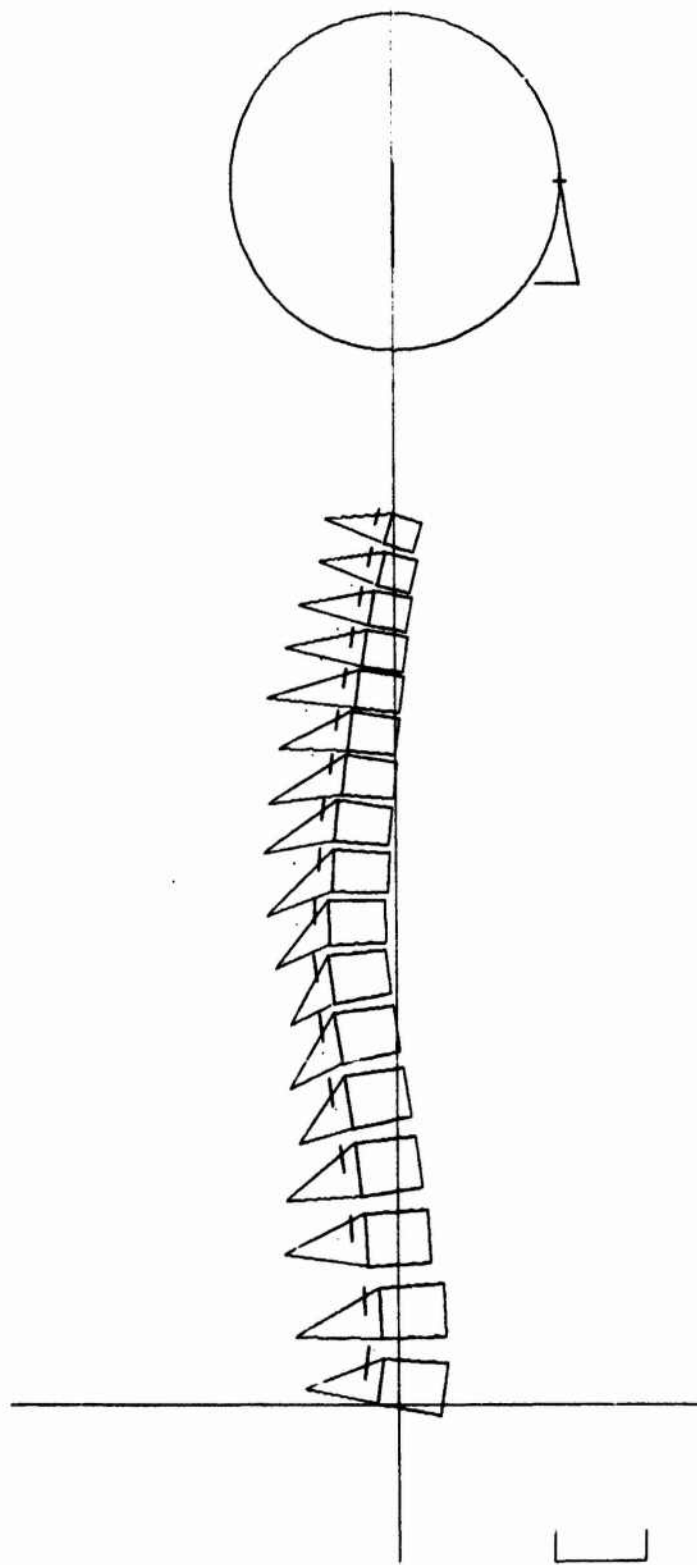


Figure 24. Erect seated configuration.

third, shown in Fig. 25, represents a hypothetical configuration in which all sagittal plane curvature has been eliminated. In this "straight spine" model all of the intervertebral disc elements are along the vertical axis as are the mass centers.

The maximum axial forces, Fig. 26, for the three configurations decrease smoothly from bottom to top, particularly in the "straight spine" model, and the curvature has little effect on the values. On the other hand, a comparison of maximum sagittal plane moments for the three models, Fig. 27, shows large differences among the models. The maximum sagittal plane moment in both curved spines occurs at L1-T12, the point where spinal curvature changes from concave to convex. In general, the sagittal plane moments for the erect configuration are smaller than for the curved configuration at all levels, while in the straight spine, the moments are smallest. These results indicate that the pre-ejection configuration of the pilot is an important factor. While the compressive forces in the vertebrae are not effected by configuration changes, the additional stress due to the large bending moments acting on the vertebrae may increase the possibility of injury.

Figures 28 and 29 show the maximum moment and axial force predicted by the model for both of the curved configurations in the vertebral bodies, to illustrate the simplified injury potential model developed in Chapter IV. The axial force and moment values shown represent the average of the axial forces and moments for each vertebrae in the discs immediately above and below it. These values, in all cases, are the maximum that were observed

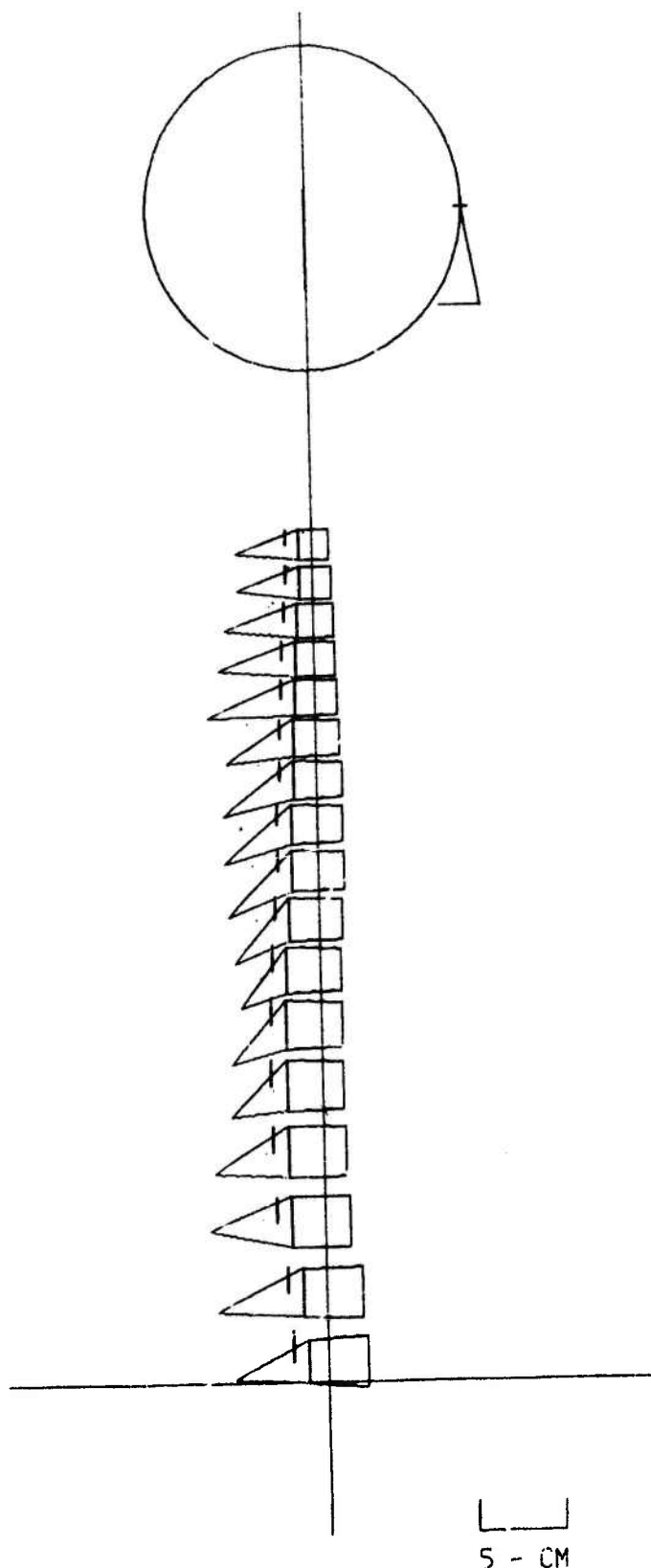


Figure 25. Straight spine configuration.

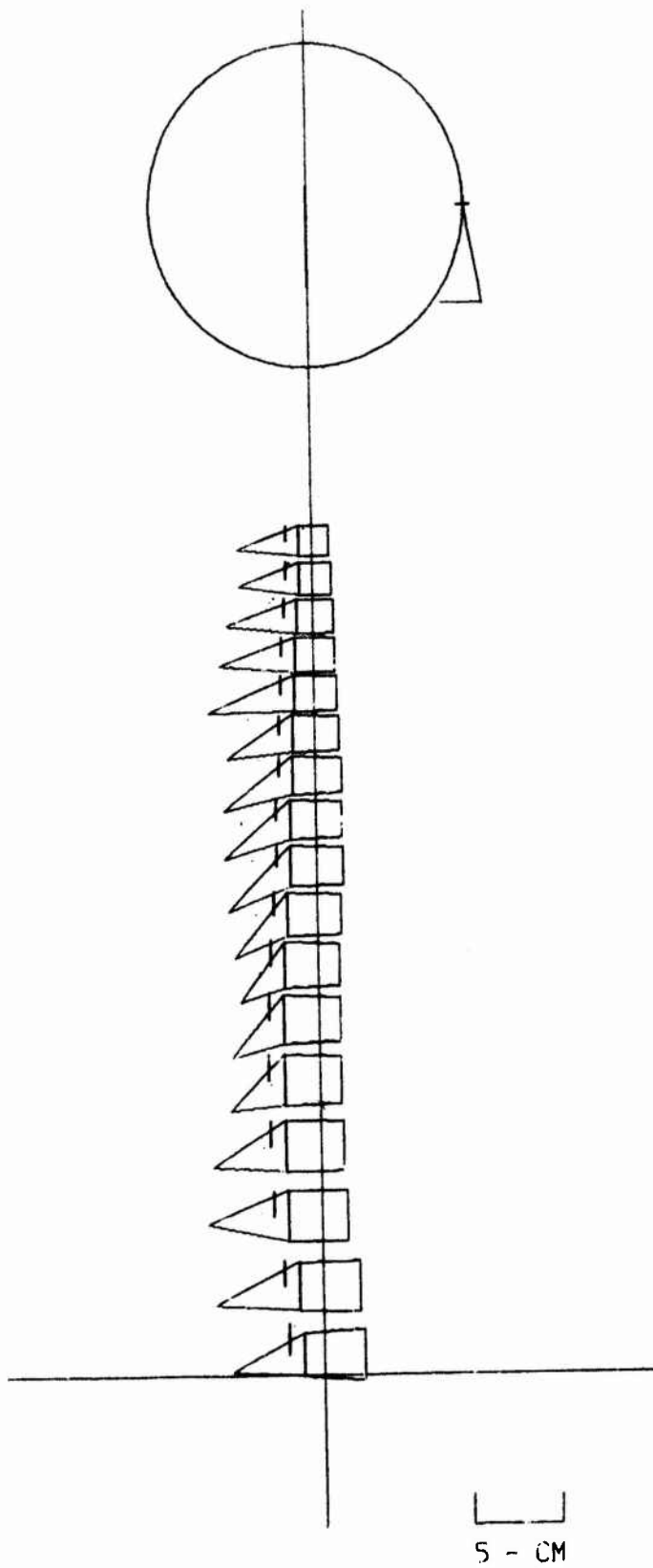


Figure 25. Straight spine configuration.

MAXIMUM AXIAL FORCE

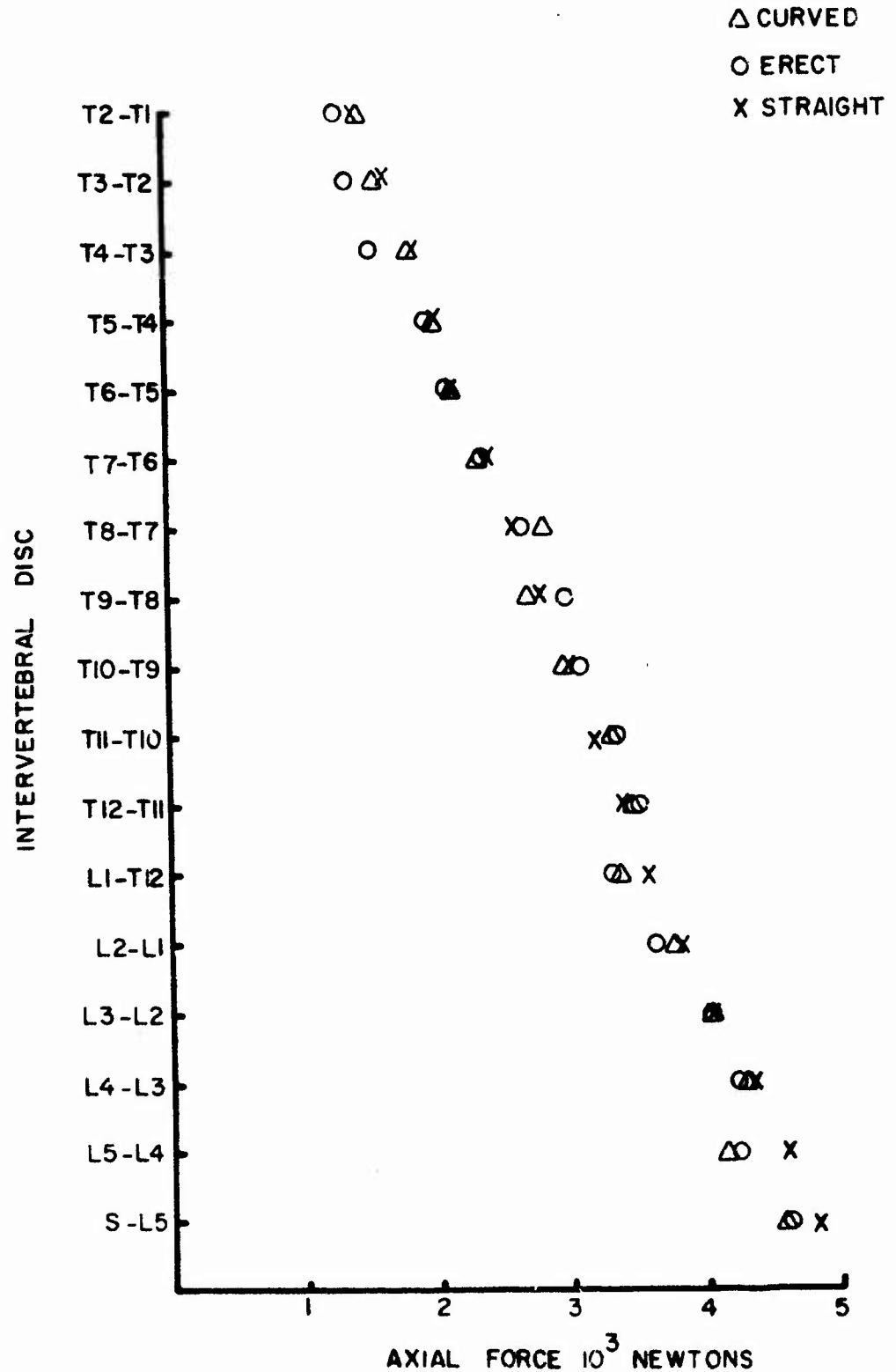


Figure 26. Comparison of maximum axial forces in spines with and without sagittal plane curvature.

MAXIMUM MOMENTS

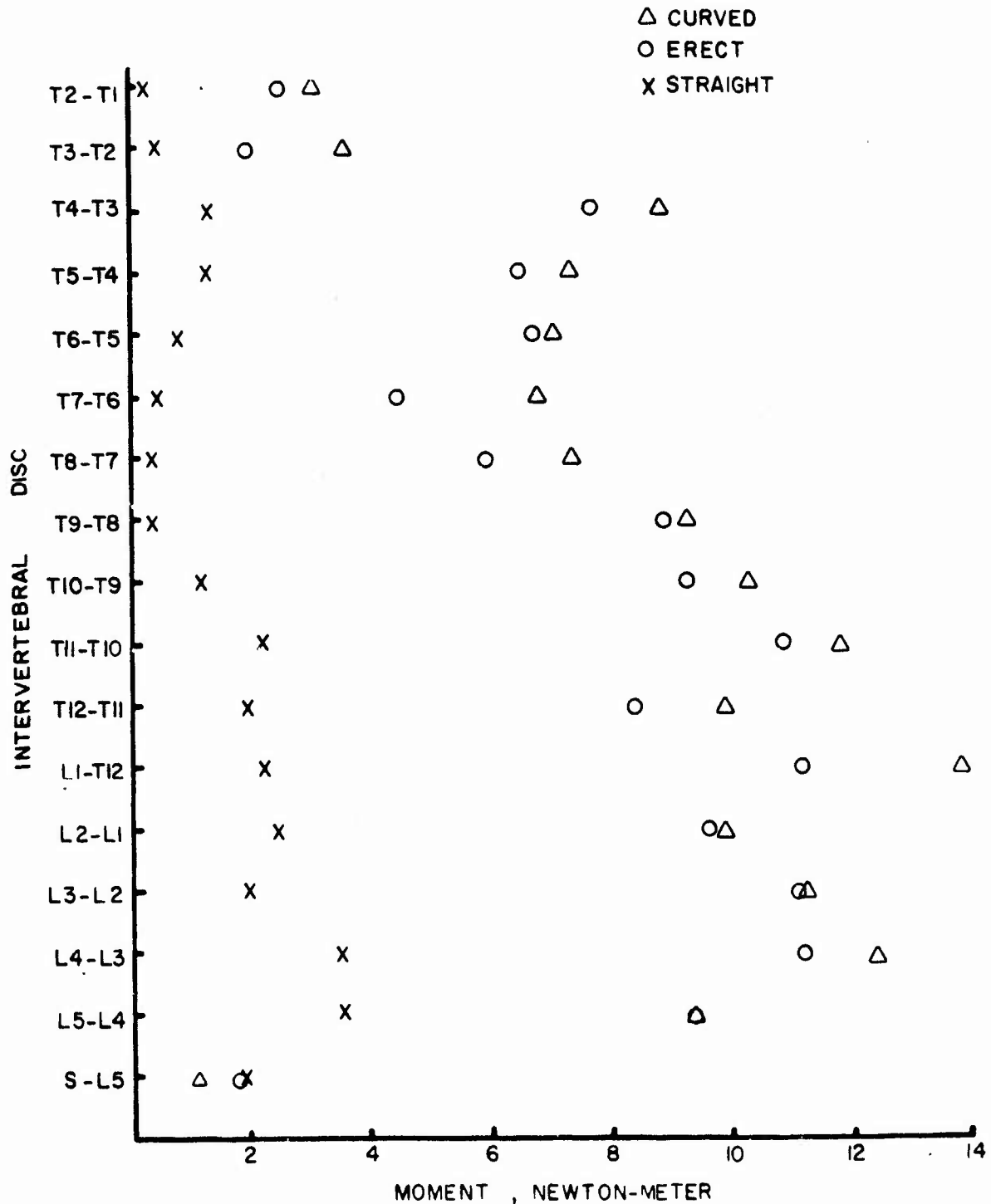


Figure 27. Comparison of maximum bending moments in spines with and without sagittal plane curvature.

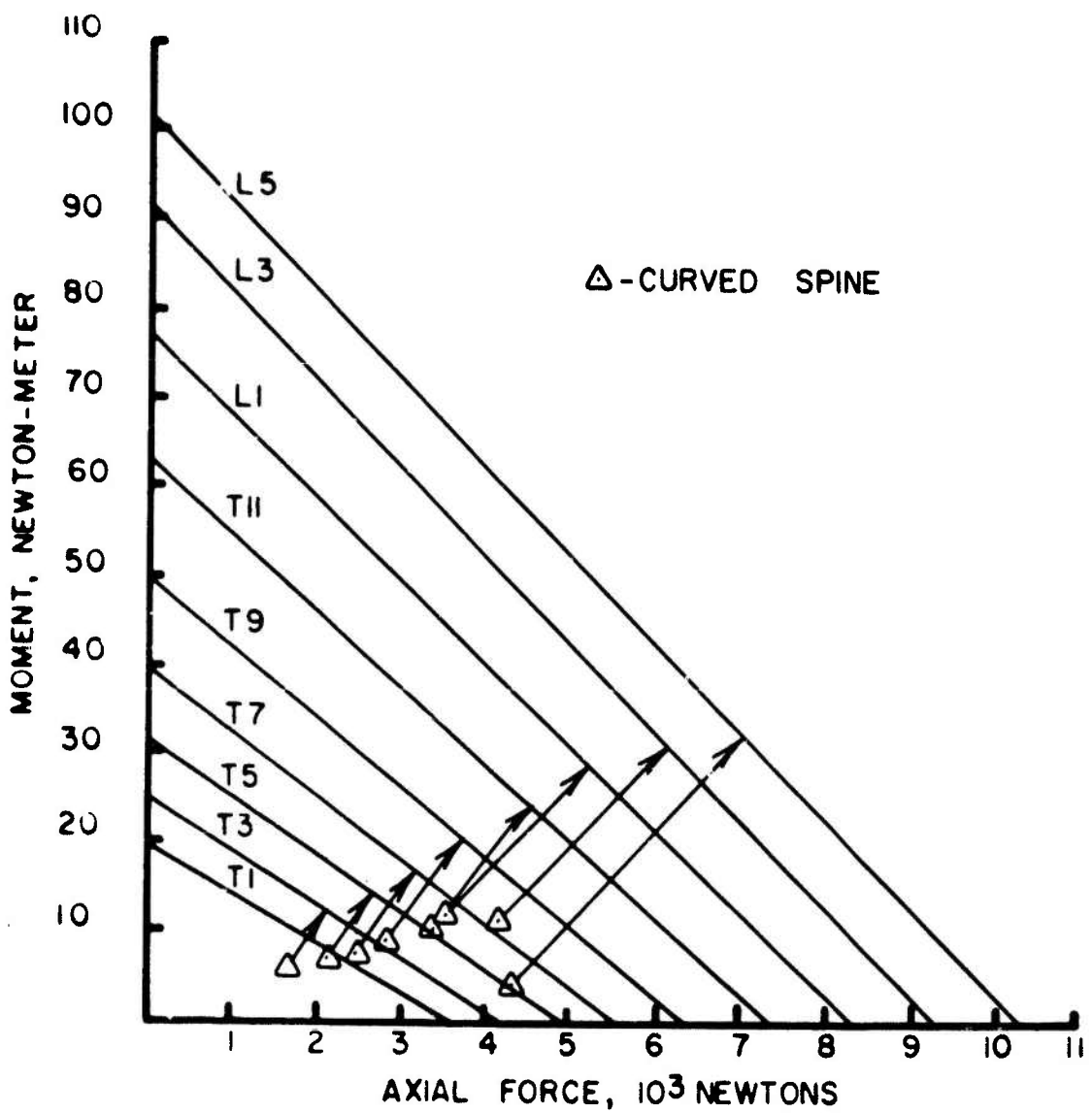


Figure 28. Injury potentials for large lumbar curvature spine.

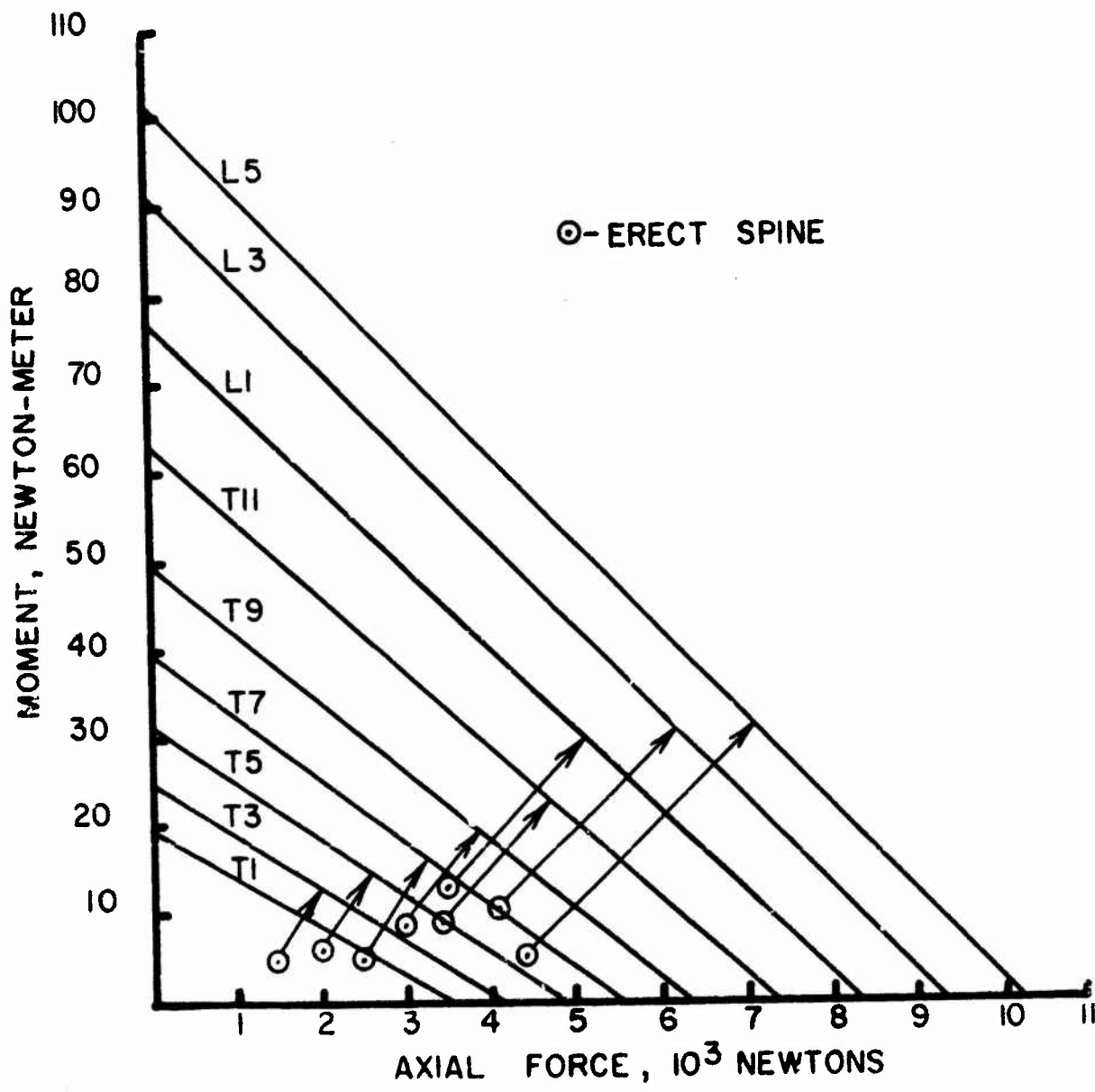


Figure 29. Injury potentials for erect spine.

during the 80 msec simulation (the maximum axial forces and moments do not necessarily occur at the same time). The length of the line segment with the arrow, relative to the distance of the limit load from the origin, is one indication of the probability of no injury at a level (if the point falls inside the limit line). Thus, the probability of injury is somewhat greater for the more curved spine, particularly in the T1-T5 region, where the distance to the injury line is almost 20% less for the more curved spine. Particularly if we consider the possibility that the moments may serve as a triggering factor for failures, then the curved spine, with its greater moments appears to have a greater injury potential.

Rate of Onset. One of the parameters of interest in the ejection problem is the effect of changes in the rate of onset for the acceleration. Rapid rates of onset result in dynamic magnification of force and acceleration magnitudes. Hess and Lombard (1957) reported that onsets of about 60 msec produced considerably higher acceleration levels in the body than the maximum acceleration of the ejection seat. Alternatively, slower onset rates, (100 msec) do not magnify acceleration levels, but may not provide adequate displacement of the pilot to clear the aircraft in the required time. Two ramp acceleration profiles were simulated here. In both the maximum acceleration is 10g; the slower onset profile reached the maximum acceleration at 40 msec with an onset rate of 250g/sec, the other profile reached maximum acceleration at 14 msec with an onset rate of 714g/sec.

Comparison of the maximum acceleration of the head showed a 19.07g peak at 60 msec for the rapid onset of 18.03g peak at 72 msec for the slow onset, which is a 5% reduction in the acceleration level. Similarly, a comparison of maximum forces in the lumbar region showed the axial disc forces were reduced by about 8%. Also the sagittal plane moments and facet forces were reduced by 10% to 15%. Thus the model predicts, as expected, that slower rates on onset reduce the dynamic magnification of axial loads and accelerations and reduce the overall bending response of the spine. Time histories of the head acceleration and forces are shown in Figs. 30 to 33.

Angled Pulse (slanted seat). The orientation of the ejection seat with respect to the direction of the acceleration vector is another consideration in the ejection problem. By reclining the seat so that the acceleration vector has a slight anterior component with respect to the axis of the spine, two beneficial effects are introduced: (1) the acceleration component along the axis of the spine is reduced, and (2) the resulting anterior component of acceleration provides support for the spine by forcing the seat-back against the torso. Two orientations of the acceleration vector were studied, one in which the axis of the spine and acceleration vector were aligned vertically with a peak acceleration magnitude of 10g, and the other with a 30° included angle and a 10g peak acceleration magnitude resulting in 8.66g component along the axis of the spine and a 5g anterior component.

Table 14 compares the maximum lumbar forces for three simula-

HEAD ACCELERATION

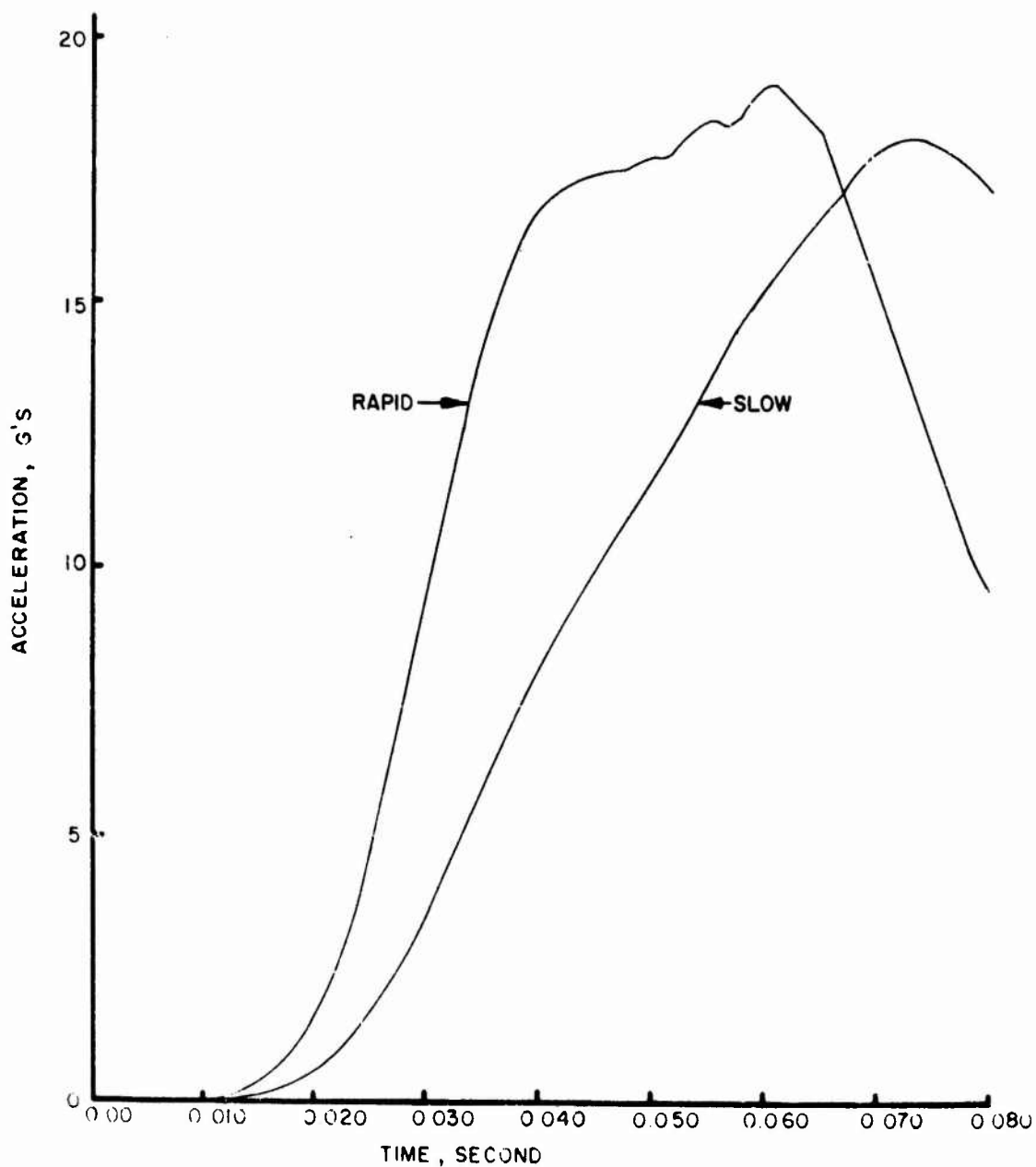


Figure 30. Comparison of head acceleration for fast and slow rate of onset.

L4-L3 AXIAL FORCE

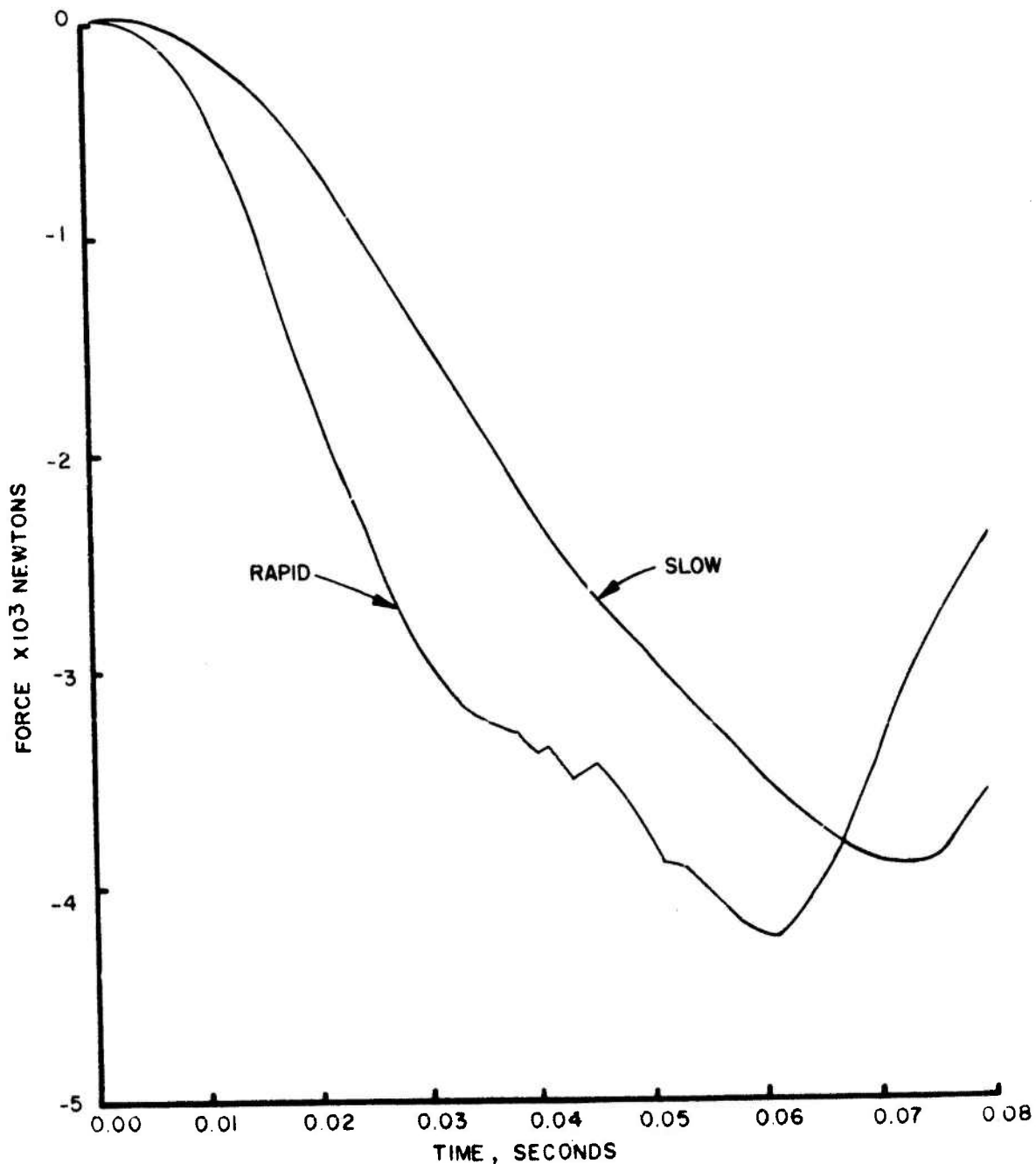


Figure 31. Comparison of axial force in L4/L3 for fast and slow rate of onset.

L3-L2 FACET FORCE

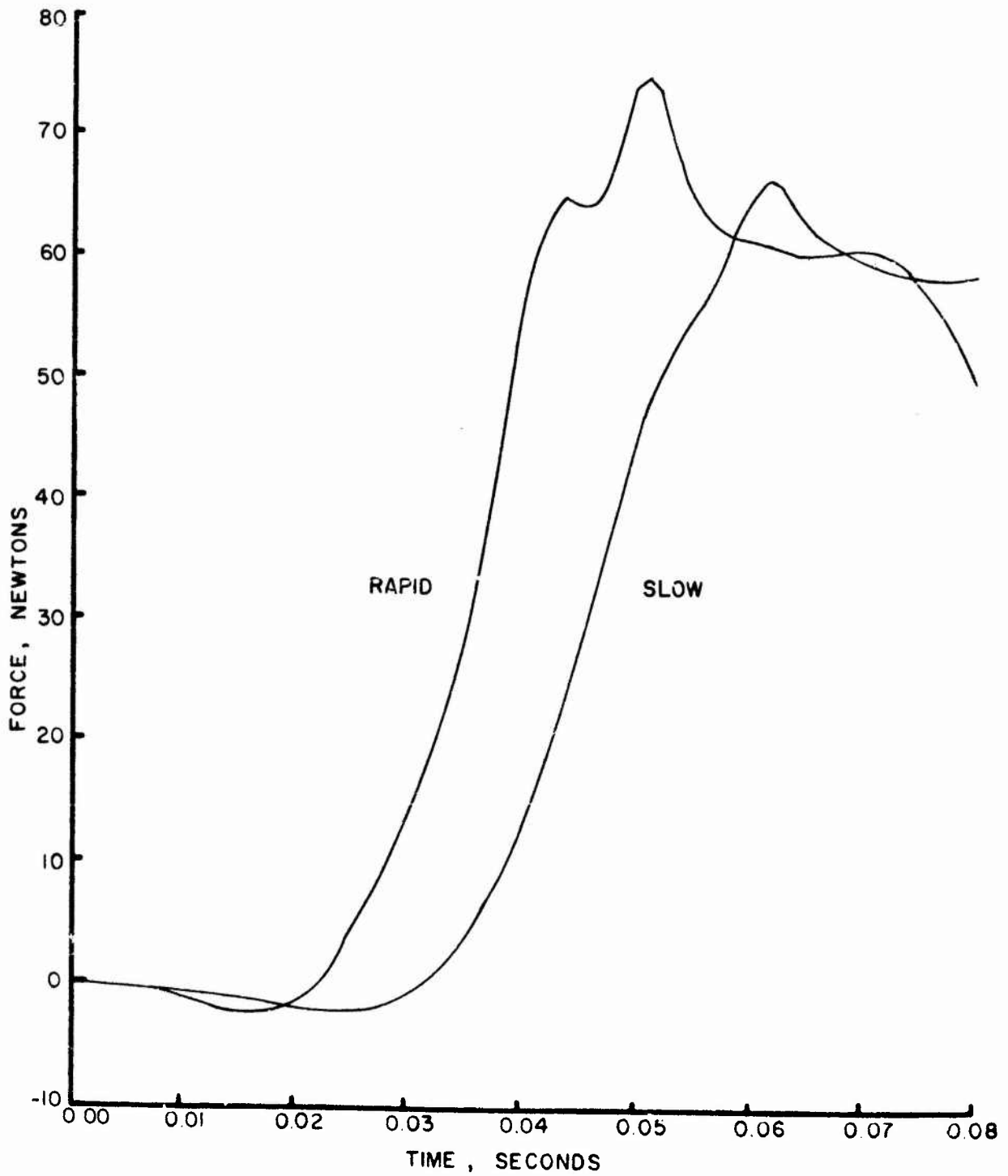


Figure 32. Comparison of facet force in L3/L2 for fast and slow rate of onset.

T4-T3 MOMENT

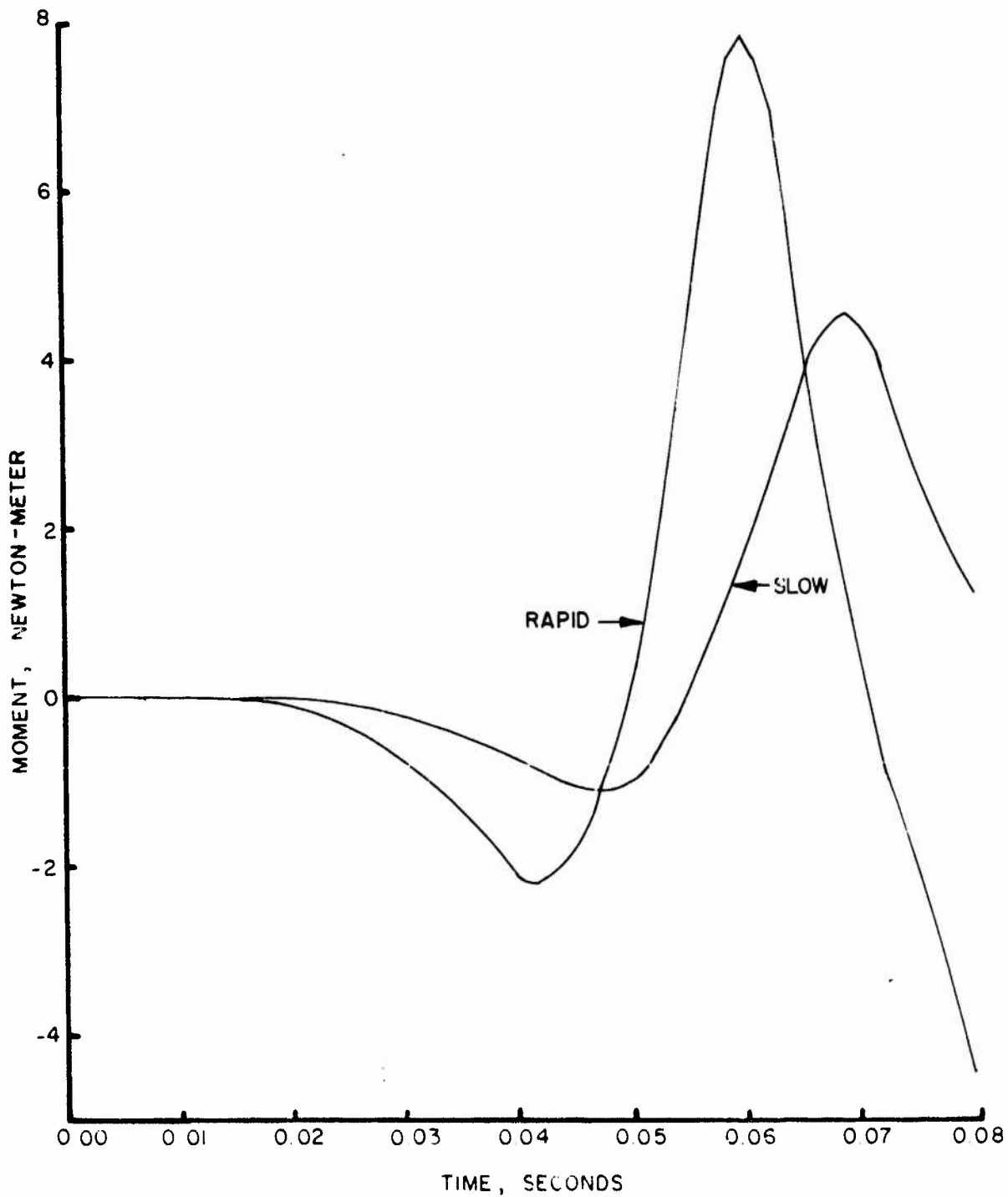


Figure 33. Comparison of moment in T4/T3 for fast and slow rate of onset.

Table 14. Comparison of Response for 30° Angle and Vertical Ejection

Disc Level	Axial Force 10 ³ Newtons			Moment Newton-Meters			Facet Force Newtons		
	30° Rapid Onset	0° Slow Onset	0° Rapid Onset	30° Rapid Onset	0° Slow Onset	0° Rapid Onset	30° Rapid Onset	0° Slow Onset	0° Rapid Onset
L5-L4	-3.50	-3.96	-4.27	9.33	8.18	9.40	32.7	15.8	23.7
L4-L3	-3.39	-3.91	-4.24	9.49	10.47	11.19	50.8	57.9	63.2
L3-L2	-3.26	-3.69	-4.03	9.26	10.03	11.11	59.9	66.2	74.7
L2-L1	-3.03	-3.39	-3.68	7.29	7.74	9.56	61.9	67.7	80.9
L1-T12	-2.89	-3.01	-3.32	-10.52	-9.06	-11.11	26.4	34.0	36.9

tions of 80 msec duration: rapid onset with 30° included angle, slow onset with no angle, and rapid onset with no included angle. These results show a similarity in response for the rapid onset at a 30° angle and the slow onset at a 0° angle, while the rapid onset at 0° exhibits generally higher force levels. The similarity in results for the rapid onset at 30° and the slow onset at 0° can be attributed to a reduction in the effective inertial forces in both simulations. In the slow onset simulation, the effective inertial force is reduced by the decrease in dynamic magnification. In the rapid onset at 30° , a similar reduction in inertial force results from the action of the seatback, which supports part of the inertial load.

These results appear to indicate that within the constraints of maximum possible seat angle and the required displacement of the ejection seat for clearance of the aircraft, an optimum combination of seat angle and rate of onset could be determined. This optimum solution should reduce force levels in the spine.

Eccentric Head Loading. An eccentric head mass, which represents a helmet mounted device, was chosen to illustrate the behavior and applicability of the model to this class of problems. In this study, the head, in addition to its own mass, included a rigidly connected 0.9 kg mass located 0.102 meters from the sagittal plane. Because of the positioning of the added mass, the problem is not symmetric about the sagittal plane, and a three dimensional analysis is needed.

Figure 34 shows the axial force time histories at three levels

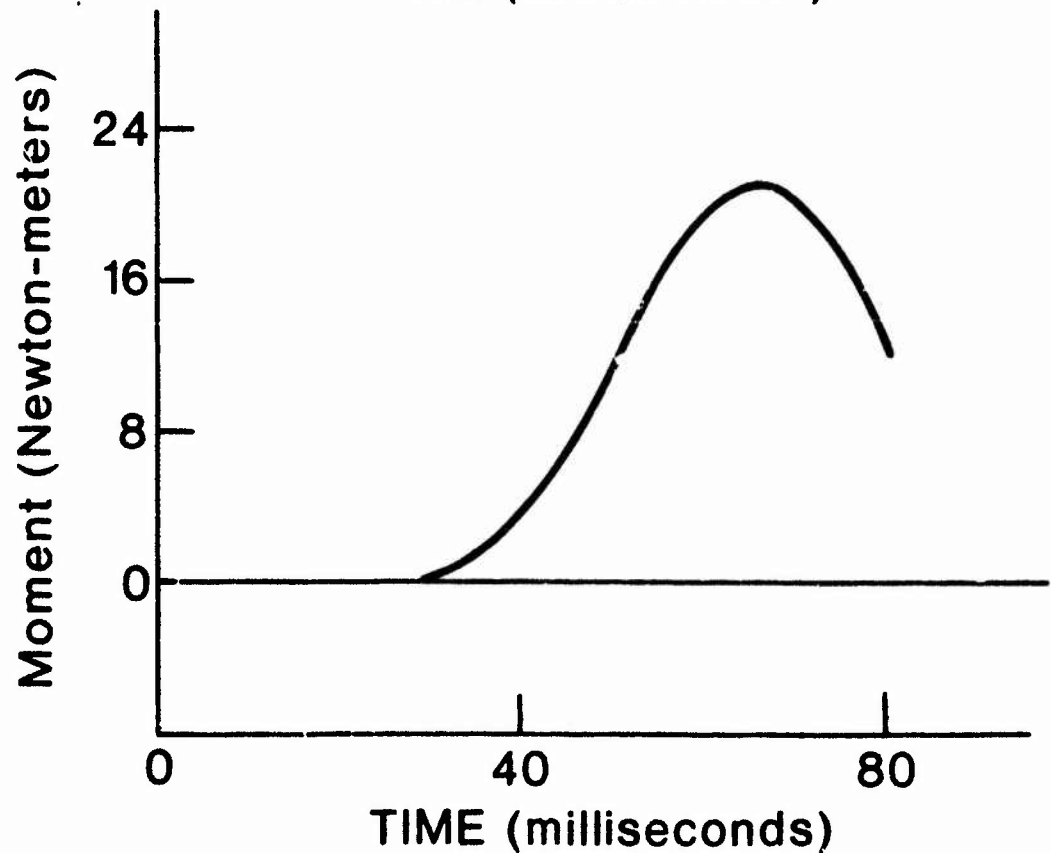
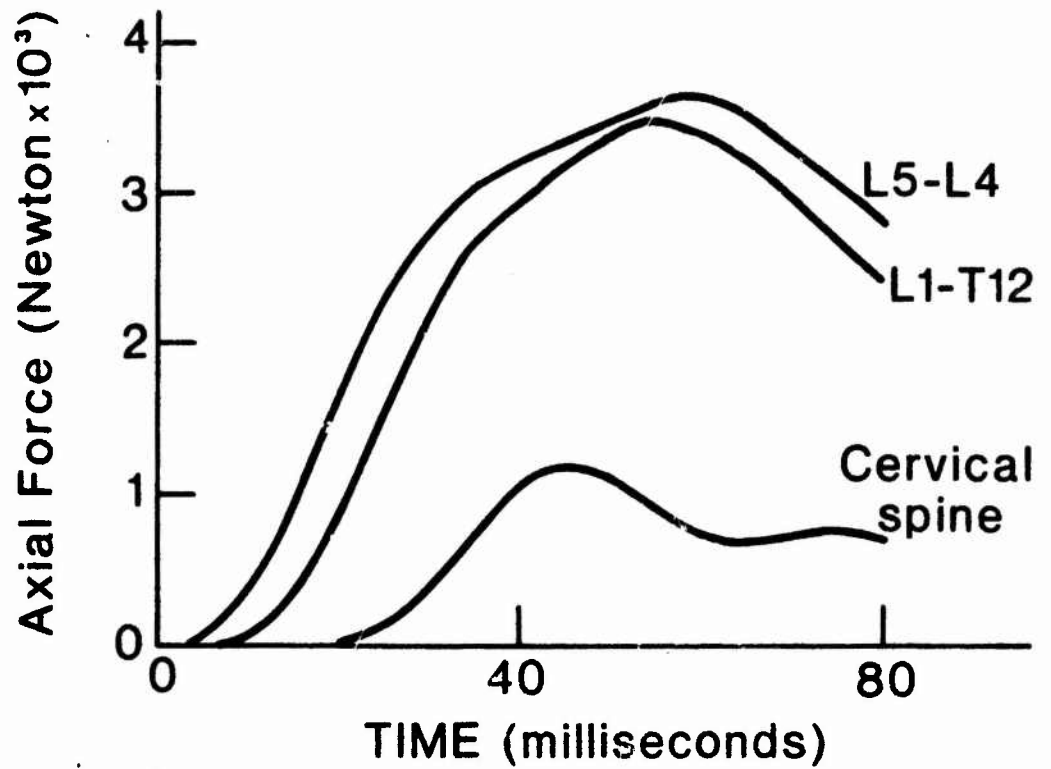


Figure 34. Response of spine to eccentric mass distribution of head.

of the spine. As can be seen from Fig. 34 the axial behavior clearly demonstrates the progression of a compressive wave up the spine at about 30m/sec. This value of axial wave speed in the spine is in good agreement with the values reported by Hess and Lombard (1957) and Li, et al (1970). The peak compressive forces occur earlier in the upper levels of the spine, due to the reflected expansion wave which moves down from the head cancelling, in part, the upward moving compressive wave. Figure 34 shows the cervical moment in the frontal plane due to the eccentric loading. This moment vanishes until the compressive wave has reflected from the head; after reflection, a frontal plane moment is generated in the cervical spine. This moment attains its maximum at about 65 msec, which is considerably later than when the peaks in compressive forces are reached.

In the cervical spine, the intervertebral discs have very little bending stiffness, whereas the articular facets have large moment arms about the sagittal plane. Hence, the forces in the facets can be estimated neglecting the intervertebral disc moments by ascribing the moment to a difference of the vertical forces in a facet pair. This calculation indicates that the peak, compressive facet force is on the same side as the eccentric mass and that its magnitude is about 10^3 Newtons, which is on the order of two to three times the facet force without an eccentric head mass.

2. Complete Spine Model

The studies reported in this Section were conducted with the more complex model of the spine described as Model II in the previous chapter. With the exception of the last study, the seat-back and restraints were included in all studies and the models were driven by prescribing the acceleration of the ejection seat to be $10G_z$, with a rate of onset of 714g/sec over the first 14 msec to the maximum acceleration. The large bandwidth of this model requires that the explicit integration technique be used. A time increment of 10^{-4} was sufficient for stability in energy.

Response of Rib Cage Model Under $10G_z$. In the first study, the response of the rib cage model without any viscera was studied under a vertical $10G_z$ acceleration. Deformed configurations at 20, 40, 60, and 80 msec are shown in Fig. 35. As can be seen, the entire rib cage collapses around the spinal column. There are essentially two mechanisms that prevent the collapse of the rib cage:

- i. the action of the musculature;
- ii. the interaction of the viscera and rib cage; as the viscera are compressed they subject vertical forces on the diaphragm which supports the rib cage.

Although no attempt was made to represent the complex interactions of the musculature, consideration of the second mechanism led to the development of the previously described multi-element viscera model. As the results in the following section show, by

10 G EJECTION SIMULATION WITHOUT VISCERA

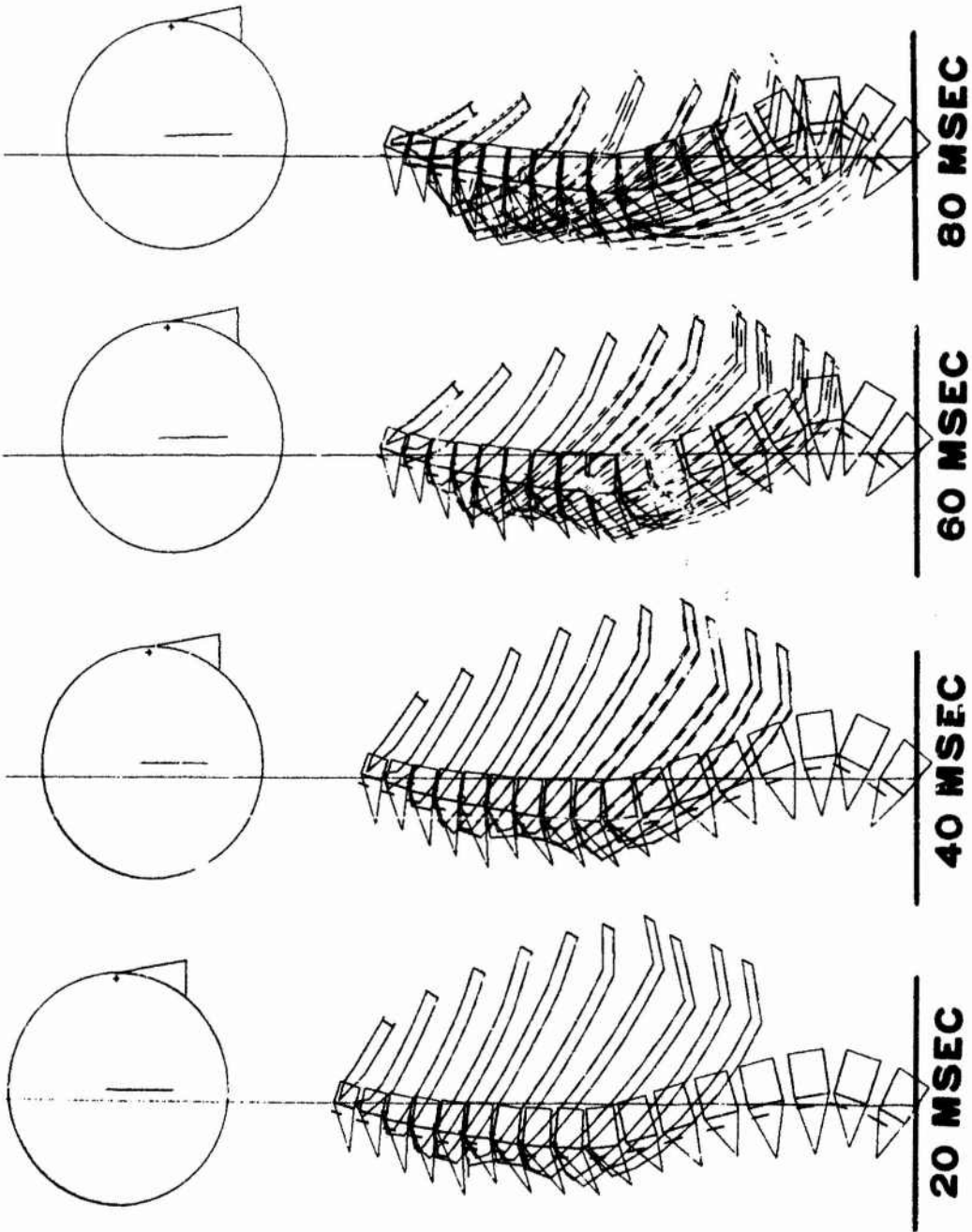


Figure 35. Response of complex model without viscera to 10G_z.

including a representation of the viscera the collapse of the rib cage was prevented.

Response of Complete Model Under $10G_z$. This study was made to determine the response of the combined rib cage and viscera models under $+G_z$ acceleration. Figure 36 depicts the deformed configurations of the model at 20, 40, 60, and 80 msec. This figure also illustrates that the collapse of the rib cage described previously is prevented by incorporating the viscera into the model.

More importantly, spinal response is altered by the inclusion of the rib cage and viscera. A comparison of maximum lumbar forces for the complete model and the isolated spine (Table 15), shows an overall reduction in force levels. Experiments by Tennyson and King (1974), in which eviscerated cadavers were subjected to $+G_z$ acceleration both with and without the abdominal cavity pressurized, show a reduction in axial force levels in the disc and articular facets for the lumbar region when the abdominal cavity was pressurized. In particular, the axial force levels are reduced by about 12% to 23% which compares with the 10% to 25% reduction reported in the experiments. The sensitivity of the axial force reductions to the value of the bulk modulus of the viscera elements was also considered; decreasing the modulus by a factor of four (1×10^6 dynes/cm²) resulted in a 5% to 12% reduction in force levels, while increasing the modulus by a factor of four (1.6×10^7 dynes/cm²) reduced the axial forces by 20% to 35%.

The maximum internal pressures of the viscera model ranged from 5.8×10^5 dyne/cm² in the lower elements to 2.5×10^5 dyne/cm² for

10 G EJECTION SIMULATION WITH PVP VISCERA MODEL

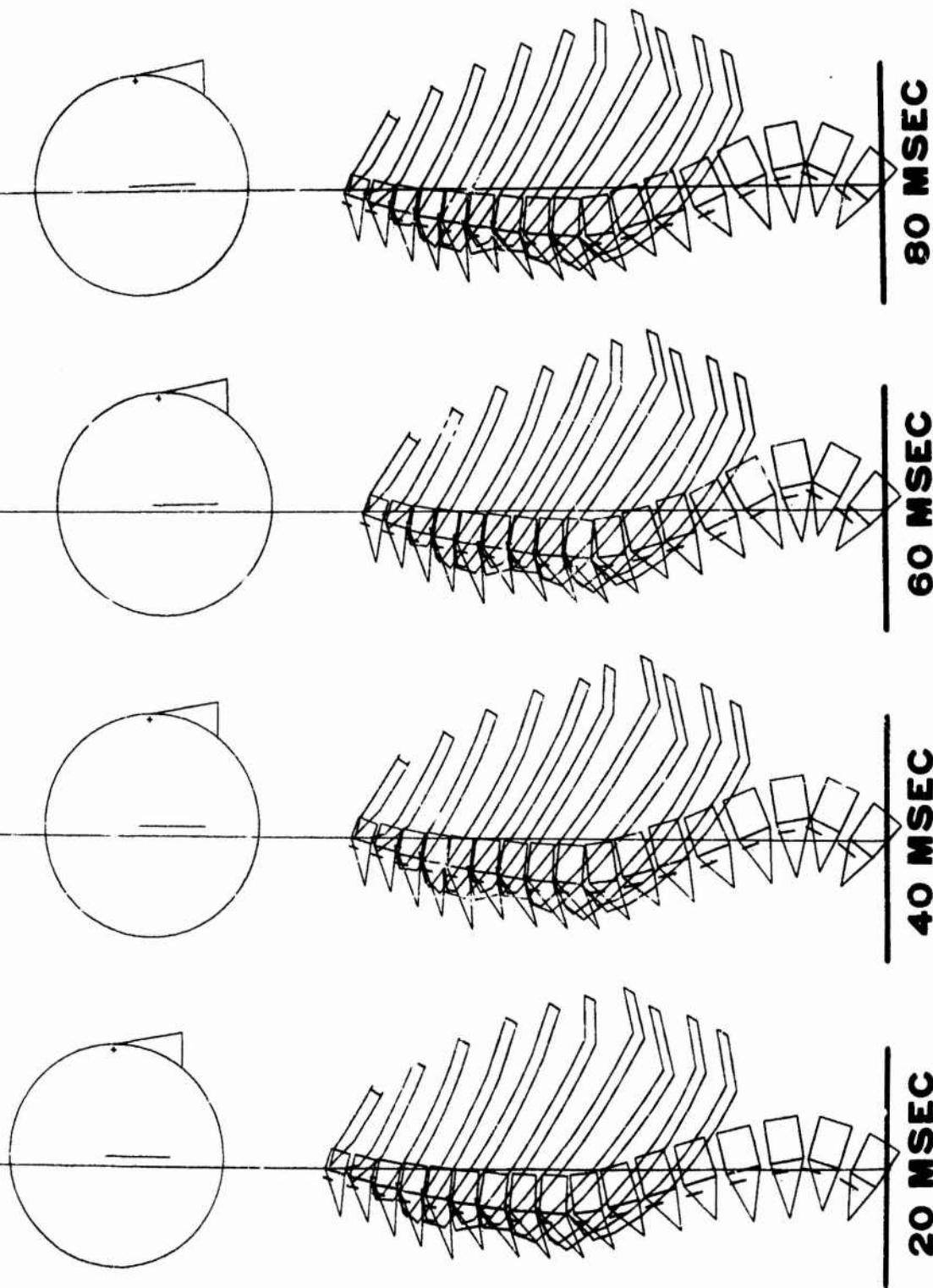


Figure 36. Response of complete model to 10G_z.

Table 15. Effect of Rib Cage and Viscera on Response
of Spine Under $10G_z$

Disc Level	Axial Force 10^3 Newtons		Moment Newton-Meter		Facet Force Newtons	
	Complete Model	Isolated Model	Complete Model	Isolated Model	Complete Model	Isolated Model
L5-L4	-3.27	-4.27	8.48	9.40	-14.9	23.7
L4-L3	-3.29	-4.24	11.53	11.19	65.2	63.2
L3-L2	-3.19	-4.03	10.28	11.11	79.6	74.7
L2-L1	-3.05	-3.68	8.71	9.56	77.5	80.9
L1-T12	-2.91	-3.32	6.43	-11.11	30.5	36.9
T5-T4	-1.83	-1.97	-5.66	6.57	-9.8	28.7
T4-T3	-1.37	-1.58	1.22	7.73	62.4	32.6
T3-T2	-1.53	-1.36	1.77	2.06	30.6	38.6
T2-T1	-1.24	-1.30	2.53	-2.63	20.7	6.2

the upper visceral elements. These values of internal pressure are substantially higher than the 1.4×10^5 dyne/cm² value used for pressurization in the Tennyson and King experiments, or the pressures of 2×10^5 dyne/cm² reported by Morris, et al (1961) in static measurements during weight lifting experiments. However, it is felt that this range of visceral pressure is not unrealistic. Using the counterpart of Eq. (4.5) and the data employed to obtain this wave speed, the maximum stresses in the abdominal wall are computed to be 5.8×10^6 dyne/cm² (84 psi). These stresses could be confined by the musculature and the tissues alone, for the strength of these tissues is on the order of 10^8 dyne/cm². The resulting expansion of the cavity would be 0.1 cm, which is probably undetectable.

The addition of the torso to the model reduced the bending moments in the thoracic spine. Thus, although the abdominal cavity-viscera model has almost no inherent bending stiffness, the overall effect of this additional column is to stiffen the model in bending. This behavior is also reflected in the acceleration of the head. The maximum acceleration is 19.6g, which is slightly higher than that of the isolated column for the same conditions.

Response of the Rib Cage Model During Frontal Impact. To illustrate another application for the dynamic response spine model, a simulation of frontal impact, as would occur in an automobile impacting a barrier, was conducted. The spinal model including head, pelvis, legs and rib cage was given an initial velocity of

1.34×10^3 cm/sec (30 mph) in the anterior direction, with the pelvis subjected to a 6.7×10^4 cm/sec² (68.3g) posterior deceleration for 20 msec. The deceleration pulse was a step function with a decreasing ramp at the end of the pulse, the magnitude of the deceleration corresponds to an experimental measurement of a 30 mph crash.

Displacement of the pelvis was prescribed to be consistent with the initial velocity and deceleration, such that the displacement from the initiation of the deceleration to 20 msec was 13.42 cm. The pelvis was constrained from rotation in the sagittal plane to simulate the effect of a lap belt restraint, although the elasticity of the restraint belt was not included in this simulation.

The head displaced 52.85 cm anteriorly at 40 msec and was subjected to 1.63×10^4 cm/sec² (16.65g) peak acceleration, also at 40 msec. An axial expansion wave travels up the spine at about 30 m/sec which is the same wave speed calculated for the compressive wave in the ejection simulations. Peak tensile axial forces in the intervertebral disc ranged from 6.84×10^8 dynes at the sacrum L5 level to 7.82×10^8 dynes at T11-T10 to 4.165×10^8 dynes at the T3-T2 level. Figure 37 shows the spinal configurations initially and at 20 and 40 msec. The exaggerated position of the upper torso at 40 msec is due to the fact that no shoulder harness restraint was included in the simulation and the possible interaction of the thoracic cavity with the steering column was not considered. It also appears that the stiffness of the ribs against rotation is too low.

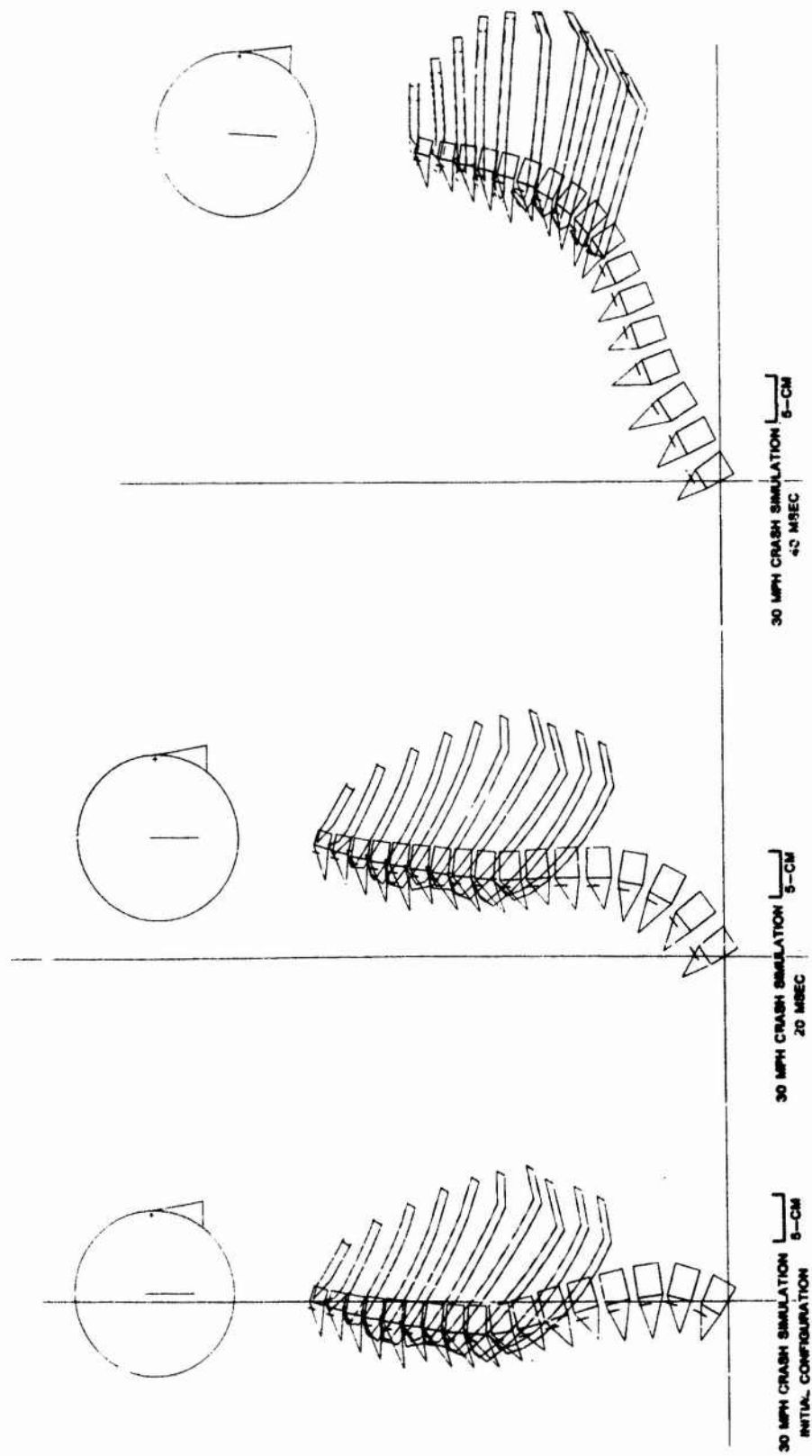


Figure 37. Frontal impact deformed configurations.

3. Modal Analyses

In order to gain a better understanding of the dynamic response properties of the spine, modal analyses were performed on the ligamentous isolated column. The first set of results in Table 16 gives the lowest 7 natural frequencies of the isolated ligamentous spine, Model I. In the modal analyses, neither the seat nor the harness restraints are included. The spine was constrained from motion in the frontal plane; only motions in the sagittal plane were considered. Material properties that do not account for the preload of the body were used.

As can be seen from the results, the model is characterized by a large number of very low natural frequencies. All of the natural modes associated with these frequencies involve primarily bending deformations of the spine. The lowest natural mode of the system with significant axial deformation is the 7th mode, which has a frequency of 17 cps.

When the harness was included, the natural frequencies shifted as shown. Adding the harness introduces additional frequencies which correspond to the motion of the pilot relative to the seat. The lowest such mode is vertical, for the harness exerts little vertical constraint. The fourth frequency, 5.62 cps, agrees reasonably with resonance peaks found in the driving seat impedance measurements by Vogt, et al (1968). However, the bending frequencies seem to be sensitive to the nature of the model, so it is not clear that this correlation is definitive.

In order to investigate these results further, the following

Table 16. Natural Frequencies of Spine Models

Sagittal Plane Frequencies

	Model I		Prasad-King Model	
	Without Harness	With Harness	Without Head or Hips	
1	1.28	0.31	3.66	1.38
2	3.14	1.78	8.17	4.48
3	5.99	2.35	13.01	7.70
4	9.94	5.62	17.70	11.74
5	13.31	10.25	22.21	14.69
6	16.71	13.08	26.92	23.30
7	18.45	14.73	30.90	26.45

Axial Frequencies

	Model I		Prasad-King Model	
	With Head and Hips	Without Head or Hips		
1	17.09	30.12		19.41
2	32.31	61.02		39.29
3	51.29	87.08		80.61
4	77.22	114.87		113.18
5	100.74	142.42		148.81
6	124.89	167.41		179.48

additional modal analyses were made

- i. axial analyses in which the model was constrained from all displacements other than axial;
- ii. analyses of the spine without head or hips;
- iii. corresponding analyses on the Prasad-King (1974) model.

The last analyses was performed to insure that the low frequency response was not an idiosyncrasy of our model. The Prasad-King model is somewhat stiffer, for evidently the preload is included in the material properties. However, the differences are quantitative rather than qualitative: the Prasad-King model low frequency content is also entirely flexural, and the axial mode frequency is even higher. It becomes clear from these results that contrary to widespread notions, the axial mode is never near 10 cps, and in fact hand calculations show that such axial frequencies are almost impossible. Evidently, the peaks in the impedance curves found in axial harmonic oscillations of the human body are due to the parametric excitation of bending modes in the spine. This hypothesis will be explored further.

4. Cervical Spine Model

The simulations reported in this section were conducted with the detailed model of the cervical spine described in Chapter IV. Additional beam elements which act only in bending and interconnect the primary nodes were included in the cervical spine. These were added to represent the stiffness of the cervical musculature; without them it was found impossible to maintain stability of the

cervical spine.

Because of the high stiffness of the facet models, including the cervical region in the model reduces the stability limit of the explicit integration procedure by an order of magnitude. Explicit integration would therefore require 8000 time steps for an 80 msec simulation. Because of the small bandwidth of this model, implicit integration was quite suitable. A time step of 5×10^{-4} seconds was used, and 160 time steps were needed for a 80 msec simulation. Although the implicit procedure increases the stability limit, it is not well-suited for contact problems, such as the seatback interaction. Thus a modified seatback, which restricted both posterior and anterior sagittal plane motion was used. In all cases ejection acceleration was prescribed as $10G_z$, with an onset rate of 714 g/sec over the first 14 msec to the maximum acceleration.

Symmetric Head Loading

Comparison of Detailed and Simple Cervical Spine Models. The simple model of the cervical spine consists of a single beam element which connects the top of T1 to the head mass. In both the detailed and simple models the head mass is the same but the detailed model includes the inertia of the cervical spine at each vertebral level. A comparison of maximum force levels in the upper thoracic region predicted by the two models shows an increase in axial forces and a reduction in sagittal moments of the intervertebral disc for the detailed model. The increase in axial loads can be attributed to the additional inertia load of

the cervical vertebrae, however the change in sagittal moments could not be explained. This reduction in bending response also results in an overall reduction of articular facet forces in the detailed model.

Compressive axial forces in the cervical region ranged from 1900 Newtons at C7 to 1000 Newtons at C2 whereas the single beam element in the simple model has a maximum of 1000 Newtons since only the inertia of the head was included. Sagittal plane moments in the cervical region are distributed between the intervertebral discs and the added beams which model the musculature with the added beams generally having twice the disc moment. Both the disc and added beams have comparatively large moments at the bottom and top of the cervical region, while the largest facet forces occur in the center.

Increased Head Loading. This study was made to evaluate the response of the cervical spine when a 0.9 kg mass is added to the center of gravity of the head mass. The cervical force levels with the added mass are significantly greater. Axial disc forces increased 14% at C2 to 6.7% at T1 and sagittal plane moments averaged a 6% increase with a corresponding average increase of 10% in articular facet forces. Hence increasing the inertial load of the head by 14% results in an almost equal redistribution of the added load in the axial component of the disc and the articular facets.

In both of these simulations the head mass displaced about 0.5 cm in the posterior direction as a result of locating the

Table 17. Cervical Forces with Increased Head Mass

Disc Level	Axial Force 10^3 Newtons		Moment Newton-Meters		Facet Force Newtons	
	5.6 Kg Head Mass	6.5 Kg Head Mass	5.6 Kg Head Mass	6.5 Kg Head Mass	5.6 Kg Head Mass	6.5 Kg Head Mass
C3-C2	-1.19	-1.36	-2.00	-2.29	-72.5	-80.3
C4-C3	-1.31	-1.45	-1.10	-1.17	-69.3	-76.4
C5-C4	-1.48	-1.62	-0.29	-0.31	-103.5	-115.3
C6-C5	-1.69	-1.83	0.85	0.76	-96.5	-106.9
C7-C6	-1.97	-2.12	2.09	2.22	-52.8	-59.9

center of mass slightly posterior to the line of action of the cervical elements. This position of the head mass was chosen to insure that the head would contact the seatback. An anterior motion of the head can be simulated by shifting the location of the head mass forward. However this would require a provision for possible chin-chest contact.

Eccentric Head Loading. In this study, the 0.9 kg mass was placed 10.16 cm directly to the left of the head mass center of gravity. This results in a 1.41 cm shift in the center of gravity of the entire head mass to the left of the sagittal plane. Comparing the results for eccentric and symmetric added mass shows almost no change in the intervertebral disc forces with the exception of frontal plane moments. However, as expected significant frontal plane moments appear when the head mass is eccentric.

Of particular interest are the changes in the articular facet load distributions. The largest changes occur in the upper three facet levels, C3-C2, C4-C3, and C5-C4, where the facet forces on the same side as the eccentric mass are increased an average of 37%, while the right side facet forces are decreased by about 20%. The lower two facet pairs, C6-C5 and C7-C6, exhibit a reversal in load distribution with the left side facet loads decreasing by 11% and the right side facet loads increasing by about 5%. This redistribution of facet loads combined with the frontal plane moments in the intervertebral disc enable the cervical spine to carry almost all of the moment due to the eccentric head mass. Time histories comparing the eccentric and symmetric

case are shown in Figs. 38 to 42.

In the above results, the added beams had no frontal plane stiffness. When frontal plane bending stiffness is included in these beams, part of the frontal plane moment due to the eccentric head mass is carried in these elements. In this case all of the facet loads on the side of the eccentric mass are increased by about 20%. The right side facet loads were decreased from 24% at C3-C2 to no change at C7-C6. Generally by including the frontal plane bending in the additional beams both the disc moments and facet loads are decreased.

A comparison of the simple cervical spine model with the detailed model shows the lateral displacement of the head is 0.44 cm for the simple model and 0.52 cm for the detailed model at 80 msec. Also the frontal plane moment in the simple model is an order of magnitude greater than frontal plane moments predicted by the detailed model. Thus ascribing all of the frontal plane moment to the articular facets, as was done in the first section of results for eccentric head loading, leads to an exaggerated estimate of the facet loads. Maximum head accelerations were 18.9 for the simple model and 20.4G for the detailed model which are similar to the results for the symmetric head loading. Frontal and lateral views of the eccentrically loaded detailed model at 80 msec are shown in Figs. 43 and 44.

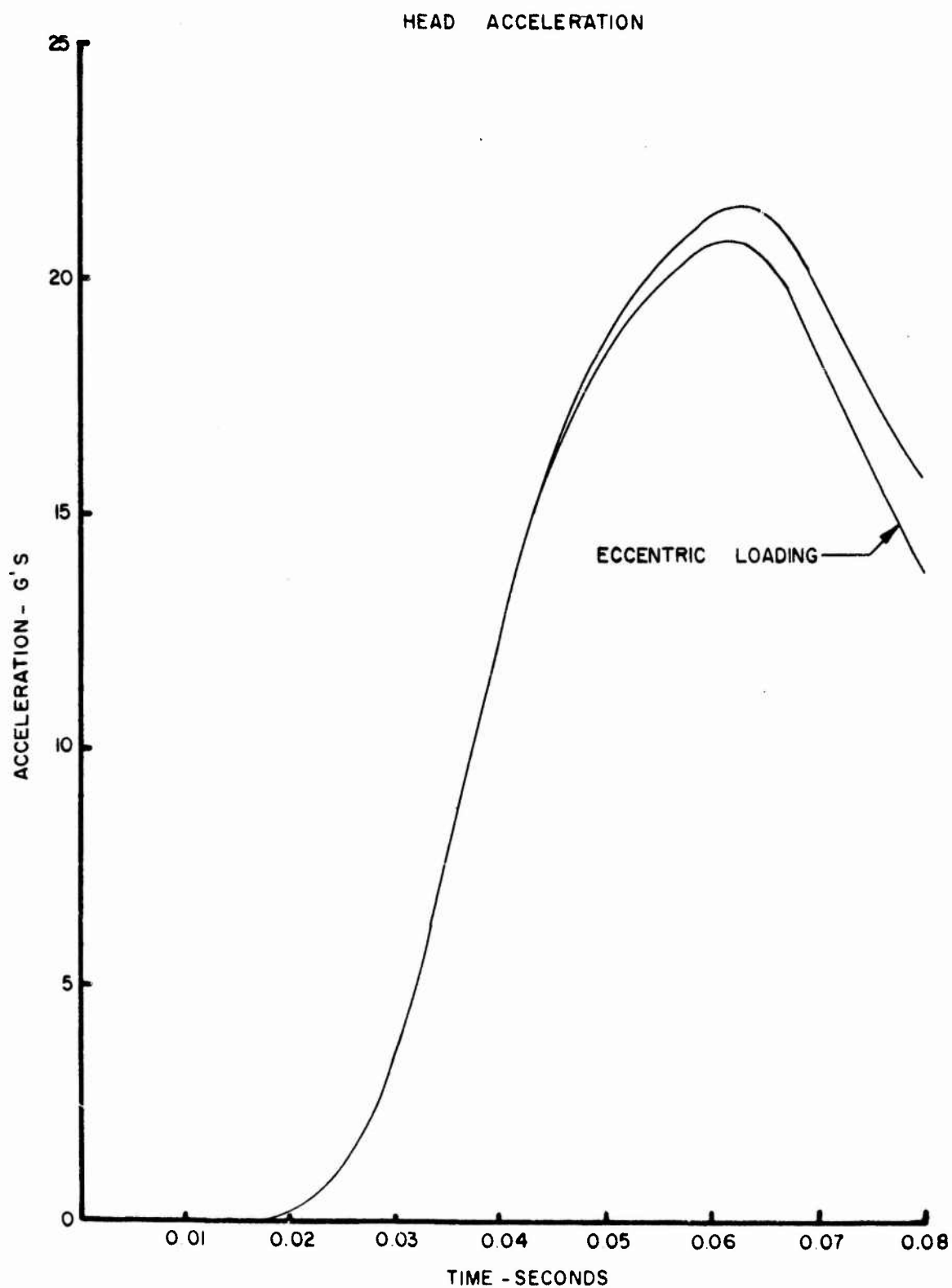


Figure 38. Comparison of head acceleration for symmetric and eccentric head mass.

C5 - C4 AXIAL FORCE

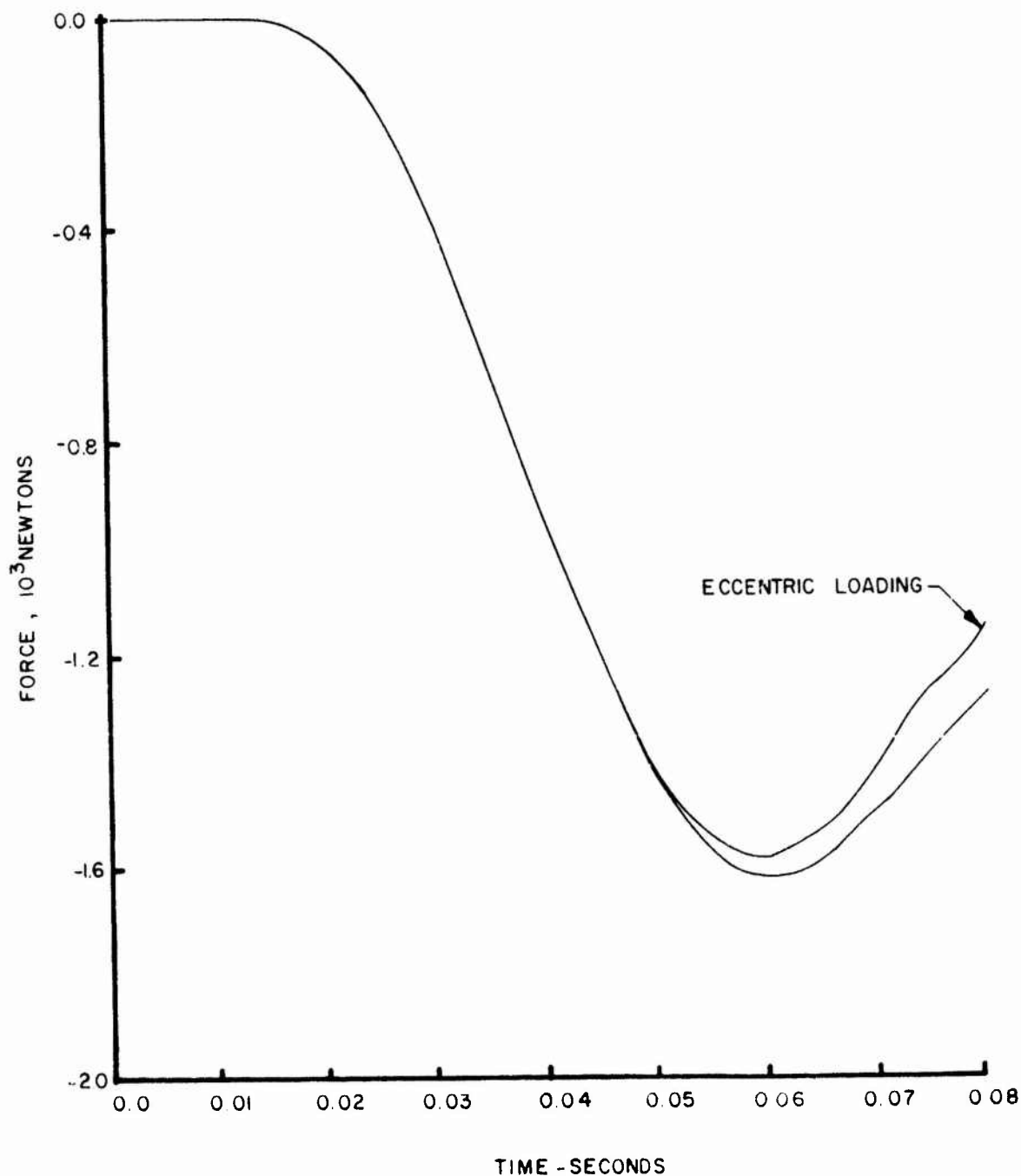


Figure 39. Comparison of C5/C4 axial force for symmetric and eccentric head mass.

C5-C4 SAGITTAL PLANE MOMENT

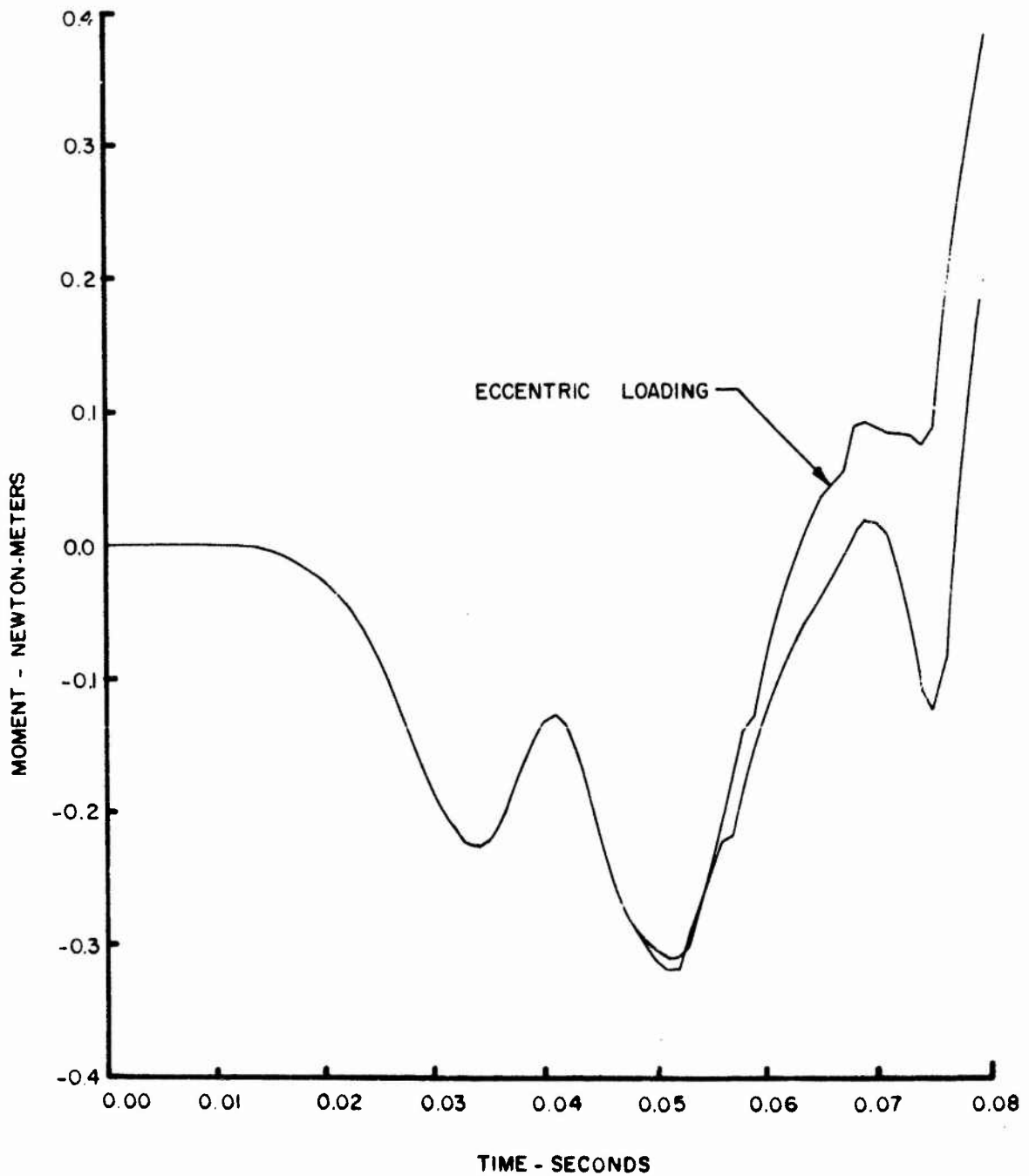


Figure 40. Comparison of C5/C4 sagittal plane moment for symmetric and eccentric head mass.

C5-C4 LEFT FACET FORCE

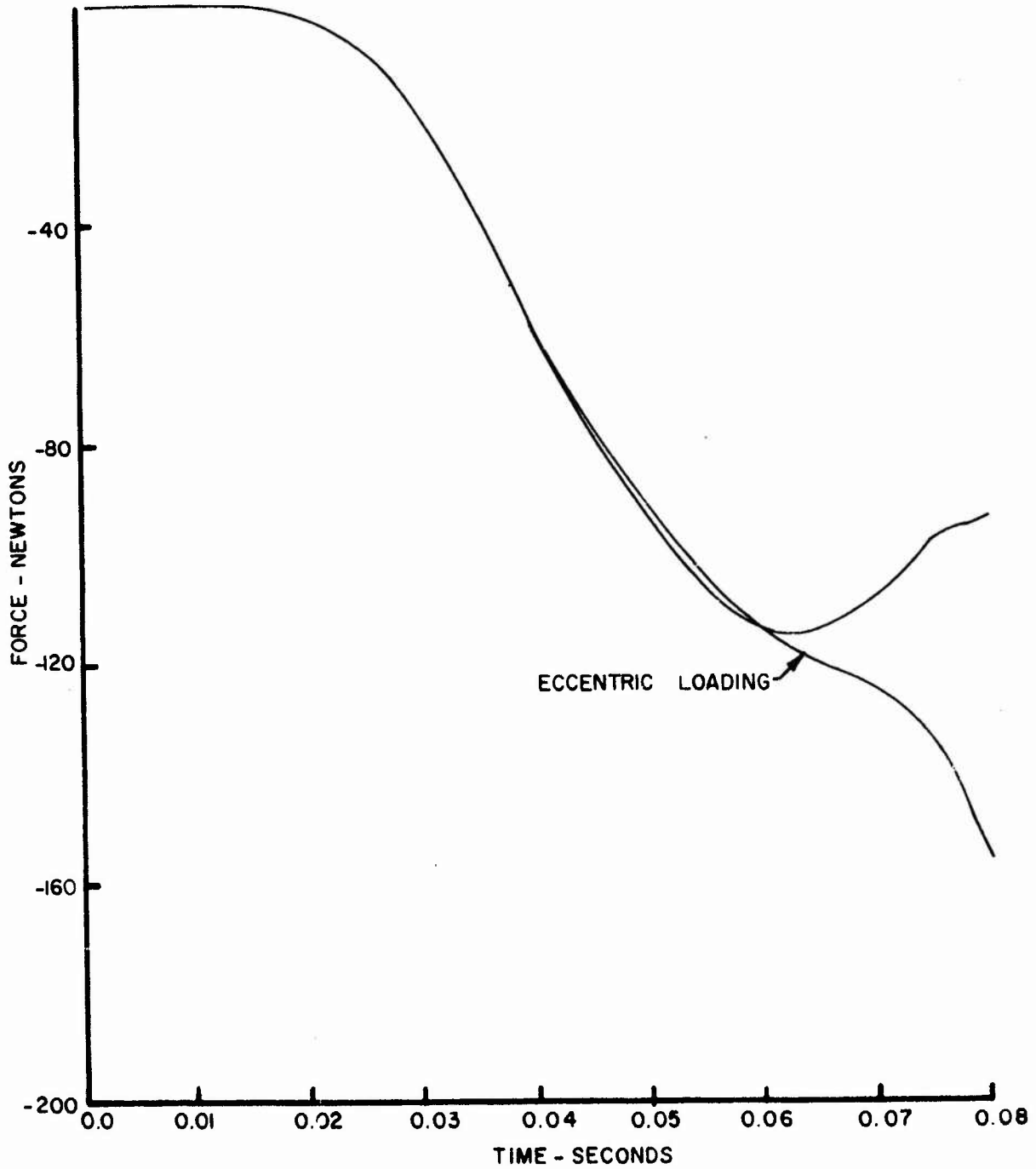


Figure 41. Comparison of C5/C4 left facet force for symmetric and eccentric head mass.

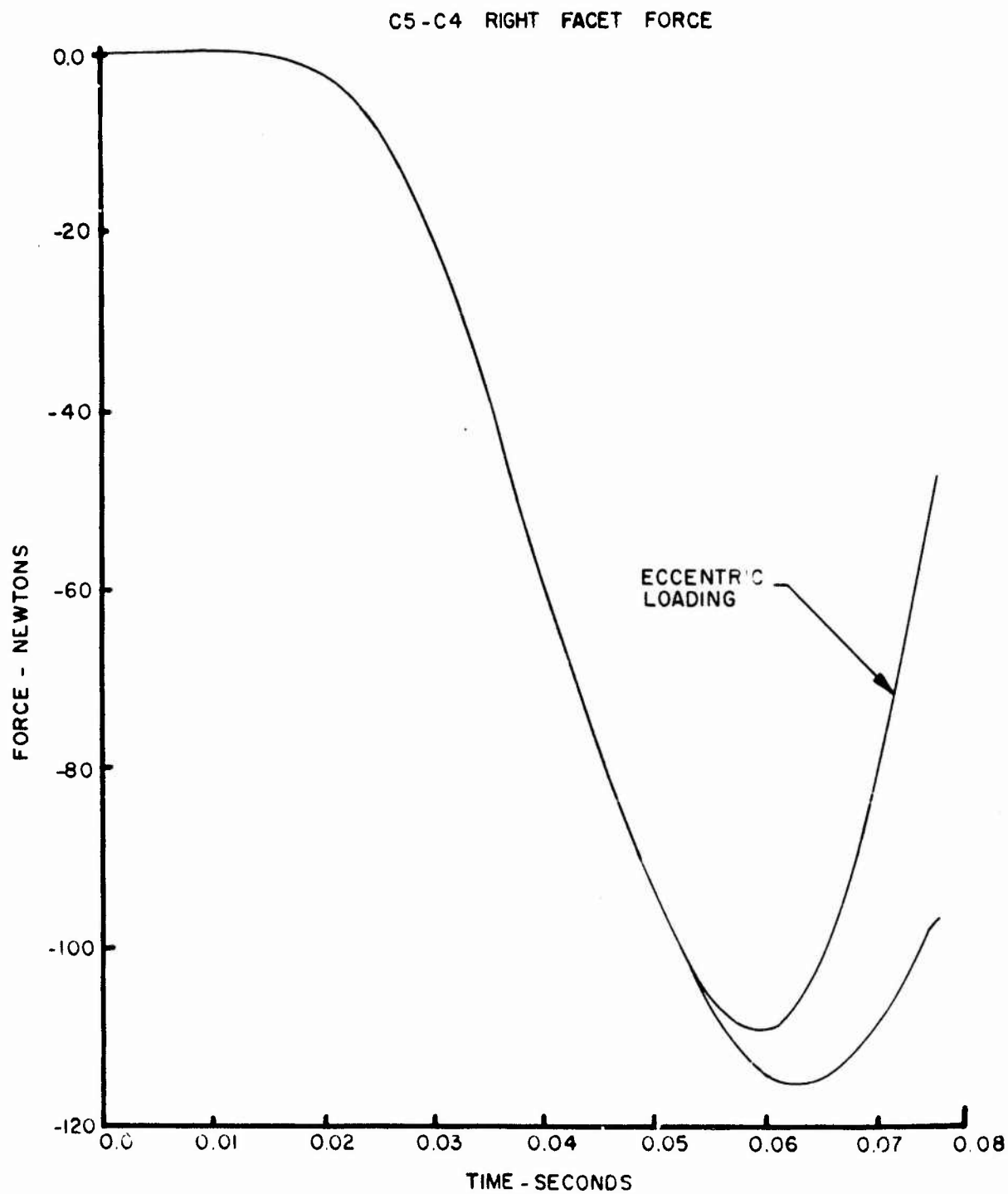


Figure 42. Comparison of C5/C4 right facet force for symmetric and eccentric head mass.

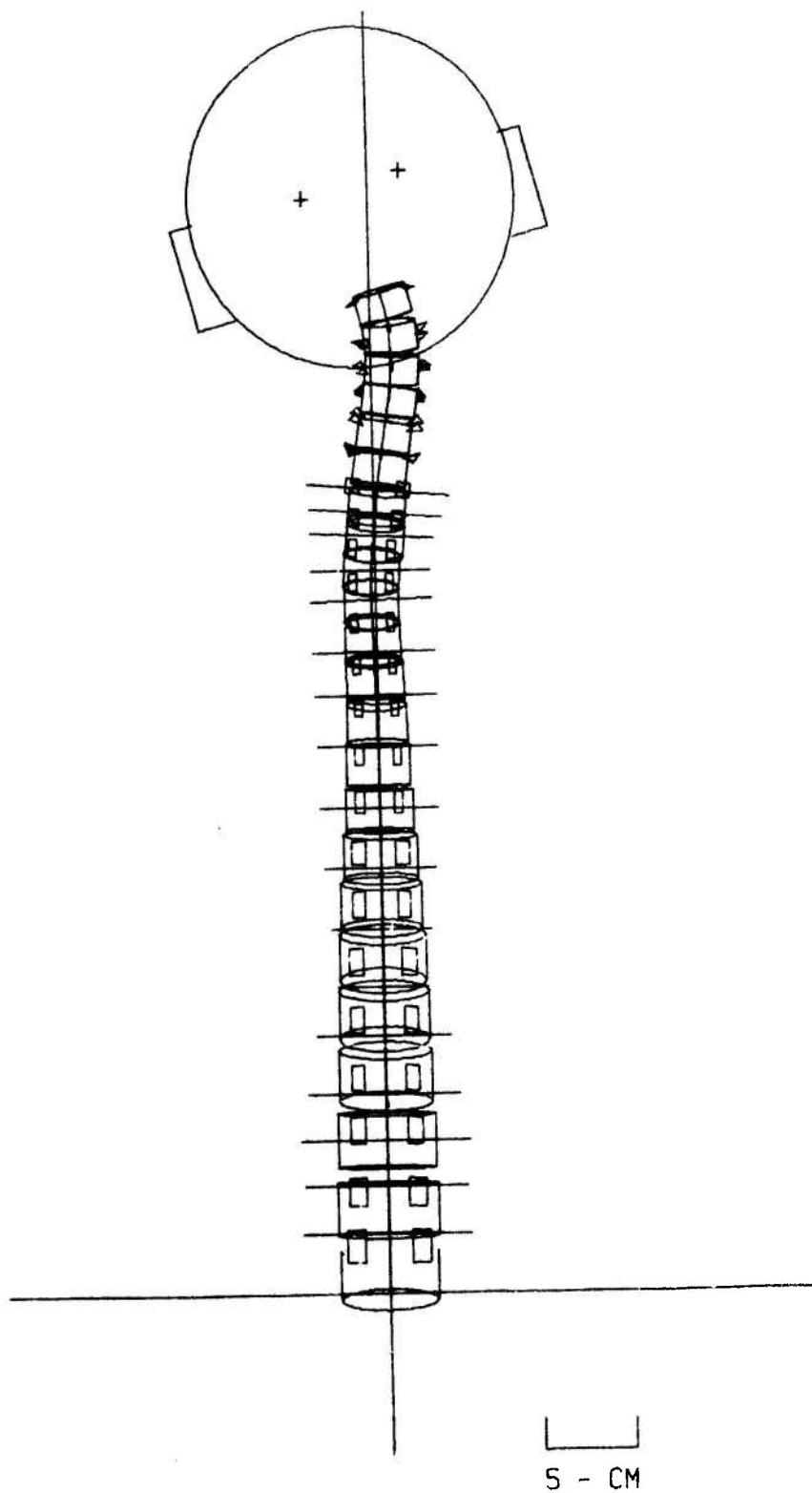


Figure 43. Back view of 80 msec configuration for eccentric head mass.

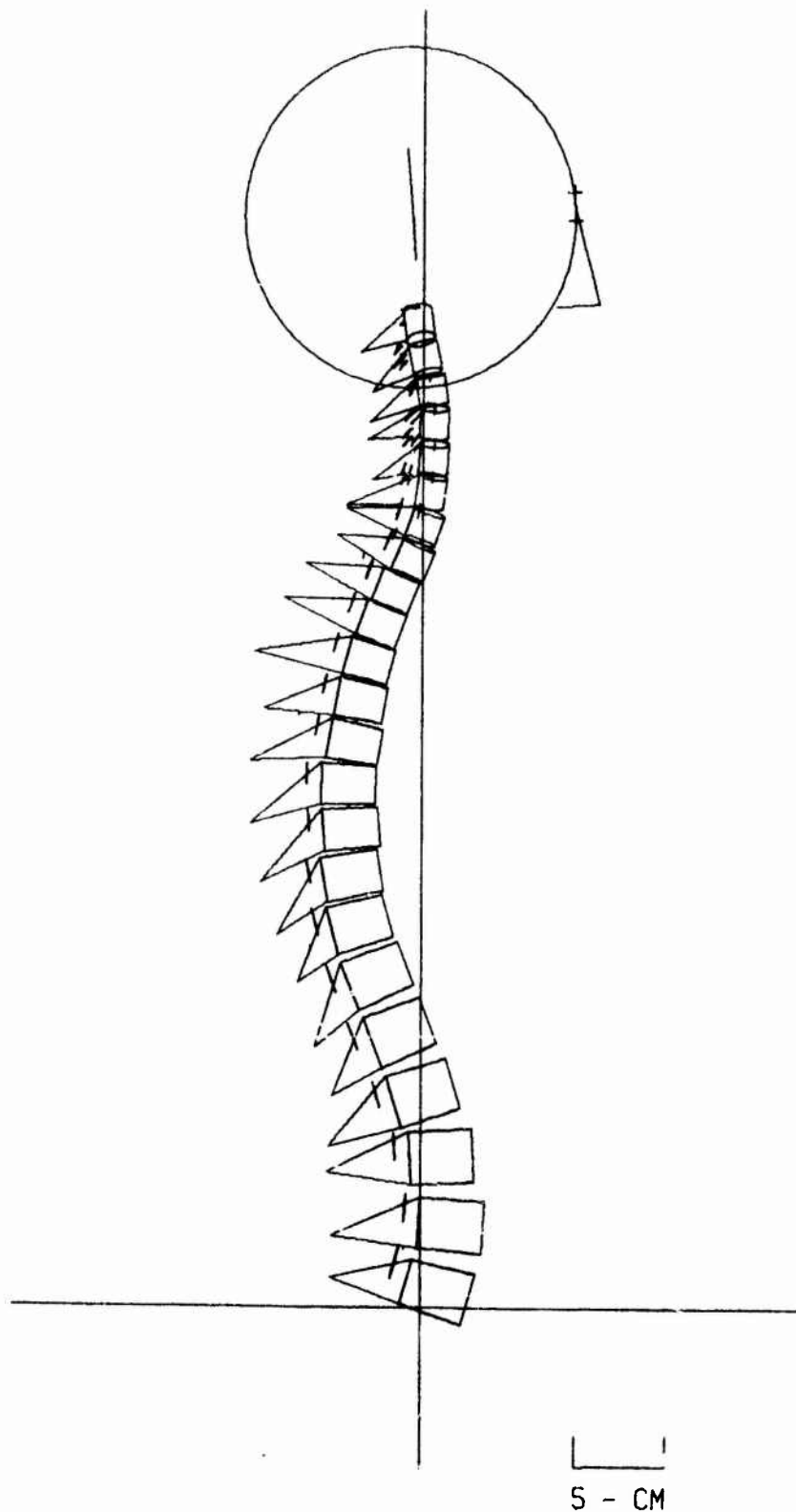


Figure 44. Side view of 80 msec configuration for eccentric head mass.

REFERENCES

- Andriacchi, T., Schultz, A., Belytschko, T. and Galante, J. "A Model for Studies of Mechanical Interactions Between the Human Spine and Rib Cage," J. of Biomechanics 7, 497-507, 1974.
- Bartz, J.A., "Validation of a Three Dimensional Mathematical Model of the Crash Victim," Proc. Symposium on Human Impact Response, Warren, Michigan, 1973.
- Belytschko, T., "Transient Analysis," Structural Mechanics Computer Programs, ed. W. Pilkey, et al., University Press of Virginia, 255-276, 1974.
- Belytschko, T. and Hsieh, B.J., "Nonlinear Transient Finite Element Analysis with Convected Coordinates," Intl. J. of Num. Methods in Eng. 7, 255-271, 1973.
- Belytschko, T. and Schoeberle, D., "On The Unconditional Stability of an Implicit Algorithm for Nonlinear Structural Dynamics," to be published, J. Appl. Mech.
- Brown, T., Hansen, R. and Yorra, A., "Some Mechanical Tests on the Lumbosacral Spine with Particular Reference to the Intervertebral Discs," J. of Bone and Joint Surg. 39A, 1135-1164, 1970.
- Clauser, C., McConville, J. and Young, J., "Weight, Volume and Center of Mass Segments of the Human Body," AMRL-TR-69-70, Wright-Patterson A.F.B., Ohio, 1969.
- Evans, F.G., "Mechanical Properties and Histological Structure of Human Cortical Bone," ASME Paper No. 70-WA/BHF-7, 1970.
- Farfan, H., Cossette, J., Robertson, G., Well, R. and Kraus, H., "The Effects of Torsion on the Lumbar Intervertebral Joints: The Role of Torsion in the Production of Disc Degeneration," J. of Bone and Joint Surg., 49A, 468-497, 1970.
- Gourlay, A.R. and Watson, G.A., Computational Methods for Matrix Equations, John Wiley and Sons, 1973.
- Hess, J.L. and Lombard, C.F., "Theoretical Investigations of Dynamic Response of Man to High Vertical Accelerations," Aviation Medicine, 66-75, 1958.

- Hurty, W.C. and Rubinstein, M.F., Dynamics of Structures, Prentice-Hall, Englewood Cliff, New Jersey, 1964.
- IBM Scientific Subroutine Package, IBM Technical Publications Department, White Plains, New York, 1967.
- Kazarian, L., "Dynamic Response Characteristics of the Human Vertebral Column, An Experimental Study on Human Autopsy Specimens," Acta Orthop. Scand. 146, 1972.
- Kulak, R.F., "A Study of Intervertebral Disc Mechanics by the Finite Element Method," Ph.D. Thesis, University of Illinois at Chicago, 1974.
- Lanier, R., "The Presacral Vertebrae of American White and Negro Males," Amer. J. Physical Anthro. XXV, 341-420, 1939,
- Latham, F., "A Study in Body Ballistics: Seat Ejection," Proc. of Royal Society 147, Series B, 121, 1957.
- Li, T.F., Advani, S.H. and Lee, Y.C., "The Effect of Initial Curvature on the Dynamic Response of the Spine to Axial Accelerations," Symposium on Biomechanical Models and Their Applications, published by Aerospace Medical Research Lab, Wright-Patterson A.F.B., No. AMRL-TR-71-29, 621-648, 1971.
- Liu, Y.K. and Ray, G., "A Finite Element Analysis of Wave Propagation in the Human Spine," Final Report for Contract F33615-72-C-1212, Aerospace Medical Research Laboratory, Wright-Patterson A.F.B., Ohio, 1973.
- Liu, Y.K. and Wickstrom, J.K., "Estimation of the Inertial Property Distribution of the Human Torso from Segmented Cadaveric Data," Perspectives in Biomedical Eng., 1973.
- Lucas, D. and Bresler, B., "Stability of the Ligamentous Spine," Biomechanics Laboratory Report 40, University of California at San Francisco, 1961.
- Marchertas, A.H. and Belytschko, T., "Nonlinear Finite Element Formulation for Transient Analysis of Thin Structures," Argonne National Laboratory Report ANL-8104, Argonne, Illinois, June 1974.
- Markolf, K., "Stiffness and Damping Characteristics of the Thoracolumbar Spine," Bioengineering Approaches to Problems of the Spine, National Institutes of Health, Bethesda, Maryland, 87-143, 1970.

- Moffatt, C.A., Advani, S.H. and Lin, C., "Analytical and Experimental Investigations of Human Spine Flexure," American Society of Mechanical Engineers, Division of Biomechanical and Human Factors, 71-WA/BHF-7, November 1971.
- Morris, J.M., Lucas, D.B. and Bressler, B., "Roles of The Trunk in Stability of the Spine," J. of Bone and Joint Surg., 43A, 1961.
- Nachemson, A., "Lumbar Intradiscal Pressure, Experimental Studies on Post Mortem Material," Acta Orthop. Scand. Suppl. 43, 1960.
- Newmark, N., "A Method of Computation for Structural Dynamics," J. Eng. Mech. Div., Proc. of ASCE, 67-94, 1959.
- Orne, D. and Liu, Y., "A Mathematical Model of Spinal Response to Impact," J. of Biomechanics 4, 49-71, 1970.
- Payne, P.R., "The Dynamics of Human Restraint Systems, Impact Acceleration Stress," National Academy of Sciences, National Research Council, Publication No. 977, Washington, D.C. 1961.
- Payne, P.R., "Some Aspects of Biodynamic Modelling for Aircraft Escape Systems," Proc. Symposium on Biodynamic Models and Appl., Wright-Patterson A.F.B., Ohio, 1972.
- Prasad, P., King, A.I., and Ewing, C.L., "The Role of the Articular Facets During +G_z Acceleration," Bioengineering Division of the American Society of Mechanical Engineers, 73-WAM/Bio-31, November 1973.
- Prasad, P. and King, A.I., "An Experimentally Validated Dynamic Model of the Spine," Trans. ASME, 546-550, 1974.
- Przemieniecki, J.S., Theory of Matrix Structural Analysis, McGraw-Hill, New York, 1968.
- Rolander, S., "Motion of the Lumbar Spine with Special Reference to the Stabilizing Effect of Posterior Fusion," Acta Orthop. Scand. Suppl. 90, 1966.
- Schultz, A., Benson, D. and Hirsch, C., "Force-Deformation Properties of Human Ribs," J. of Biomechanics 7, 303-309, 1974.
- Schultz, A., Benson, D., and Hirsch, C., "Force-Deformation Properties of Human Costo-Sternal and Costo-Vertebral Articulations," J. of Biomechanics 7, 311-318, 1974.
- Schultz, A., Belytschko, T., Andriacchi, T. and Galante, J., "Analog Studies of Forces in the Human Spine: Mechanical Properties and Motion Segment Behavior," J. of Biomechanics 6, 373-383, 1973.

- Schultz, A., Belytschko, T., Andriacchi, T. and Galante, J., "Analog Studies of Forces in the Human Spine: Computational Techniques," J. of Biomechanics 6, 361-371, 1973.
- Tennyson, S.A. and King, A.I., "Effect of Intra-Abdominal Pressure on the Spinal Column During +G_z Accelerations," Advances in Bioengineering, ASME, November 1974.
- Todd, T. and Pyle, S., "A Quantitative Study of the Vertebral Column by Direct and Roentgenoscopic Methods," Amer. J. Physical Anthro. XII, 321-338, 1928.
- Torvik, P.J., "An Analysis of Pressure Wave Generated in Seated Spinal Impact," Symp. on Biodynamic Models and Their Applications, Dayton, Ohio Oct. 1970.
- Toth, R., "Multiplying Degree of Freedom, Nonlinear Spinal Model," Proc of 19th Annual Conference on Engineering in Medicine and Biology 8, 1966.
- Voyt, H., Coermann, R. and Fust, H., "Mechanical Impedance of the Sitting Human Under Sustained Acceleration," Aerospace Medicine 39, 675-679, 1968.
- Weis, E.B. and Mohr, G.C., "Cine-radiographic Analysis of Human Visceral Response to Short Duration Impact," Aerospace Medicine 38, 10, 1967.

APPENDIX I

COMPUTER PROGRAM DESCRIPTION

1. Introduction

The program package developed here consists of two distinct programs: an analysis program for predicting the dynamic response of the human body under prescribed loads or accelerations and a graphics package for depicting deformed and undeformed anatomical configurations.

The techniques employed in the analysis program have been described in Chapters 2 and 3. In the following Sections, the input formats for this program and other information needed for its use are given. The program, in addition to standard printer output, has provisions for Calcomp and printer plot graphical output of time histories of responses such as displacements, velocities, accelerations, forces, stresses and strains.

However, the graphical depictions of the anatomy, such as Figures 6, 7, 8, and 9 are obtained by a separate program, which is described in Sections 12 and 13. The input for this graphics package can be automatically generated by the analysis program in punched card form. In addition, the graphics program can be used independently for other studies.

Both programs were developed on an IBM 370/158 computer system. They are completely written in FORTRAN IV, and with small changes can be run on CDC and UNIVAC computers. For the analysis program, both the running time and required core storage are strongly problem dependent. A minimum of about 320 k bytes (80,000 words) is needed for small problems, while models which include the rib cage and certain implicit models require about 520 k bytes (140,000 words). Running time is 3 to 5 minutes for the simple models, 10 to 20 minutes for the complex models on the IBM 370/158. For the graphics package, about 320 k bytes (80,000 words) of core storage are needed; running time is about 1 to 2 minutes.

The programs were developed as a research tool. An effort has been made to maintain modularity of subroutine functions so that additional features may be added. Care has been taken to insure maximum versatility and usability, but because of the evolutionary character of the development, these programs do not have the ease of input, extensive internal error checks, generalized applicability of user-oriented, general purpose programs.

2. Input Data

Card 1: TITLE CARD (20A4)

<u>Cols.</u>	<u>FORTRAN Name</u>	<u>Description</u>
1-80	TITLE	Any 80 alphanumeric characters to identify the problem; these characters will be printed as a heading to the output.

Card 2: PARAMETER CARD (8I5,E10.6,I5)

1-5	NNODE	Number of nodes in the model (includes primary and secondary nodes, but does not include orientation nodes).
6-10	NPRI	Number of primary nodes in the model.
11-15	NAXOR	Number of axis orientation nodes in the model; these are used to determine the orientation of the local \hat{y} axis of the beam elements (see Section 5).
16-20	NELE	Number of elements in the model.
21-25	NUMMAT	Number of different element section and material types; each group of Card 4 constitutes a section-material type.
26-30	NUMDIS	Number of nodes at which any displacement components are specified either a zero or nonzero value.
31-35	MXSTEP	Number of time steps to be taken.
36-40	NDGREE	Number of degrees of freedom per node (should be six).
41-50	DELT	Time increment.
51-55	NODMAX	Largest node number in model (default value: NODMAX = NNODE + NAXOR).

Card 3: PROGRAM CONTROL CARD (16I5)

1-5	KONTRL(1)	Global or local coordinate option (see Section 9). KONTRL(1) = 0: All nodes are input in global coordinates.
-----	-----------	---

<u>Cols.</u>	<u>FORTRAN Name</u>	<u>Description</u>
		KONTRL(1) = 1: Secondary nodes are input in the local coordinates of the associated primary node (rigid linkage).
6-10	KONTRL(2)	Print option. KONTRL(2) = 0: Print time histories of stress, displacement, etc. KONTRL(2) = 1: Omit printing of time histories.
11-15	KONTRL(3)	Control parameter for initial body axes. KONTRL(3) = 0: Initial orientations (time = 0) of body coordinates b_i of nodal masses are taken to be the principal axes as found by an eigenvalue routine. KONTRL(3) = 1: Initial orientations of body coordinates b_i are coincident with the global coordinates.
16-20	KONTRL(4)	Number of sliding interface planes (see Section 3).
21-25	KONTRL(5)	KONTRL(5)/1000 is the beta parameter in the Newmark β integration (should be zero for explicit integration and 250 for implicit integration).
26-30	KONTRL(6)	(IMPLICIT ONLY) If the number of iterations for the last step is \geq KONTRL(6) then a new stiffness matrix is formulated for the next step, otherwise the previous stiffness matrix is used.
31-35	KONTRL(7)	(IMPLICIT ONLY) Maximum number of iterations per step.
36-40	KONTRL(8)	(IMPLICIT ONLY) EPSLON*1000, energy error criteria.
41-45	KONTRL(9)	(IMPLICIT ONLY) Rotational equations of motion. KONTRL(9) = 0: Angular velocity product terms omitted. KONTRL(9) = 1: Angular velocity product terms included.
46-50	KONTRL(10)	(IMPLICIT ONLY) Geometric stiffness matrix. KONTRL(10) = 0: Omitted. KONTRL(10) = 1: Included.

<u>Cols.</u>	<u>FORTTRAN Name</u>	<u>Description</u>
51-55	KONTRL(11)	Secondary-Primary node identifier (see Card 5 NOCAL DATA CARD). KONTRL(11) = 0: Default node type is secondary node. KONTRL(11) = 1: Default node type is primary node.
56-60	KONTRL(12)	(IMPLICIT ONLY) Modal analysis option. KONTRL(12) = 0: No modal analysis. KONTRL(12) = 1: Modal analysis. KONTRL(12) = 2: Modal analysis with punched card output for plotting mode shapes of spine.
61-65	KONTRL(13)	Damping option. KONTRL(13) = 0: Critical damping KONTRL(13) = 1: Viscous damping
66-70	KONTRL(14)	Not used.
71-75	KONTRL(15)	Program restart option. KONTRL(15) = 0: No action. KONTRL(15) > 0: Step at which all information is written on unit 13 for later restart of problem. KONTRL(15) < 0: Number of seconds left in job when all information is written on unit 13.
76-80	KONTRL(16)	Debugging print option. KONTRL(16) = 0: No action. KONTRL(16) > 0: Step at which current values in all arrays are printed out and execution continues.

Card 4: MATERIAL PROPERTY CARDS (I5,/,6E10.4,/,6E10.4)

Three cards are required per material section. The input format depends on the element for which the data is needed, so choose appropriately from A, B, C, or D.

Card 4A. Material-section property cards for 3-D AXIAL SPRING ELEMENTS.

Card 4A.1

1-5	MTYP	Material type number; the following material properties apply to all elements, JE, with NODE(9,JE) = MTYP. (See Card 6: Element cards.)
-----	------	---

<u>Cols.</u>	<u>FORTTRAN Name</u>	<u>Description</u>
<u>Card 4A.2</u>		
1-10	E(1,MTYP)	Tension or compression cutoff option. E(1,MTYP) < 0: Element has stiffness only in compression. E(1,MTYP) = 0: Element has stiffness in both tension and compression. E(1,MTYP) > 0: Element has stiffness only in tension.
11-20	E(2,MTYP)	Either Young's Modulus or axial stiffness can be specified, see E(7,MTYP) for implementing this option. (See Section 8 for consistent units.)
21-30	E(3,MTYP)	Not used.
31-40	E(4,MTYP)	Slack in spring, expressed as a strain offset (set equal to zero if no slack is desired).
41-50	E(5,MTYP)	Not used.
51-60	E(6,MTYP)	Not used.
<u>Card 4A.3</u>		
1-10	E(7,MTYP)	Cross sectional area. Note: If area is specified as negative, then E(2,MTYP) is the axial stiffness of the spring, i.e. $E(2,MTYP) = AE/L$.
11-20	E(8,MTYP)	Not used.
21-30	E(9,MTYP)	Not used.
31-40	E(10,MTYP)	Not used.
41-50	E(11,MTYP)	Damping factor in fraction of critical damping or fraction of viscous damping for these elements. (see KONTRL(13))
51-60	E(12,MTYP)	Not used.

Card 4B: Material-section property cards for 3-D LINEAR, ELASTIC
RECTANGULAR BEAM ELEMENT

Card 4B.1

1-5	MTYP	Material type number; the following material properties apply to all elements, JE, with NODE(9,JE) = MTYP (see Card 6, Element Cards).
-----	------	--

<u>Cols.</u>	<u>FORTTRAN Name</u>	<u>Description</u>
<u>Card 4B.2</u>		
1-10	E(1,MTYP)	Density (see Section 8 for consistent units).
11-20	E(2,MTYP)	Elastic modulus.
21-30	E(3,MTYP)	Not used.
31-40	E(4,MTYP)	Not used.
41-50	E(5,MTYP)	Local \hat{z} cross sectional dimension.
51-60	E(6,MTYP)	Poisson's ratio.
<u>Card 4B.3</u>		
1-10	E(7,MTYP)	Cross sectional area.
11-20	E(8,MTYP)	Local \hat{y} cross sectional dimension.
21-30	E(9,MTYP)	Shear deformation parameter in the local \hat{y} direction; set to zero for no shear effects (see Chapter I).
31-40	E(10,MTYP)	Shear deformation parameter in the local \hat{z} direction; set to zero for no shear effects (see Chapter I).
41-50	E(11,MTYP)	Axial damping factor in fraction of critical damping or fraction of viscous damping for these elements. (see KONTRL(13)).
51-60	E(12,MTYP)	Bending damping factor in fraction of critical damping or fraction of viscous damping for these elements. (see KONTRL(13)).

Card 4C: Material-section property cards for 3-D SPINAL DISK BEAM
ELEMENT

Card 4C.1

1-5	MTYP	Material type number, the following material properties apply to all elements, JE, with NODE(9,JE) = MTYP (see Card 6 Element Cards).
-----	------	---

Card 4C.2

1-10	E(1,MTYP)	Axial stiffness (see Section 8 for consistent units).
11-20	E(2,MTYP)	Torsional stiffness.

<u>Cols.</u>	<u>FORTTRAN Name</u>	<u>Description</u>
21-30	E(3,MTYP)	Bending stiffness about the local \hat{y} axis.
31-40	E(4,MTYP)	Bending stiffness about the local \hat{z} axis.
41-50	E(5,MTYP)	Cubic bending stiffness about local \hat{y} axis.
51-60	E(6,MTYP)	Cubic bending stiffness about local \hat{z} axis.

Card 4C.3

1-10	E(7,MTYP)	Not used.
11-20	E(8,MTYP)	Not used.
21-30	E(9,MTYP)	Shear deformation parameter in the local \hat{y} direction; set to zero for no shear effects (see Chapter I).
31-40	E(10,MTYP)	Shear deformation parameter in the local \hat{z} direction; set to zero for no shear effects (see Chapter I).
41-50	E(11,MTYP)	Axial damping factor in fraction of critical damping or fraction of viscous damping for these elements (see KONTRL(13)).
51-60	E(12,MTYP)	Bending damping factor in fraction of critical or fraction of viscous damping for these elements (see KONTRL(13)).

Card 4D: Material-section property cards for PRESSURE VOLUME
PENTAHEDRON ELEMENT

Card 4D.1

1-5	MTYP	Material type number, the following material properties apply to all elements, JE, with NODE(9,JE) = MTYP (see Card 6, Element Cards).
-----	------	--

Card 4D.2

1-10	E(1,MTYP)	Bulk modulus (see Section 8 for consistent units).
11-20	E(2,MTYP)	Not used.
21-30	E(3,MTYP)	Not used.
31-40	E(4,MTYP)	Not used.
41-50	E(5,MTYP)	Not used.
51-60	E(6,MTYP)	Not used.

<u>Cols.</u>	<u>FORTTRAN Name</u>	<u>Description</u>
<u>Card 4D.3</u>		
1-10	E(7,MTYP)	Not used.
11-20	E(8,MTYP)	Not used.
21-30	E(9,MTYP)	Not used.
31-40	E(10,MTYP)	Not used.
41-50	E(11,MTYP)	Not used.
51-60	E(12,MTYP)	Damping factor in fraction of viscous damping for these elements.

Card 5: NODAL DATA CARDS (15,4x,A1,7E10.4)

NNODE and NAXOR cards are required; the orientation nodes must follow all regular nodes.

1-5	N	Node number.
6-10	NODTYP	Secondary-Primary node identifier. NODTYP = S: specifies this node is secondary. NODTYP = P: Specifies this node is primary. (NOTE: This method of node type identification is used along with KONTRL(11) to identify primary nodes whose mass is calculated by the program, i.e. for 3-D rectangular beams.)
11-20	XC(N)	X - coordiante
21-30	YC(N)	Y - coordinate
31-40	ZC(N)	Z - coordinate
41-50	TMASS(1)	Translational mass.
51-60	TMASS(2)	Global \bar{X} moment of inertia, I_{xx}
61-70	TMASS(3)	Global \bar{Y} moment of inertia, I_{yy}
71-90	TMASS(4)	Global \bar{Z} moment of inertia, I_{zz}

(See Section 6 for description of mass lumping at the nodes.)

Card 6: ELEMENT DATA CARDS (15I5)

NELE cards are required.

Card 6A: Element Data Card for 3-D AXIAL SPRING; 3-D LINEAR, ELASTIC RECTANGULAR BEAM; and 3-D SPINAL DISK BEAM ELEMENTS

1-5	M	Element number.
-----	---	-----------------

<u>Cols.</u>	<u>FORTRAN Name</u>	<u>Description</u>
6-10	NODE(1,M)	Node I
11-15	NODE(2,M)	Node J (The local \hat{x} axis is directed from Node I to Node J).
16-20	NODE(3,M)	If node I is not a primary node, the primary node associated with node I (see Section 5).
21-25	NODE(4,M)	If node J is not a primary node, the primary node associated with node J.
26-30	NODE(5,M)	Not used.
31-35	NODE(6,M)	Not used.
36-40	NODE(7,M)	Not used.
41-45	NODE(8,M)	Node K, axis orientation node number to be used in orienting the element local \hat{y} axis; the \hat{y} axis lies in the plane of nodes I, J, and K (see Section 5).
46-50	NODE(9,M)	Material type number; for each material type, a set of material cards must be provided (see Cards 4, Material Property Cards).
51-55	NODE(10,M)	Element type number; indicates whether element M is a spring, elastic beam or disc beam, or pressure volume element. NODE(10,M) = 1: 3-D axial spring. NODE(10,M) = 2: 3-D linear elastic beam. NODE(10,M) = 3: 3-D spinal disk beam. NODE(10,M) = 4: 3-D pressure volume element.
56-60	NODE(11,M)	Not used.
61-65	NODE(12,M)	Not used.
66-70	NODE(13,M)	Not used.
71-75	NODE(14,M)	Not used.

Card 6B: Element Data Cards for PRESSURE VOLUME PENTRAHEDRON ELEMENT

1-5	M	Element number
6-10	NODE(1,M)	Generic node I
11-15	NODE(2,M)	Generic node J
16-20	NODE(3,M)	Generic node K
21-25	NODE(4,M)	Generic node L
26-30	NODE(5,M)	Generic node M
31-35	NODE(6,M)	Generic node N

<u>Cols.</u>	<u>FORTRAN Name</u>	<u>Description</u>
36-40	NODE(7,M)	Primary node associated with generic nodes I-K.
41-45	NODE(8,M)	Primary node associated with generic nodes L-N.
46-50	NODE(9,M)	Material type number; for each material type, a set of material cards must be provided (see Cards 4, Material Property Cards).
51-55	NODE(10,M)	Element type number. NODE(10,M) = 4: Pressure volume pentahedron.
56-60	NODE(11,M)	Not used.
61-65	NODE(12,M)	Not used.
66-70	NODE(13,M)	Not used.
71-75	NODE(14,M)	Not used.

Card 7: PRESCRIBED DISPLACEMENT CARDS (I4,6I1,E10.4)

NUMDIS cards; include only if NUMDIS > 0.

1-4 N Node number at which one or more degrees of freedom are specified.

For each degree of freedom of node N a value of I is specified, where

I =

- 0 indicates no constraint on that degree of freedom.
- 1 indicates that the displacement or rotation component is always zero.
- 2 indicates that the displacement or rotation component is prescribed in SUBROUTINE FREEFD

For each component, a column is provided as follows

5	I	Refers to translational global x degree of freedom of node N.
6	I	Refers to translational global y degree of freedom of node N.
7	I	Refers to translational global z degree of freedom of node N.
8	I	Refers to rotation about body \bar{x} axis degree of freedom.
9	I	Refers to rotation about body \bar{y} axis degree of freedom.

<u>Cols.</u>	<u>FORTRAN Name</u>	<u>Description</u>
10	I	Refers to rotation about body \bar{z} axis degree of freedom.
11-20	ANGLE	Not used.

Card 7A: MODAL ANALYSIS CARD (I4,6I1)

Include only if KONTRL(12) > 0.

1-4	NAXISP	Coordinate axis for printer plots of primary node mode shapes. NAXISP = 1: Mode shapes plotted vs. global x axis. NAXISP = 2: Global y axis. NAXISP = 3: Global z axis.
-----	--------	--

For each of the six degrees of freedom in the entire model a value of I is specified, where

I = 0 indicates this D.O.F. is to be included in the modal analysis.

I = 1 indicates this D.O.F. is to be omitted from the modal analysis.

In addition, individual nodal degrees of freedom may be omitted from the modal analysis by prescribing that D.O.F. to be zero via the prescribed displacement cards (See Card 7).

5	I	Refers to translational global x.
6	I	Refers to translational global y.
7	I	Refers to translational global z.
8	I	Refers to rotation about body \bar{x} .
9	I	Refers to rotation about body \bar{y} .
10	I	Refers to rotation about body \bar{z} .

Card 8: OUTPUT CONTROL CARD (4I10)

1-10	NPFREQ	Frequency of output; whatever output is desired will be printed every NPFREQ steps.
11-20	NPRU	Number of motion output records.
21-30	NPRS	Number of stress output records.
31-40	NPIC	Number of complete (all motion and stress values at one time step) output pictures.

<u>Cols.</u>	<u>FORTRAN Name</u>	<u>Description</u>
<u>Card 9: MOTION OUTPUT CARDS (I10,10x,10A4)</u>		
(NPRU cards; only included if NPRU > 0.)		
1-7	UOUT	Node number.
8	J	Component number of kinematic variable (displacement, velocity or acceleration) to be output. J = 1: Translation in global x direction. J = 2: Translation in global y direction. J = 3: Translation of global z direction. J = 4: Rotation about body \bar{x} axis. J = 5: Rotation about body \bar{y} axis. J = 6: Rotation about body \bar{z} axis.
9	K	Indicates whether record is displacement, velocity, or acceleration. K = 0: Displacement time history. K = 1: Velocity time history. K = 2: Acceleration time history.
10	L	Plot control. L = 0: No plot of time history. L = 1: Calcomp plot of time history. L = 2: Printer plot of time history. L = 3: Both calcomp and printer plot of time history. L = 4: Printer plot and punched cards of time history.
21-60	GLABEL	Alphanumeric information to be printed identifying time history plot.

Card 10: STRESS OUTPUT CARDS (I10,10x,10A4)

(NPRS cards; only included if NPRS > 0.)

1-7	SOUT	Element number
8-9	M	Component number (see Section 11 for organization of STRS array).
10	N	N = 0: No plot. N = 1: Calcomp plot of time history. N = 2: Printer plot of time history.

<u>Cols.</u>	<u>FORTRAN Name</u>	<u>Description</u>
		N = 3: Both Calcomp and printer plot of time history.
		N = 4: Printer plot and punched cards of time history.
21-60	GLABEL	Alphanumeric information to be printed for identifying time history plot.

Card 11: COMPLETE OUTPUT PICTURE CARDS (2I10)

(NPIC cards; only included if NPIC >0.)

1-10	NPOUT	Time step at which complete output picture is desired.
11-20	KON	<p>KON = 1: Output displacements and unit vectors at all nodes having mass (see Section 5).</p> <p>KON = 2: Output above plus coordinates of deformed model (note: output for rotational degrees of freedom is nonsense for this case).</p> <p>KON = 3: Output above plus velocities and accelerations at all nodes having mass.</p> <p>KON = 4: Output above plus all local element forces.</p> <p>KON = 6: Output above plus punched card output of all deformed nodes having mass and associated unit vectors. (Used as input for 3-D plotting program.)</p> <p>KON < 0: Punched card output only.</p>

3. Ejection Seat Geometry Subroutine

The program provides the capability of modelling arbitrary ejection seat geometries. Seat geometry is represented as a collection of piecewise linear planes. Each plane is defined by three points (X_1, X_2, X_3) whose coordinates are given in the global system. The positive normal of the plane is then defined by the right hand rule applied to the sequencing of the points (X_1, X_2, X_3).

In order to prescribe the motion of the plane and incorporate the restraint system, each plane is designated by a primary node. The motion of the primary node is characterized by an acceleration vector. The magnitude of the acceleration vector is given by an acceleration time history which is input through subroutine ICIF (see Section 4). The direction is given by specifying the direction cosines of the acceleration vector. Each primary node which designates a plane may be associated with an arbitrary number of secondary nodes. These secondary nodes can then be used as points of attachment for representing the restraint system with any of the deformable elements available in the program. NOTE: The primary and secondary nodes for this system are input through the Nodal Data Cards (see Card 5), also each primary node must have a Prescribed Displacement Card (see Card 7) with the translational degrees of freedom indicated as prescribed and the rotational degrees of freedom indicated as zero. The deformable elements representing the restraint system are input through the Element Data Cards (see Card 6).

The technique used in the subroutine is to modify the equations of motion for those primary nodes of the model that are in contact with the ejection seat, primary nodes not in contact are not effected. The criteria for contact between a plane and a primary node of the model is that both the relative displacement and acceleration in the normal direction of the plane be decreasing, i.e. the primary node is moving towards the plane.

Input data for subroutine SLIDER; this data is placed after Card 11 of READIN input (Note: data for subroutine ICIF to specify the motion of the planes must follow this data). For each plane (I = 1 to number of planes) the following sequence of five input cards are required:

Card A1: Plane Identification Card (2I5,6E10.0)

<u>Cols.</u>	<u>FORTTRAN Name</u>	<u>Description</u>
1-5	NPNO(1)	Primary node number designating the plane.
6-10	NASN(I)	Total number of primary nodes of the model which may contact plane I.
11-20	DICOS(1,I)	Direction cosine of acceleration vector with respect to the global x-axis.
21-30	DICOS(2,I)	Direction cosine of acceleration vector with respect to the global y-axis.
31-40	DICOS(3,I)	Direction cosine of acceleration vector with respect to the global z-axis.
41-50	SEATK(1,I)	Linear stiffness of elastic plane I.

<u>Cols.</u>	<u>FORTRAN Name</u>	<u>Description</u>
51-60	SEATK(2,I)	Cubic stiffness of elastic plane I.
61-70	VDAMP(I)	Fraction of viscous damping for plane I.

Card A2: Contacting Primary Node Numbers Card (10I5)

1-5	NCP(J,I)	Node number of primary node J which may contact plane I; where J=1 to NASN(I).
-----	----------	--

NOTE: If a consecutive sequence of primary node numbers are associated with a plane, the subroutine will generate the intermediate primary node numbers. The option to generate intermediate primary node numbers is indicated by specifying NASN(I) = 0 on Card A1 and specifying the first and last primary node numbers, NCP(1,I) and NCP(2,I), on Card A2. This sequence must be ascending $NCP(1,I) < NCP(2,I)$.

Card A3: Plane Location Cards (3E10.0)

(3 cards) - for each of the three points (X_1, X_2, X_3) specify

1-10	XI(1)	Global X coordinate of point I.
11-20	XI(2)	Global Y coordinate of point I.
21-30	XI(3)	Global Z coordinate of point I.

4. Subroutine ICIF; Cubic Interpolation Motion Record Subroutine

The program in its present form can treat arbitrary vertical motion input of the hips and seat. The motion input can be specified as either a displacement, velocity or acceleration vs. time curve. For the latter two, the program automatically integrates the record once or twice, respectively, to obtain a displacement history, which is then used to drive the model.

The motion record is specified by an arbitrarily spaced set of points (t_i, f_i, f_i') , $i = 1$ to n , where

- n = is the number of points specified for the motion record.
- t_i = are the times at which the motion function (displacement, velocity, or acceleration) is specified.
- f_i = value of the motion function (displacement, velocity, or acceleration) at time t_i .
- f_i' = value of the derivativeⁱ of the motion function with respect to time at time t_i .

A cubic, continuously differentiable interpolation function is used to approximate the motion record between prescribed points.

SUBROUTINE ICIF (TIME, VALUE, NI)

TIME - Time at which displacement is to be evaluated.
 VALUE - Upon return contains value of displacement.
 NI - Number of integrations to be performed,
 NI = 0, no integration, displacement data was input.
 NI = 1, one integration, velocity data was input.
 NI = 2, two integrations, acceleration data was input.

Input data for subroutine ICIF; this data is placed after Card 11 of READIN input.

Card A1: Initial Parameter Card (I5,5X,2E10.0)

<u>Cols.</u>	<u>FORTRAN Name</u>	<u>Description</u>
1-5	NPTS	Number of points where the motion functions value and derivative are specified, n.
11-20	F1	Integration constant for first integration.
21-30	F2	Integration constant for second integration.

Card A2: Function Specification Cards (3E10.0)

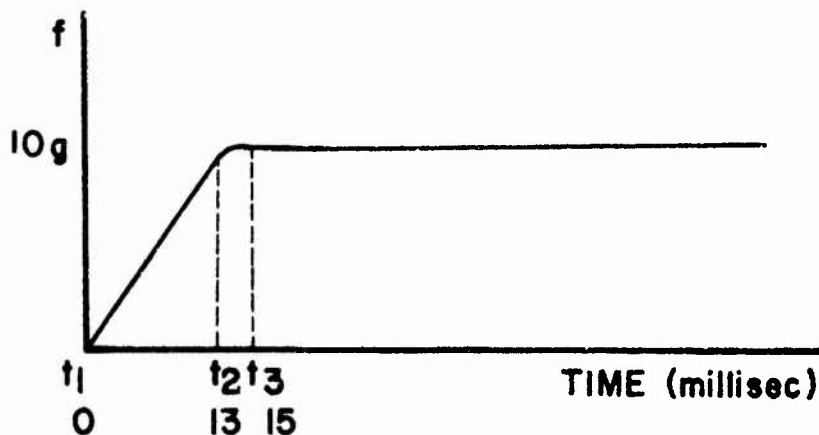
(NPTS Cards) - for each point i specify

1-10	T	Time t_i
11-20	F	Motion function value at time t_i , $f(t_i)$.
21-30	FP	Derivative of function at time t_i , $f'_i(t_i)$.

NOTE: The motion function must start at time zero, $t_1 = 0$.

An example of this data is given below.

Example: 10g Acceleration Record



i	t_i	f_i	f_i'
1	0.0	0.0	7.006×10^5
2	1.3×10^{-3}	9.108×10^3	7.006×10^5
3	15×10^{-3}	9.809×10^3	0.0
4	1.0	9.809×10^3	0.0

5. Primary, Secondary and Axis Orientation Nodes

This program permits the user to construct models with or without rigid linkages between nodes. For this purpose, two types of nodes are used:

Primary nodes - All degrees of freedom are associated with primary nodes. If a primary node is associated with a rigid linkage, it must be at the mass center of the rigid linkage. At most one primary node is allowed per rigid linkage.

Secondary nodes - These nodes connect the ends of deformable elements with rigid linkages; more than one secondary node may be associated with each rigid linkage. A secondary node has no independent degrees of freedom.

If there is no rigid linkage at the endpoint of an element, the endpoint is a primary node.

A third type of node, an axis orientation node, is used to orient the local \hat{y} axis for beam elements.

Axis Orientation node - The two nodes associated with the endpoints of a beam element define the local \hat{x} axis for the beam element. In order to define the local \hat{y} axis for the beam element, a third node is used to define a plane containing both the local \hat{x} and \hat{y} axes. The normal to this plane is the local \hat{z} axis.

6. Mass Lumping

All masses are associated with primary nodes. The mass of a primary node may either (1) be input directly through Cards 5, (2) be generated within the program through lumping the masses of elements or (3) by a combination of these methods (1) and (2).

If method (1) is desired exclusively, the density of all elements on cards 4.1 should be input as zero.

Method (2) can be used by omitting the input of lumped masses and moments of inertia on Cards 4 and inputting mass densities for the elements; the program then lumps half the mass and moments of inertia of each element at the associated nodes.

Method (3) calls for care on the part of the user when rigid linkages are used. The program sums translational masses of each rigid linkage as input through Cards 4 and the lumped masses of elements connected to the primary nodes. It also simply sums the moments of inertia of the primary node and the elements connected to it. It does not shift the center of mass or transform moments to inertia by the parallel axis theorem.

The analyst should also be aware that all independent degrees of freedom are associated with some mass. Any degree of freedom not associated with a mass will automatically be omitted from the equations of motion and so remain fixed throughout the temporal integration.

7. Unit Vectors B1, B2, and B3

The rotational equations of motion for each node (Euler equations) are formulated in a coordinate system that rotates with the node. This coordinate system is initially chosen to coincide with the principal axes of the moment of inertia tensor and remains so throughout the deformation, since it rotates with the mass.

If the principal moments of inertia at a node are about the global x, y, and z coordinates, then initially the unit vectors of the rotational coordinate system coincide with the global coordinates, i.e. B1 is a unit vector in the global x direction, B2 is a unit vector in the global y direction, and B3 is a unit vector in the global z direction. Only the components of two of the unit vectors need be known at any time, i.e. B1 and B3. The third is then given by the cross product $B2 = B3 \times B1$.

8. Consistent Units

It is recommended that the program be used with the following system of units (i.e. all input data should be in these units):

Time : Second (sec.)
Length : Centimeter (cm.)
Mass : Gram (g.)
Force : Dyne (g-cm/sec²)

For the convenience of the user the local element forces and moments are internally converted and also output in the english units:

Length : Inch (in.)
Force : Pound force(lbf.)

However, any consistent system of units may be used for the input data. The resulting output will then be in the same system (and the identifying units will not be germane) with the exception of the english units for forces and moments, which are internally converted.

9. Global or Local Coordinates for Secondary Nodes

Two options are available for the input of the coordinates of secondary nodes:

Global (KONTRL(1) = 0)

All nodal coordinates (primary, secondary, and axis orientation) are input in the global x, y, and z coordinates system.

Local (KONTRL(1) = 1)

The nodal coordinates of the secondary nodes associated with a rigid linkage (primary node) are input in local \hat{x} , \hat{y} , and \hat{z} components of the associated rigid linkage. The local axis origin is the primary node for that rigid linkage.

10. Dynamic Allocation

Core storage among the arrays is allocated internally within the program. This procedure which is called dynamic allocation, requires the user to specify only the dimension of a single array. All vectors and matrices needed for the solution of the problem are then packed sequentially into this array. The size of the array is problem dependent, so that for small problems little core storage is needed. If the dimension specified by the user is not sufficiently large for the problem, an error message is printed along with the total amount of storage needed.

The following are the problem dependent scalar values used to allocate core storage:

Values Obtained Directly from the Input Data

<u>FORTRAN Name</u>	<u>Description</u>
IMODAL	Modal analysis option
MXSTEP	Maximum number of time steps.
NAXOR	Number of axis orientation nodes.
NDGREE	Maximum number of degrees of freedom per node.
NELE	Number of elements
NNODE	Number of primary and secondary nodes in the dataset.
NODMAX	Maximum node number used in the dataset.
NOPT	Number of sliding planes.
NPDIS	Number of degrees of freedom whose motion is prescribed as nonzero.
NPFREQ	Frequency of output; whatever output is desired will be printed every NPFREQ steps.
NPIC	Number of complete output pictures.
NPRI	Number of primary nodes.
NPRS	Number of stress output records.
NPRU	Number of motion output records.
NUMDIS	Number of nodes at which any displacement components are specified either zero or nonzero.
NUMMAT	Number of different element section and material types.

Values Calculated Internally from the Input Data

<u>FORTRAN Name</u>	<u>Description</u>
LBKE=NBE*(MUDE+1) -((MUDE+1)*MUDE)/2	Required storage of the stiffness matrix for modal analysis.
MEQ=NDGREE*NNODE	Maximum number of degrees of freedom in the mesh.
MUD=(MAX(I-J)+1) *NDGREE-1	Number of nonzero upper codiagonals in banded stiffness matrix.
MUDE=NBE-1	Number of nonzero upper codiagonals in banded stiffness matrix for modal analysis.
NBE=NDE*NPRI	Number of degrees of freedom in the mesh for modal analysis.
NDE	Number of degrees of freedom per node for modal analysis (See Card 7A).
NODET=NNODE+NAXOR	Total number of nodes in the mesh (primary and secondary and axis orientation).
NPLOT=NPRU+NPRS	Number of time histories to be plotted.
NPTS=MXSTEP/ NPFREQ+2	Number of points to be plotted for each time history.
N1=NDGREE*NPRI	Number of independent degrees of freedom in the mesh.

The following is a list of the array names and their storage requirements which are dynamically allocated:

<u>FORTRAN Name</u>	<u>Size</u>	<u>Description</u>
A	NPTS	Temporary storage of ordinate values for plotted output.
AL	NELE	Element lengths.
AO	N1	Old nodal accelerations.
AUX	N1	Deformed nodal coordinates.
A1	N1	Current nodal accelerations.
BIGK	N1*(MUD+1) -((MUD+1)* MUD)/2	Total global stiffness.
BLAMB	9*NPRI	Nodal body vector transformations.
DICOS	9*NELE	Element vector transformations.
DICOSP	9*NOPT	Sliding plane acceleration vector direction cosines.

<u>FORTRAN Name</u>	<u>Size</u>	<u>Description</u>
E	12*NUMMAT	Material and section properties.
EFFLAS	N1	Old effective force.
EFFORC	N1	Current effective force.
EVAL	NBE*IMODAL	Eigenvalues from modal analysis.
EVEC	NBE*NBE* IMODAL	Eigenvectors from modal analysis.
FERROR	N1	Error force.
FEXOLD	N1	Old external force.
FINOLD	2*N1	Old nodal internal force.
FINT	2*N1	Nodal internal force.
FORCD	N1	Current external force.
GLABEL	10*NPLOT	Labels for plotted output.
INDEX	NELE+1	Index to the STRS array.
INMESH	NODMAX	Internal node number locator.
IX	7*NELE	Element connectivity.
MESHIN	NODET	Mesh node number locator.
NASN	NOPT	Number of primary nodes which may contact the sliding plane.
NCP	10*NOPT	Node numbers of primary nodes which may contact the sliding plane.
NODDIS	NUMDIS+1	Nodal fixities.
NPNO	NOPT	Primary node number of sliding plane.
NPOUT	2*NPIC	Picture output.
NTYPE	2*NPLOT	Plot type identifier.
PSU	NPTS*NPLOT	Output values for time histories.
SEATK	2*NOPT	Stiffness coefficients for elastic sliding plane.
SMASS	N1	Nodal masses.
SOUT	NPRS	Element output code.
SQMASS	NBE*IMODAL	Square root of nodal masses.
STFLAS	LBKE	Total global stiffness for modal analysis.
STOREK	2*MUD* NPDIS	Storage of stiffness for prescribed displacements.
STROLD	(Size is determined in sub- routine ASSBLE)	Old element information.

<u>FORTRAN Name</u>	<u>Size</u>	<u>Description</u>
STRS	(same as STROLD)	Current element information.
SS	NPRS	Output force values.
T	NPTS	Time values for plotted output.
TBLAM	9*NPRI	Temporary storage of body vector transformations.
UOUT	NPRU	Nodal output code.
UP	3*NOPT	Displacement of sliding plane.
UPOLD	3*NOPT	Old displacements of sliding plane.
UP1	3*NOPT	Velocity of sliding plane.
UP2	3*NOPT	Acceleration of sliding plane.
UU	NPRU	Output kinematic values.
VDAMP	NOPT	Viscous damping coefficient for sliding plane.
VO	N1	Old nodal velocities.
V1	N1	Current nodal velocities.
XC	NODET	X coordinate of node points.
XC	MEQ	Old nodal displacements.
X1	MEQ	Current nodal displacements.
YC	NODET	Y coordinate of node points.
ZC	NODET	Z coordinate of node points.

11. Organization of STRS Array

3-D Axial Spring Elements

Component Number	Quantity
1-3	Original local coordinates of secondary node I with respect to its associated primary node, $r^0 = \text{secondary-primary}$.
4-6	Body components of r^0 ($\bar{r}^0 = \lambda^T r^0$).
7-9	Original local coordinates of secondary node J with respect to its associated primary node.
10-12	Body components of r^0 .
13	Element strain
14	Element stress
15	Element axial force
16	Length change in element

3-D Linear, Elastic Rectangular Beam Element

Component Number	Quantity
1-6	Body components of original element unit vectors e_1^0 and e_2^0 ($\bar{e}^0 = \lambda^T e^0$)
7-9	Original local coordinates of secondary node with respect to its associated primary node, $r^0 = \text{secondary-primary}$.
10-12	Body components of r^0 ($\bar{r}^0 = \lambda^T r^0$). The above components 1-12 apply to element node I.
13-24	Same as above for element node J.
25	Element strain
26	Element stress
27	Axial force
28	Local y shear force v_y
29	Local z shear force v_z
30	Torsional moment M_x
31	Moment about local y axis at node I M_{Iy}
32	Moment about local y axis at node J M_{Jy}

33	Moment about local z axis at node I M_{Iz}
34	Moment about local z axis at node J M_{Jz}
35	Empty
36	Change in length
37	Rotation about local x axis θ_x
38	Rotation about local y axis at node I θ_{Iy}
39	Rotation about local y axis at node J θ_{Jy}
40	Rotation about local z axis at node I θ_{Iz}
41	Rotation about local z axis at node J θ_{Jz}
42-46	Empty

3-D Spinal Disk Beam Element

Component Number	Quantity
1-6	Body components of original element unit vectors e_1^0 and e_2^0 ($\bar{e}^0 = \lambda^T \mu e^0$).
7-9	Original local coordinates of secondary node with respect to its associated primary node, $r^0 = \text{secondary-primary}$.
10-12	Body components of r^0 ($\bar{r}^0 = \lambda^T r^0$). The above components 1-12 pertain to element node I.
13-24	Same as above for element node J.
25	Axial force
26	Local y shear force V_y
27	Local z shear force V_z
28	Torsional moment M_x
29	Moment about local y axis at node I M_{Iy}
30	Moment about local y axis at node J M_{Jy}
31	Moment about local z axis at node I M_{Iz}
32	Moment about local z axis at node J M_{Jz}
33-34	Empty
35	Strain at previous time step
36	Change in length
37	Rotation about local x axis θ_x

38	Rotation about local y axis at node I	θ_{Iy}
39	Rotation about local y axis at node J	θ_{Jy}
40	Rotation about local z axis at node I	θ_{Iz}
41	Rotation about local z axis at node J	θ_{Jz}
42-46	Empty	

Pressure Volume Penetration Element

Component Number	Quantity
1-3	Original local coordinates of secondary node with respect to its associated primary node $r^0 = \text{secondary} - \text{primary}$.
4-6	Body components of r^0 ($\bar{r}^0 = \lambda^T r^0$). The above components 1-6 pertain to the generic node 1 of the element.
7-36	Same as above for the other five generic nodes of the element.
37	Element internal pressure.
38	Element volume.
39	Element area.
40	Element axial force.

12. Graphics Program for Anatomical Analysis

This program was developed to aid the researcher in analyzing the simulated behavior of the human spine. The vertebrae, rib, sternum, head and pelvis can be plotted with symbols that are representative of these anatomical elements so that the configuration of the skeletal system can be visualized. In addition, options are available for cylinders and additional geometrical figures. These bodies can be rotated and displaced to any orientation in three dimensional space and this space can then be rotated relative to the viewing points. The back and right side projections are then plotted. Hidden portions of certain figures are removed so that resulting projections are not ambiguous due to a large number of hidden lines.

In order to facilitate use of the program, an overview of its procedure is given in the following paragraphs. Further details on the algorithms and procedures are given in subsequent Sections.

The elements, as represented by the program, are described by a combination of points connected by lines and by geometric solids, such as spheres or cylinders. The location of the points of an element are given in an element coordinate system $(\hat{x}, \hat{y}, \hat{z})$. The origin of this coordinate system is the base point of the element. This data is called element point data. In addition, elements which include geometric solids require element dimension data, such as the radius and the length of the cylinder.

The location and orientation of each element is described by the coordinates of the base point in the global system (x, y, z) and the orientation of the element's local coordinate system. The latter is specified by giving the global components of the element coordinate unit vectors, that is e_{1x} , e_{1y} , e_{1z} , e_{3x} , e_{3y} , and e_{3z} , these are equivalent to the direction cosines.

The plotting program thus requires two types of data:

1. position and orientation data of each element;
2. element description data consisting of element point data and/or element dimension data for each element.

The first type of data must be input in each run of the program by means of card input (Cards 5 in Section 13). For many anatomical elements, the element description data is permanently stored in a data bank and is an essential part of this program's capabilities. These elements are called standard elements and data for these elements have been obtained by measurements of skeletal segments and is reasonably representative of a typical anatomy; this data must be stored on units 20 and 27. If for any reason the user desired to modify this element description data, he must input his own description point data on these data banks. In addition, the user has a set of commands available that enable him to plot simple elements such as lines, cylinders and spheres: these are called user-defined elements.

To aid in the visualization, the depiction may be plotted from any angle relative to the global (x, y, z) coordinates. This option is effected by the command SHFT (cards 5), which implicitly constructs an (x', y', z') system, so that the (x, y, z) system is shifted relative to (x', y', z') by the Euler angles ϕ , θ , and ψ . The command VIEW (Cards 5) then given the option of plotting the (x', z') or the (y', z') views, or both. If only a lateral view and an antero-posterior view are desired, a SHFT command is not necessary. The coordinates of the physical plot are always denoted by X and Z, where X can correspond to either x' or y' , and Z always corresponds to z' . The X axis is placed along the bottom of the plot, and the Z axis is placed vertically.

The dimensions of the cube in the (x', y', z') system which encloses all elements in the plot must be specified; anything outside this cube is not plotted. The physical dimensions of the plot and location of the origin of the (x', y', z') coordinate system on

the plot are given by Card 4. The plot is then automatically scaled so that the specified space cube in the (x',y',z') system fits on the specified size of the physical plot, with the origin of the (x',y',z') system at the point that is specified. Note that the physical dimensions of the plot are specified in inches, whereas all data for the depiction is given in cm.

13. Input

All data except plot dimensions are in cm. Plot dimensions are in inches.

Card 1: Heading (20A4)

Cols. 1-80 TITLE: 80 alphanumeric characters to be used as a heading on output.

Card 2: Type of input (4X,A4)

Cols. 5-10 "VECTOR"

Card 3: Space in (x',y',z') coordinates to be plotted (6F10.0)

Cols. 1-10 x' min
11-20 x' max
21-30 y' min
31-40 y' max
41-50 z' min
51-60 z' max

Card 4: Size of plots and location of origin (6F10.0)

Cols. 1-10 TOTALX width of plot (inches) for plots of (x',z') view.
11-20 TOTALY width of plot (inches) for plots of (y',z') view. (Only needed is IDN >1 in VIEW command, see Cards 5).
21-30 TOTALZ height of plot (inches); will be the same for (x',z') and (y',z') views.
31-40 XNEG distance of the origin of the (x',y',z') system from left hand side of the plot (inches) in (x',z') plot.

- 41-50 YNEG distance of origin of (x',y',z') system from left hand side of the plot (inches) in (y',z') plot.
- 51-60 ZNEG distance of origin from bottom of plot (inches).

COMMAND cards: Each group of COMMAND cards plots a certain type of element or executes a specific operation in the graphics procedure. For each command, Cards 5A, 5B, and 5C must be in sequence. In some commands, Cards 5A and/or 5C are not needed and should be omitted; this varies with the command and the user should refer to COMMAND descriptions.

Cards 5A: Command cards - choose any of the commands listed under COMMAND DESCRIPTIONS, (2I2,A4,9F8.0)

Cols.	1-2	IDN	Body number (only needed for certain <u>standard elements</u> , see 5-1).
	3-4	NP	Number of element data points; if body is on data bank (see Table 18), set NP = 0 and the element description data need not be input. If an element is not a standard element, set NP = number of data points required as specified by the element command (see COMMAND description for specific instructions for each element).
	5-8	ID	Command (four alphanumeric characters from the list given in 5-1).
	9-16	P(1)	Global x coordinate of base point.
	17-24	P(2)	Global y coordinate of base point.
	25-32	P(3)	Global z coordinate of base point.
	33-40	X1	Global x component of local \hat{x} unit vector, $e_{xx}^{\hat{x}}$
	41-48	X2	Global y component of local \hat{x} unit vector, $e_{xy}^{\hat{x}}$
	49-56	X3	Global z component of local \hat{x} unit vector, $e_{xz}^{\hat{x}}$
	57-64	Z1	Global x component of local \hat{z} unit vector, $e_{zx}^{\hat{z}}$
	65-72	Z2	Global y component of local \hat{z} unit vector, $e_{zy}^{\hat{z}}$
	73-80	Z3	Global z component of local \hat{z} unit vector, $e_{zz}^{\hat{z}}$

Cards 5B: Follows Cards 5A for certain commands as specified in COMMAND descriptions.

Cards 5C: (NP/2 cards) Element point coordinate data. Needed only for certain commands as specified in COMMAND description; follows Card 5B; if there is no Card 5B for that COMMAND, Card 5C follows 5A.

Cols.	1-10	\hat{x} coordinate of point I
	11-20	\hat{y} coordinate of point I
	21-30	\hat{z} coordinate of point I
	31-40	\hat{x} coordinate of point I+1
	41-50	\hat{y} coordinate of point I+1
	51-60	\hat{z} coordinate of point I+1

COMMAND Descriptions

5.1 STANDARD ELEMENT PLOT COMMANDS

None of these commands require a Card 5B or Card 5C.

HEAD	Plot the head. The body number IDN is ignored.
RIBL	Plot the IDNth left rib.
RIBR	Plot the IDNth right rib.
STER	Plot the sternum. The body number IDN is ignored.
VERT	Plot the INDth thoracic vertebra.
VERL	Plot the IDNth lumbar vertebra.
BODY	The body with optional number IDN (see last column in Table 18) will determine which of the above elements is to be plotted. This option is used only for old data sets which do not include the above names. BODY commands must precede all other commands.

5.2 USER-DEFINED PLOT COMMANDS

Cards 5B and 5C are only needed as noted.

LINC	The (NP) points on Cards 5C will be plotted to form a closed curve by connecting point (i) to point (i+1), i=1 to NP, and then connecting point (NP) to point (1).
LINO	The (NP) points on Cards 5C will be plotted to form an open curve by connecting point (i) to point (i+1), i=1 to NP.

LINS The NP points on Cards 5C must have positive \hat{x} coordinates. For each point, an additional point is generated by mirror image in the \hat{y} - \hat{z} plane. The resulting set of points are then plotted as in LINC.

SPHR Plot a sphere with optional line segment superimposed.

Card 5B

Cols. 1-10 $\hat{x}, \hat{y}, \hat{z}$ coordinates of center of sphere,
11-20 respectively, relative to base point,
21-30 usually 0,0,0.

31-40 $\hat{x}, \hat{y}, \hat{z}$ coordinates of a point on the sphere,
41-50 respectively, which is used to determine
51-60 the radius.

Cards 5C are optional and can be used to input coordinates $\hat{x}, \hat{y}, \hat{z}$ or NP/2 pairs of points. Each pair of points is connected by a line segment.

CONE A truncated conic section is to be plotted with optional line segments superimposed. The base point is the center of the bottom ellipse.

Card 5B (6F10.0 Format)

C1 - major half axis of the bottom base
C2 - minor half axis of the bottom base
C3 - the height of the body
C4 - The major half axis of the top plane
C5 - the minor half axis of the top plane

Cards 5C are optional and are used to input line segments just as for SPHR, but only visible line segments are plotted.

CYLN An elliptical cylinder is to be plotted with optional line segments superimposed. The base point is the center of the bottom ellipse.

Card 5B (3F10.0 Format)

C1 - the major half axis of the base
C2 - the minor half axis of the base
C3 - the length of the cylinder

Cards 5C are optional line segments as in CONE.

5.3 COMMANDS FOR PROGRAM EXECUTION AND OPTIONS

(*only commands denoted by asterisks must be included for the program to run; all others may be omitted if the user wishes to run with the default options.)

- GRID This command will add a frame around the plot.
- SHFT This command will rotate all bodies by Euler angles (in radians) (ϕ , θ , ψ) which are the X1, X2, X3 values on Cards 5A respectively.
- VIEW This command determines the views to be plotted.
If IDN = 1, x',z' plane is plotted.
If IDN = 2, y',z' plane is plotted.
If IDN = 3, both views are plotted.
If no VIEW card is included, both views will be plotted.
- DEBUG This command will trace the flow of the program so error conditions can be traced. This is done by printing the object definition and tests performed by the ID/3D sub-routines. This command will also print the transformed body point coordinates.
- MARK This command will place a string of alphanumeric characters on the plot. The string is taken from Card 5B. The orientation of the message is determined from the data on Card 5A.
P(1) z coordinate of the left side of string.
P(2) x' or y' coordinate of the left side of string.
P(3) height of letters in inches.
X1 angle at which the message is plotted from measured vertical axis in degrees.
X2 number of characters in message.
X3 view that message is to be plotted on
 X3 = 1 x',z' view
 X3 = 2 y',z' view
- WEDG This command adds wedging to the vertebrae, according to the following:
IDN = 1 AP wedging only (AP: antero-posterior)
IDN = 2 AP and lateral wedging
If no WEDG command is read, only AP wedging is included.
- SCAL This command will plot a 5 cm line on the plot for indicating the scale of the plot.
- NRES Each line segment is divided into NRES equal subdivisions to check for hidden lines. This card may be omitted, in this case the value of NRES is 5.
- GO* This card is used as a delimiter of the data for each problem, and must be the last card if more than one set of data is to be plotted in one run. A set of cards for another plot may follow this card. The word GO must be left oriented.

The limits on the number of bodies in the standard version of the program are:

maximum number of bodies MNB = 60

maximum number of element description data MWBP = 1500 x 3

maximum number of vertebrae MNV = 25

Table 18

Standard Elements

<u>Body type</u>	<u>IDN</u> (for command in left-hand column)	<u>Description</u>	(Optional IDN for use only when BODY command is used.)
		Sacrum (not plotted)	1
VERT	1	1st thoracic vertebrae	2
VERT	2	2nd thoracic vertebrae	3
VERT	3	3rd thoracic vertebrae	4
VERT	4	4th thoracic vertebrae	5
VERT	5	5th thoracic vertebrae	6
VERT	6	6th thoracic vertebrae	7
VERT	7	7th thoracic vertebrae	8
VERT	8	8th thoracic vertebrae	9
VERT	9	9th thoracic vertebrae	10
VERT	10	10th thoracic vertebrae	11
VERT	11	11th thoracic vertebrae	12
VERT	12	12th thoracic vertebrae	13
VERL	1	1st lumbar vertebrae	14
VERL	2	2nd lumbar vertebrae	15
VERL	3	3rd lumbar vertebrae	16
VERL	4	4th lumbar vertebrae	17
VERL	5	5th lumbar vertebrae	18
RIBR	1	1st right rib	19
RIBL	1	1st left rib	20
RIBR	2	2nd right rib	21
RIBL	2	2nd left rib	22
RIBR	3	3rd right rib	23
RIBL	3	3rd left rib	24
RIBR	4	4th right rib	25
RIBL	4	4th left rib	26

Table 18 (continued)

<u>Body type</u>	<u>IDN</u> (for command in left-hand column)	<u>Description</u>	(Optional IDN for use only when BODY command is used)
RIBR	5	5th right rib	27
RIBL	5	5th left rib	28
RIBR	6	6th right rib	29
RIBL	6	6th left rib	30
RIBR	7	7th right rib	31
RIBL	7	7th left rib	32
RIBR	8	8th right rib	33
RIBL	8	8th left rib	34
RIBR	9	9th right rib	35
RIBL	9	9th left rib	36
RIBR	10	10th right rib	37
RIBL	10	10th left rib	38
STER	*	sternum	39
HEAD	*	head	40

*IDN not needed for HEAD or STERN commands.

APPENDIX II. ELEMENT STIFFNESS MATRICES

In this Appendix the local element stiffness matrices and corresponding global transformation matrices are presented. The elements are standard in structural analysis so no derivations are given. The local element stiffness consists of a tangential stiffness plus a geometric stiffness

$$[\hat{k}] = [\hat{k}_T] + [\hat{k}_G] \quad (\text{II.1})$$

which relate nodal deformations to nodal forces in the corotational element coordinates. The global element stiffness matrix is then obtained by transforming the local stiffness by

$$[k] = [T]^T [\hat{k}] [T] \quad (\text{II.2})$$

where $[T]$ is the matrix defined by Eq. (2.36). The total global stiffness is found by adding together the global stiffnesses of all elements,

$$[k] = \sum_{e=1}^E [\ell^{(e)}]^T [k^{(e)}] [\ell^{(e)}] \quad (\text{II.3})$$

where $[\ell^{(e)}]$ is the Boolean connectivity matrix for the element. As is standard in finite element programs, the matrix operations indicated in Eq. (II.3) are not performed as matrix multiplications, but simply as additions. Thus the total global stiffness matrix is obtained by adding the element global stiffnesses into the appropriate

locations of the total matrix, which of course depends on the node numbers of the elements, i.e. connectivity.

The local element stiffness of spring elements is

$$[\hat{k}_T] = k_1 + 3k_2 \delta^2 \begin{bmatrix} 1 & & & & & & \\ & 0 & 0 & & & & \\ & & & \text{sym.} & & & \\ & 0 & 0 & 0 & & & \\ & -1 & 0 & 1 & & & \\ & & & & & & \\ & 0 & 0 & 0 & 0 & 0 & \\ & 0 & 0 & 0 & 0 & 0 & 0 \end{bmatrix} \quad (\text{II.4})$$

$$[\hat{k}_G] = \frac{\hat{f}_{Jx}}{l} \begin{bmatrix} 0 & & & & & & \\ & 0 & 1 & & & & \\ & & & \text{sym.} & & & \\ & 0 & 0 & 1 & & & \\ & 0 & 0 & 0 & 0 & & \\ & 0 & -1 & 0 & 0 & 1 & \\ & 0 & 0 & -1 & 0 & 0 & 1 \end{bmatrix} \quad (\text{II.5})$$

Here \hat{f}_{Jx} is the current axial force in the element and l is the element length.

In the beam element, for the purpose of saving space, it is convenient to express the tangent stiffness matrix as a product of two matrices. Hence

$$[\hat{k}_T] = [Q]^T [\hat{k}^*] [Q] \quad (\text{II.6})$$

stiffness is

$$[k_T] = B \{E\} \{E\}^T \quad (II.9)$$

where B is the tangent bulk modulus and {E} is given in Table 1.

The geometric stiffness is not included for the hydrodynamic element.

The transformation matrices are written as partitioned matrices, consisting of 3 x 3 submatrices defined by Eqs. (2.1) through (2.4) and Eq. (2.18). The spring transformation is

$$[T]^T = \begin{bmatrix} [\mu]_I & [0] \\ [\Omega]_I^T [\lambda]_I^T [\mu]_I & [0] \\ [0] & [\mu]_J \\ [0] & [\Omega]_J^T [\lambda]_J^T [\mu]_J \end{bmatrix} \quad (II.10)$$

The beam transformation is

$$[T]^T = \begin{bmatrix} [\mu]_I & [0] & [0] & [0] \\ [\Omega]_I^T [\lambda]_I^T [\mu]_I & [\lambda]_I^T [\mu]_I & [0] & [0] \\ [0] & [0] & [\mu]_J & [0] \\ [0] & [0] & [\Omega]_J^T [\lambda]_J^T [\mu]_J & [\lambda]_J^T [\mu]_J \end{bmatrix} \quad (II.11)$$

The hydrodynamic element transformation is given by

$$\begin{aligned}
 [T]^T &= \begin{bmatrix}
 [I] & [I] & [0] & [0] & [0] \\
 [\Omega]_I^T [\lambda]_I^T & [\Omega]_J^T [\lambda]_J^T & [\Omega]_K^T [\lambda]_K^T & [\Omega]_L^T [\lambda]_L^T & [\Omega]_M^T [\lambda]_M^T \\
 [0] & [0] & [0] & [I] & [I] \\
 [0] & [0] & [0] & [\Omega]_L^T [\lambda]_L^T & [\Omega]_M^T [\lambda]_M^T \\
 & & & & [\Omega]_N^T [\lambda]_N^T
 \end{bmatrix}
 \end{aligned}$$

(II.12)